

Protein Adsorption on Nanostructured Silica Surfaces

vorgelegt von
Diplom-Chemiker
Jens Meißner
geb. in Pritzwalk

von der Fakultät II – Mathematik und Naturwissenschaften
der Technischen Universität Berlin
zur Erlangung des akademischen Grades

Doktor der Naturwissenschaften
– *Dr. rer. nat.* –

genehmigte Dissertation

Promotionsausschuss:

Vorsitzender: Prof. Dr. Reinhard Schomäcker
Berichter: Prof. Dr. Gerhard H. Findenegg
Berichter: Prof. Dr. Michael Gradzielski
Berichter: Prof. Dr. Bhuvnesh Bharti

Tag der wissenschaftlichen Aussprache: 12. Dezember 2017

Berlin 2018

Danksagung

An erster Stelle möchte ich mich ganz herzlich bei Prof. Dr. Gerhard H. Findenegg bedanken, in dessen Arbeitskreis ich diese Dissertation anfertigen durfte. Jederzeit hatte ich die Möglichkeit zu wissenschaftlichen Diskussionen, die die Entwicklung dieser Arbeit ganz entscheidend voran gebracht haben.

Furthermore, I want to thank Prof. Dr. Bhuvnesh Bharti, who was helping me during my stay at the North Carolina State University and advising me during my time as a diploma student. I consider myself to be lucky to have met you.

Prof. Dr. Michael Gradzielski danke ich für die Möglichkeit die Labore seiner Arbeitsgruppe zu nutzen.

Weiterhin möchte ich Prof. Dr. Reinhard Schomäcker für die Übernahme des Vorsitzes meiner Prüfungskommission danken.

Auch möchte ich mich bei B.Sc. Albert Prause bedanken, dessen Unterstützung als studentische Hilfskraft mir viel experimentelle Arbeit abgenommen hat. Also, I want to thank M.Sc. Caroline Di Tommaso for her help with the SBA-15 functionalization during her summer internship.

Für die aufopferungsvolle Hilfe und Anleitung bei Synchrotron-Messzeiten in Triest bedanke ich mich bei Prof. Dr. Heinz Ammenitsch und seinem Team mit Dr. Benedetta Marmioli und Dott. Barbara Sartori. Grazie mille!

Außerdem möchte ich mich bei Jana Lutzki, Gabi Görig-Hedicke, Michaela Dzionara sowie Petra Erdmann, Maria Bülth und Christiane Abu-Hani bedanken.

Für die Finanzierung im Rahmen des IRTG 1524 bedanke ich mich bei der Deutschen Forschungsgemeinschaft, dem Sprecher des IRTG 1524 Prof. Dr. Martin Schoen sowie der geschäftsführenden Direktorin Dr. Daniela Fliegner.

Ein großes Dankeschön gebührt auch allen Kommilitonen und Freunden vom Stranski-Laboratorium, insbesondere Olli, Martin, Miriam und Lucas, Michi, Caro sowie Sven, mit denen jeder Arbeitstag spannend wurde.

Mein besonderer Dank gilt meinen langjährigsten Freunden Micha und den Gentlemen Alexander, Marc, Christoph, Michael, Aymeric und Jan. Durch euch konnte ich permanent neue Motivation schöpfen!

Vom ganzen Herzen will ich mich bei meiner Familie bedanken. Auf meine Schwester Katja mit Konstantin und Oskar kann ich mich blind verlassen. Mein größter Dank gilt meinen wunderbaren Eltern Elke und Germut, die mich auf meinem Weg nach allen Kräften unterstützt haben und mir in jeder meiner Entscheidungen beistanden!

Zusammenfassung

Die vorliegende Dissertation ist eine Studie über die Interaktion von globulären Proteinen mit nanostrukturierten Silika Oberflächen. Ziel der Arbeit ist es, ein besseres Verständnis für die Einflüsse hoher Oberflächenkrümmung und räumlicher Einengung auf das Adsorptionsverhalten und auf die Morphologie von adsorbierten Proteinen zu entwickeln.

Das Adsorptionsverhalten von Lysozyme und β -Lactoglobulin auf Silika-Nanopartikeln wurde von pH 2 bis 11 und einer Ionenstärke bis zu 100 mM untersucht. In diesem pH Bereich ändert sich die Ladungsverteilung auf Proteinen und Silika drastisch. So war es möglich, die Wechselwirkungen zwischen Partikel und β -Lactoglobulin auf beiden Seiten des isoelektrischen Punktes des Proteins zu studieren. Die erhaltenen Daten wurden mit der Guggenheim – Anderson – de Boer Adsorptionsisotherme ausgewertet. Dieses Model lässt die Mehrschichtadsorption aus einer flüssigen Phase zu.

Mithilfe von Neutronen Kleinwinkelstreuung wurde die Orientierung des globulären Proteins Cytochrom *c* auf Silika Nanopartikeln bei verschiedenen äußeren pH Bedingungen bestimmt. Die Streudaten wurden mit einem Formfaktor Model ausgewertet, das ‚Himbeerförmige‘ Strukturen beschreibt. Eine starke Veränderung in der Adsorptionsorientierung relativ zur Partikeloberfläche wurde zwischen pH 3 und 4 gefunden. Dieses Verhalten wurde mit dem Dipolmoment des Proteins in Verbindung gebracht. Simulationen des Dipolmoments für verschiedene Protonierungszustände von Cytochrom *c* zeigen eine charakteristische Änderung der Dipolmomentorientierung in der gleichen pH Region.

In vorangegangenen Studien wurde gefunden, dass Proteinadsorption eine Heteroaggregation von Silikapartikeln auslösen kann. In dieser Arbeit wurde die großräumige Struktur der Aggregate von Silikapartikeln und fluoreszenzmarkiertem Lysozym mit konfokaler Laserrastermikroskopie untersucht. Die 3D Aggregatstruktur wurde aus Stapeln einzelner 2D Aufnahmen rekonstruiert. Die globale Struktur wurde mithilfe des Verhältnisses aus der Oberfläche und dem Volumen der Aggregate abgeschätzt.

Die Aufnahme von Proteinen in nanometerkleinen Poren hängt vom zugänglichen Porenvolumen und von den Wechselwirkungen zwischen Protein und Porenwand ab. Die Adsorption von Lysozym in mesoporösen SBA-15 mit nativen und chemisch modifizierten Porenwänden wurde über einen weiten pH Bereich untersucht. Um die beobachteten Unterschiede zu erklären, wurde ein geometrisches Model für die Porenauffüllung entwickelt, welches die Porengrößenverteilung einbezieht.

Die Schmelzpunktserniedrigung von elf wässrigen Alkalihalogenidlösungen in den Mesoporen von SBA-15 und MCM-41 wurde mit DSC untersucht. Es wurde gefunden, dass die eutektische Temperatur vom Volumenbruch der Salzkristalle in der Pore abhängt. Die Unterschiede waren am größten für Salze, die Oligohydrat Kristalle formen. Salzspezifische Effekte spielen dabei nur eine untergeordnete Rolle.

Abstract

This Ph.D. thesis presents a study of the interaction of globular proteins with nanostructured silica surfaces. It aims to gain a better understanding of the consequences of a high surface curvature and confinement on the adsorption behavior and morphology of the adsorbed protein.

The adsorption behavior of lysozyme and β -lactoglobulin on silica nanoparticles was studied from pH 2 to 11 and ionic strength until 100 mM. Within this pH range the surface charge distribution on proteins and silica changes drastically. Specifically it was possible to study the interactions between particles and β -lactoglobulin on both sides of the isoelectric point of the protein. Resulting data were evaluated with the Guggenheim – Anderson – de Boer adsorption isotherm equation which accounts for multilayer adsorption from liquid phases.

The orientation of the globular protein cytochrome *c* adsorbed on silica nanoparticles was determined as a function of solution pH using small angle neutron scattering. The scattering data was evaluated with a form factor model accounting specifically for 'raspberry-shaped' structures. A pronounced shift in the adsorption orientation relative to the particle surface was detected between pH 3 and 4. This behavior was correlated with the dipole moment of the protein. Simulations of the dipole moment for different protonation states of cytochrome *c* show a distinctive change in the dipole moment orientation for the same pH region.

In preceding studies it was found that protein adsorption can cause hetero-aggregation of the silica nanoparticles. Here, the large-scale structure of these aggregates was studied by confocal laser scanning microscopy with fluorescently labeled lysozyme. Stacks of 2D images were used to reconstruct the 3D aggregate structure and estimate the global structural properties in terms of their surface-area-to-volume ratio.

Protein uptake in nanometer-sized pores depends on the accessible pore space and the interaction of the protein with the pore wall. The adsorption of lysozyme in mesoporous SBA-15 silica materials with native and chemically modified pore walls was studied over a wide pH range. To assess the observed differences in the protein uptake capacity of the materials, a geometrical pore filling model was developed that takes into account the different pore-size distribution of the materials.

The melting point depression of eleven aqueous alkali halide systems confined in the mesopores of SBA-15 and MCM-41 silica was studied by DSC. It was found that the eutectic temperature in the pores is mainly dependent of the fraction of volume occupied by the salt crystallites, i.e. largest for salts forming oligohydrates in the pores. Salt-specific adsorption effects at the pore wall are only of minor importance.

Publications

Parts of this thesis are based on the publications listed below.

Chapter 3:

J. Meissner, A. Prause, B. Bharti and G. H. Findenegg: Characterization of protein adsorption onto silica nanoparticles: influence of pH and ionic strength", *Colloid Polym Sci* **2015**, 293, 3381 – 3391. Reproduced with permission. Published open access under the Creative Commons Attribution 4.0 International license.

<http://dx.doi.org/10.1007/s00396-015-3754-x>

Chapter 6:

J. Meissner, A. Prause, C. Di Tommaso, B. Bharti and G. H. Findenegg: Protein Immobilization in Surface-Functionalized SBA-15: Predicting the Uptake Capacity from the Pore Structure, *J. Phys. Chem. C* **2015**, 119, 2438 – 2446. Copyright 2015 American Chemical Society. Reproduced with permission.

<http://dx.doi.org/10.1021/jp5096745>

Chapter 7:

J. Meissner, A. Prause and G. H. Findenegg: Secondary Confinement of Water Observed in Eutectic Melting of Aqueous Salt Systems in Nanopores, *J. Phys. Chem. Lett.* **2016**, 7, 1816 – 1820. Copyright 2016 American Chemical Society. Reproduced with permission.

<http://dx.doi.org/10.1021/acs.jpcclett.6b00756>

Contents

CHAPTER 1 INTRODUCTION	1
1.1 PROTEIN ADSORPTION AT HIGHLY CURVED HYDROPHILIC SURFACES.....	1
1.2 PROTEIN-INDUCED AGGREGATION OF SILICA NANOPARTICLES	3
1.3 ORIENTATION OF ADSORBED PROTEIN MOLECULES.....	4
1.4 FREEZING/MELTING OF CONCENTRATED SALT SOLUTIONS IN NANOPORES	5
CHAPTER 2 METHODS AND MODELS	7
2.1 FLUORESCENCE MICROSCOPY	7
2.1.1 Confocal Laser Scanning Microscopy.....	7
2.1.2 Fluorescence Correlation Spectroscopy	9
2.2 SMALL ANGLE NEUTRON SCATTERING	10
2.2.1 Technical Background.....	11
2.2.2 Raspberry Form Factor Model	13
2.3 PROTEIN DIPOLE MOMENT	15
2.4 DIFFERENTIAL SCANNING CALORIMETRY	17
CHAPTER 3 CHARACTERIZATION OF PROTEIN ADSORPTION ONTO SILICA	
NANOPARTICLES: INFLUENCE OF PH AND IONIC STRENGTH	19
3.1 INTRODUCTION	19
3.2 MATERIALS AND METHODS	21
3.2.1 Materials.....	21
3.2.2 Protein Adsorption Measurements	21
3.2.3 Adsorption Isotherm Equation	22
3.3 RESULTS	23
3.3.1 Nanoparticle and Protein Characteristics	23
3.3.2 Lysozyme Adsorption.....	25
3.3.3 β -Lactoglobulin Adsorption.....	27
3.4 DISCUSSION	29
3.5 CONCLUSION	33
CHAPTER 4 EVOLUTION OF HETERO-AGGREGATE STRUCTURE AT DIFFERENT	
PROTEIN LOADINGS.....	35
4.1 INTRODUCTION	35
4.2 MATERIALS AND METHODS	36
4.2.1 Materials.....	36

4.2.2	Protein Labeling.....	36
4.2.3	Adsorptions Measurements.....	36
4.2.4	Fluorescence Correlation Spectroscopy.....	37
4.2.5	Confocal Laser Scanning Microscopy.....	37
4.3	RESULTS.....	38
4.3.1	Adsorptions Comparison.....	38
4.3.2	Fluorescence Correlation Spectroscopy.....	40
4.3.3	Confocal Laser Scanning Microscopy.....	41
4.4	DISCUSSION AND OUTLOOK.....	43
4.4.1	Adsorptions Comparison.....	43
4.4.2	Fluorescence Methods.....	44

CHAPTER 5 ORIENTATION OF CYTOCHROME C ADSORBED ON SILICA

PARTICLES.....		49
5.1	INTRODUCTION	49
5.2	MATERIALS AND EXPERIMENTAL TECHNIQUES.....	50
5.3	THE ‘RASPBERRY–LIKE’ FORM FACTOR.....	51
5.4	CHARGE DISTRIBUTION ON CYTOCHROME C	56
5.5	DISCUSSION AND CONCLUSIONS.....	58
5.6	APPENDIX	60
5.6.1	Characterization of Silica Particles and Cytochrome c	60
5.6.2	Fitting of SANS Data with the RB-model.....	61
5.6.3	Adsorption Isotherms and Calculation of Expected Surface Coverage.....	62
5.6.4	Instrumental Details SANS	63

CHAPTER 6 PROTEIN IMMOBILIZATION IN SURFACE-FUNCTIONALIZED SBA-15:

PREDICTING THE UPTAKE CAPACITY FROM THE PORE STRUCTURE 65		
6.1	INTRODUCTION	65
6.2	PORE FILLING MODEL.....	66
6.3	RESULTS	68
6.3.1	Functionalized SBA-15 Materials	68
6.3.2	Analysis of Porosity	70
6.3.3	Lysozyme Adsorption.....	73
6.3.4	Protein Immobilization Capacity of the Materials	74
6.4	DISCUSSION	77
6.4.1	Protein Uptake Capacity.....	77
6.4.2	Influence of Surface Functionalization	78
6.5	CONCLUSION	79
6.6	APPENDIX	80
6.6.1	Preparation of Mesoporous Materials	80

6.6.2	Sample Characterization Methods.....	81
6.6.3	Calculation of Matrix Porosity	82
6.6.4	Normalized Pore Size Distribution Function	85
6.6.5	Protein Adsorption Measurements	87
6.6.6	Adsorption Data and Langmuir Fits for Lysozyme in the OMS Materials	88
6.6.7	Protein pore filling model	89
CHAPTER 7 SECONDARY CONFINEMENT OF WATER OBSERVED IN EUTECTIC		
MELTING OF AQUEOUS SALT SYSTEMS IN NANOPORES		93
7.1	INTRODUCTION	93
7.2	RESULTS AND DISCUSSION	94
7.3	CONCLUSION	99
7.4	APPENDIX	100
7.4.1	Characterization of silica materials	100
7.4.2	Eutectic point of bulk systems.....	100
7.4.3	Systems Forming Salt Hydrates	102
7.4.4	Volume fraction of Salt in Solid Eutectic Mixtures	102
7.4.5	Information from DSC Cooling Scans	104
7.4.6	Information from in situ XRD.....	107
7.4.7	Summarized DSC Pore Melting Results	109
CHAPTER 8 CONCLUSIONS AND OUTLOOK.....		113
8.1	PROTEIN ADSORPTION ON SILICA NANOPARTICLES ON ABOVE AND BELOW THE ISOELECTRIC POINT	113
8.2	HETERO-AGGREGATION OF SILICA NANOPARTICLES WITH A PROTEIN: OBSERVING THE AGGREGATE STRUCTURE WITH FLUORESCENCE METHODS.....	114
8.3	ORIENTATION OF ADSORBED PROTEIN ON BULK pH CONDITIONS AS A CONSEQUENCE OF THE DIPOLE ORIENTATION	116
8.4	PREDICTION OF PROTEIN ADSORPTION IN NATIVE AND CHEMICALLY MODIFIED MESOPOROUS SILICA MATERIALS	117
8.5	FREEZING/MELTING OF AQUEOUS SALT SYSTEMS IN SILICA MESOPORES	119
REFERENCES		121
ABBREVIATIONS AND SYMBOLS.....		139

Chapter 1 Introduction

Adsorption and immobilization of proteins at solid surfaces play an important role in the environment and in many fields of technology. While protein adsorption at flat surfaces has been studied for many decades, the interaction with nanoparticles and immobilization in nanoporous matrices represents a relatively new field of research. In this thesis I present the results obtained during my Ph.D. research. The major topic is adsorption of proteins onto nanostructured surfaces e.g. inorganic nanoparticles and porous materials. The first chapter gives a brief introduction in the field of colloidal physics and establishes a general understanding of the research field.

1.1 Protein Adsorption at Highly Curved Hydrophilic Surfaces

In the last two decades colloidal science grew into a technology with lots of applications in various fields and disciplines. Today nanoscopic materials can be found in all parts of the everyday life, reaching from quantum dots used in modern displays¹ over silver nanoparticles in antibacterial products and cleansers^{2,3} up to medical devices for targeted drug delivery.^{4,5} In the near future, nanomaterials will be omnipresent in the human environment and therefore exposed to the biological media containing salts, proteins and polymers. Adsorption of these compounds on nanoparticles and nanostructured surfaces is a ubiquitous process and is observed on hydrophobic as well as on hydrophilic surfaces. It is obvious that this has an influence on both, the particles and the protein. Hence, the intended functionality of surfaces can be affected. For this reasons a general and in-depth understanding of the interactions of nanomaterials with biological matter and the resulting consequences is vital.

Maybe the most fundamental question in this field is for the nature and strength of the interaction of proteins with the respective surface. At this point it is important to differentiate between hydrophobic and hydrophilic surfaces. The main driving force for adsorption of proteins on hydrophobic surfaces is of entropic nature. In the case of hydrophobic surfaces immersed in aqueous solutions, water molecules form a structured network (hydrophobic effect) in the close vicinity of the surface. During the process of adsorption these ordered water molecules are liberated from the surface. The adsorption force caused by this entropic gain can be big enough to even bypass electrostatic repulsion.^{6,7}

In contrast to that the interactions between soft matter and hydrophilic surfaces are dominated by electrostatic forces and adsorption is almost exclusively limited to situations when protein and surface are oppositely charged.⁷ This holds for structurally stable and inflexible (“hard”) proteins (e.g. lysozyme and cytochrome *c*). On the other hand “soft” proteins

can deform easily as a consequence of lacking disulfide bonds and fewer hydrogen bonds. Such instable proteins can lose their secondary structure to a certain extend upon adsorption. In this case entropy contributes to the overall adsorption energy.

In order to quantitatively describe the protein adsorption on nanostructured surfaces different isotherm models have been discussed. The most fundamental model is the Langmuir isotherm developed by Irving Langmuir in the early 20th century.⁸ It assumes that all adsorption sites are equivalent, only one monolayer is adsorbed and molecules adsorbed on neighboring sites do not interact with each other. For many situations these assumptions are not valid as proteins usually carry a net charge and adsorbed on neighboring sites the proteins will experience a strong repulsive interaction. Alternatively, the Hill model was considered to describe such materials better.⁹ This model was in its first form developed to describe the dissociation curves of hemoglobin and assumes a cooperative adsorption behavior. In the case of non-cooperative behavior this isotherm model reduces to the Langmuir model. This means multilayer adsorption is not natively described by this model. In contrast to that, the GAB-model (Guggenheim-Anderson-de Boer) accounts for multilayer adsorption and describes three states for the adsorbate molecule.^{10,11} A first layer with direct contact to the substrate is strongly bound. In every further layer the adsorbate molecules are equally strong bound but different from the first layer and the bulk phase. The GAB-model was used for the evaluation of the adsorption experiments presented in Chapter 3, where differently charged proteins (lysozyme and β -lactoglobulin) were adsorbed to the anionic surface of silica particles.

A special case of nanostructured surfaces are nanopores, i.e. pore with a uniform diameter in the nanometer range. Such pores are found in the ordered mesoporous silicates such as SBA-15 or MCM-41. These materials are often considered as suitable support materials for immobilized enzymes in order to stabilize the proteins against polar solvents or heat^{12–14} and as carriers for targeted protein release.^{15–17} The microenvironment in these pores can be specifically tailored for each application by adjusting the pore size and manipulating the surface chemistry.^{18,19} By adequately choosing the parameters it is possible to enhance the stability and enzymatic activity of an enzyme compared to the native, free protein.^{20–24} On the other hand, it is also possible to avoid protein adsorption on surfaces by modifying the surface chemistry. It is reported that zwitterionic and polyethylene glycol grafted surfaces are protein repellent.²⁵ This effect can be utilized to protect exposed surfaces from biofouling. In Chapter 6 this thesis the loading capacity of such porous materials was analyzed and described with a general pore filling model, accounting for irregularities of the pore-size distribution.

1.2 Protein-Induced Aggregation of Silica Nanoparticles

The behavior of colloidal dispersions is often determined by the interplay of van der Waals and electrostatic double layer forces, as described by the classical DLVO theory (after Derjaguin, Landau, Verwey and Overbeek).^{26,27} Accordingly, in a stable colloidal dispersion the short range van der Waals attraction is compensated by electrostatic repulsion between equally charged particles. This interplay can be disturbed by changes in the solution composition. For example an addition of salt (increase in ionic strength, IS) screens the repulsive electrostatic force which in turn lowers the barrier for a close contact of the particles. In close proximity the attractive van der Waals force dominates and causes a strong attraction between single particles, ultimately causing aggregation. Despite its ability to describe the stability of colloidal dispersions, the DLVO theory does not include all forces acting between colloidal particles. These non-DLVO forces, such as steric interactions, hydration forces, hydrophobic interactions and depletion forces,²⁸ can also define the state of a system containing proteins and silica particles.^{29,30}

In order to discuss systems containing proteins and nanoparticles it is important to briefly look at the surface charge of proteins. Proteins are polyelectrolytes with different cationic or anionic groups, each with a different dissociation constant. Depending on the solution pH these groups are either charged (positively or negatively) or uncharged and thus the net charge of the entire protein varies with pH. At a protein-specific pH the number of positive and negative charges are equal leading to a situation where the protein is electrostatically neutral although it still carries local charges. This point is called isoelectric point (IEP). Below this pH value the protein is positively charged, at pH exceeding the IEP the protein is negatively charged.

When added to a dispersion of charged particles, an oppositely charged protein will readily adsorb at the particle surface as a consequence of electrostatic attraction. In this case the adsorption of proteins can cause a destabilization of the colloidal dispersion. This behavior is explained with bridging aggregation of the particles by the protein (see Chapter 3 and 4), i.e. simultaneous binding of a protein molecule to two particles, leading to large-scale aggregates and flocculation of the system. Often even visible to the bare eye, as the stable dispersion immediately turns turbid upon protein addition.

In our earlier work we reported a study of bridging aggregation of silica nanoparticles by lysozyme.^{31,32} Protein adsorption was found between the IEP of silica and lysozyme and the adsorption capacity increased towards the IEP of lysozyme as the electrostatic repulsion between individual adsorbed molecules decreases. In the same pH interval the increased turbidity indicated strong aggregation between the particles. Zeta potential measurements showed qualitatively a behavior which is expected for particles with a certain number of adsorbed proteins.

The aggregate structure was further investigated by a detailed analysis with small-angle x-ray scattering (SAXS) under different pH and salinity conditions.³¹ The structure factor of the SAXS intensity profiles was modeled with a short-range square-well pair potential.³² The analysis showed a pronounced influence of pH on the aggregate structure. At low pH ($\text{pH} < 6$) the aggregates were small and dense and the structure was not affected by changes in the ionic strength of the surrounding solution. With increasing pH the aggregate structure opened up to a looser network of large, branched aggregates. At pH values beyond pH 9 a distinct salt effect was found. Without additional salt the aggregate structure remained open and loose up to the maximum pH of the study. In this pH regime the addition of salt led to an increased attractive force between the particles as the electrostatic repulsion is shielded by the high IS.

As the structural studies of the protein-silica aggregates had been performed only for fixed protein to silica ratios, it was of interest to specifically investigate the evolution of aggregate sizes as the number ratio of protein to silica particles was changed. Such a study was now performed with the help of fluorescence techniques. In Chapter 4 a study using a combination of fluorescence laser scanning microscopy (CLSM) and fluorescence correlation spectroscopy (FCS) is shown. In this work the early stages of the aggregation process (i.e. low protein to silica ratios) were investigated with FCS whereas later stages (i.e. high protein to silica ratios) were studied with CLSM. With this combination of techniques it was possible to observe the structural evolution of hetero-aggregates over several decades of protein to silica ratios and visualize the large-scale structures by direct optical methods.

1.3 Orientation of Adsorbed Protein Molecules

For the development of useful industrial application of enzyme/nanoparticle systems details of the adsorption of protein molecules, including adsorption-induced changes of tertiary and secondary structure, and the orientation of the molecule relative to the surface need to be understood, as the stability and function crucially depend on these parameters.³³

One useful method to probe the internal structure of a protein either in solution or adsorbed on nanoparticles is circular dichroism spectroscopy (CD spectroscopy). With this technique the content of ordered sequences in the protein is analyzed by measuring the absorption of circular polarized UV-light. Differences in the secondary structure between native and adsorbed protein can be traced back to different content of alpha-helices, beta-sheets and coiled segments of the peptide backbone. Many of these studies found a significant change in the secondary structure^{34–36} for a variety of protein-particle combinations. Other studies show a contrary picture and report only minor changes in the secondary structure of the protein.³⁷ For example human serum albumin is structurally influenced when contacted to silver particles but is not affected by gold particles.³⁸ Comparing the structure of different proteins adsorbed on the

same particles revealed that “soft” proteins (BSA, hemoglobin) are more susceptible to perturbation than “hard” proteins (cytochrome *c*, RNase).³⁹ Solely differences in the size of particles with otherwise identical composition are known to cause a completely different behavior of adsorbed proteins.^{40,41} Remarkably, studies imply that the protein structure and activity is best maintained when it is adsorbed on smaller particles. This behavior is explained with a smaller contact patch and a lower electrostatic potential for smaller particles.⁴⁰ This lead to less perturbation of the protein conformation by electrostatic influences as seen in CD spectroscopy.⁴¹ This multitude of scientific results show a picture where the conformational integrity of a protein is vastly depending on individual properties of the protein:nanoparticle system.

The spatial orientation of individual proteins is difficult to analyze. Indirect methods have been used to probe the orientation of adsorbed protein molecules, including studies with fluorescence markers⁴² and molecular simulations.⁴³ In the latter case explicit-solvent molecular dynamics simulations were used to predict the adsorption orientation of chymotrypsin and lysozyme on amorphous silica from DLVO forces. Based on the main assumption that the adsorption on charged hydrophilic surfaces is dominated by electrostatic forces the electrical dipole moment was found to dominate the adsorption orientation. The protein orients in such a way that its electrical dipole moment is aligned perpendicular to the silica surface with the positive pole pointing towards the negatively charged surface. Results were most clear for chymotrypsin which has a significantly larger dipole moment.

In this thesis neutron small-angle scattering (SANS) was used as an alternative method for probing the orientation of adsorbed protein molecules. Cytochrome *c* was used as a model protein for structurally “hard” proteins with a large electric dipole moment. It was adsorbed onto silica particles and the pH was changed to understand the spatial response to a change in the dipole moment orientation. The scattering data is analyzed with a recently developed form factor model⁴⁴ and the results are compared with simulations of the spatial orientation of the protein dipole moment vector. The results are presented in Chapter 5.

1.4 Freezing/Melting of Concentrated Salt Solutions in Nanopores

As discussed in Section 1.1, the adsorption of proteins at solid surfaces is strongly affected by the ionic strength, as the electrostatic interactions are screened by added salt. Salt-specific effects may also be important, as small ions of the electrolyte may compete in different ways for adsorption sites at the surface.^{45,46} In order to study the relevance of such ion-specific effects, a comparative study of properties of concentrated electrolyte solutions in the pores of SBA-15 was performed.

As a sensitive way to monitor salt-specific or ion-specific effects, the melting behavior of the salt solutions in SBA-15 was investigated. Within the strong confinement of silica pores smaller than 10 nm the melting of water is observed at temperatures more the 50 K below the bulk melting point.⁴⁷ This implies that in narrow pores liquid water is stable down to temperatures below the homogeneous nucleation temperature of bulk ice (ca. 235 K). On hydrophilic surfaces a layer of a non-freezable water is located directly at the surface. In small pores the volume fraction of this layer becomes substantial and affects the properties of the total pore water to a significant extent.

This weathering of buildings stones and historical monuments is of great economic and cultural importance. This manifests in the amount of work which has been done on the field of pore crystallization induced deterioration of natural stone and concrete.^{48–50} From this research, it is known that different salt solutions cause vastly different damage pattern to limestone with moderately large pores (> 30 nm).⁵¹ Furthermore, the uptake of salts into the pores of stones increases the damage induced by halotolerant microbial populations found in aged walls.⁵² Regarding the processes of weathering damage, the research has been focused on understanding the mechanisms on the micron-sized pores of natural stone.

For this reason Chapter 7 of this thesis presents a comparative study of the depression of the eutectic temperature of a series of alkali halides in nanometer-sized pores of SBA-15 and MCM-41 silica. Large shifts of the eutectic temperature were found for salt solutions crystallizing in oligohydrates. Those bulky crystallites require a significant larger fraction of the pore volume and therefore, act as an additional or secondary confinement for the water ice. The results were evaluated as a function of the volume fraction of solid salt crystals in the frozen solution and modeled using a modified Gibbs-Thomson equation.

Chapter 2 Methods and Models

This chapter gives a more in depth overview about four important characterization techniques used in this work. Other experimental methods were used as routine experiments. A complete overview about all used methods and synthesis including the precise instrumentation and references can be found in the respective chapter.

2.1 Fluorescence Microscopy

In order to study the global structure of lysozyme-silica hetero-aggregates a combination of two complementary techniques has been used. The overall macroscopic aggregate structure of the flocculates has been studied using confocal laser scanning microscopy (CLSM). With this technique aggregate sizes from 200 nanometre to a few hundred micrometre are assessable. Properties of smaller structures were probed using fluorescence correlation spectroscopy (FCS). With this combination of experiments makes it possible to study the exact same systems over length scales of 4 orders of magnitude.

2.1.1 Confocal Laser Scanning Microscopy

Confocal laser scanning microscopy (CLSM) is a technique readily applied to visualize small specimen and is often used in the medical field but also other scientific divisions benefit from its capabilities. The fundamental base for this technique was pioneered by Marvin Minsky in 1957 with the US patent 3013467,⁵³ where he reported the principle working mechanism for a confocal microscope. Figure 2.1 shows the beam path of a confocal microscope setup with all important components.^{53,54} In this concept the use of a pinhole limits the light entering the detector to one specific focal plane in the sample providing a superior resolution in the z-direction (parallel to the beam path). Therefore the confocal microscope reduces the field of view to a small spot in the sample and the use of a movable sample stage gives the opportunity to scan through the sample in all three spatial dimensions. This specific setup provide many advantages over normal light microscopes. Just to name a few:

- Increased signal-to-noise ratio
- Reduced blurring of the image
- Higher effective resolution
- Images of “unusually thick and highly-scattered specimens”⁵³
- xyz-scanning through the sample

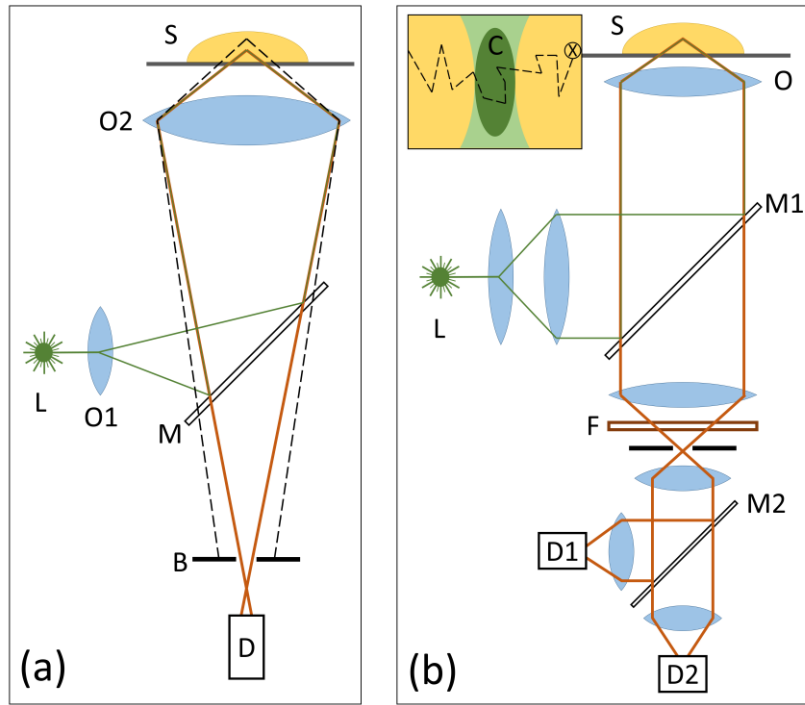


Figure 2.1: (a): Principle beam path of a confocal microscope working in the epi-illuminating mode (one lens is used simultaneously as objective and condenser lens). With the sample S, the objective O2, a dichromatic mirror M, the pin hole B, the detector D, the objective O1 and the light source (laser) L. (b): Beam path for a FCS experiment with the light source (laser) L, the sample S, dichromatic mirrors M1 and M2, a filter F and 2 detectors D1 and D2. In the sample the specimen x diffuses through the confocal volume C and emits a fluorescent signal.

With the wider availability of laser systems the first confocal laser scanning microscope was developed by Davidovits and Eggers and the first images of cells were published in 1971.⁵⁵ In 1983 Åslund and co-workers constructed the first CLSM, where a stack of pictures were taken and later visualized in 3D.⁵⁶

In the following decades the popularity of this technique grew and ultimately it evolved to a standard in biomedical research and related fields. Its latest improvement was pioneered by Hell and Wichmann, who developed the idea for a microscope, which is capable of a resolution below the diffraction limit.^{57,58} Such an STED-microscope (stimulated emission depletion) has a resolution far below the diffraction limit up to a molecular level.⁵⁹ The resolutions of a conventional fluorescence CLSM is defined as:⁶⁰

$$r_{\text{lateral}} = \frac{0.4\lambda}{NA} \quad \text{and} \quad r_{\text{axial}} = \frac{1.4\lambda n}{NA^2} \quad (2.1)$$

Where λ the wavelength, n is the refractive index and NA is the numerical aperture of the used objective. For typical conditions (as used for experiments presented in Chapter 4) it gives a lateral resolution of 163 nm.

In the here reported experiments a Leica TSC SP5 II equipped with an HCX PL APO CS 63.0×1.20 water UV immersion objective was used to collect stacks of images with different focal planes. The total confocal volume was $123 \times 123 \times 123 \mu\text{m}^3$ with a voxel resolution of $0.5 \times 0.5 \times 0.5 \mu\text{m}^3$. Detailed experimental parameters and information about the data treatment are given in Chapter 4.

2.1.2 Fluorescence Correlation Spectroscopy

FCS measures the fluctuation of a fluorescence signal from a small volume of the sample as a function of time. This technique uses a confocal microscope (see Section 2.1.1) and its opportunity to imaging a very small volume. The first application published in literature dates from 1972, where Magde et al. reported a data for the binding of ethidium bromide to DNA.⁶¹ The principle beam path of a FCS experiment is given in Figure 2.1b.

The fluorescence correlation spectroscopy (FCS) was used to assess objects which were too small for imaging with the afore mentioned CLSM. With this combination it was possible to keep the experimental parameter largely unchanged and also to gain information about different stages of the aggregation process for a broad range of length scales.

In a FCS experiment the size is not measured directly but derived indirectly via the diffusions kinetic of the individual components in the observation volume. Stokes-Einstein equation (Eq. 2.2) was used to calculate the hydrodynamic radius R_h from the diffusion coefficient D_f .

$$R_h = \frac{k_B T}{6\pi\eta D_f} \quad (2.2)$$

Where k_B is the Boltzmann constant, T the temperature and η the viscosity of the surrounding solution. All parameters are known or kept constant within an experiment except the diffusion constant. In order to obtain the diffusion constant from the time resolved fluorescent signal the autocorrelation function $G(\tau)$ needs to be derived with Equation 2.3.⁶²

$$G(\tau) = \frac{\langle \delta I(t) \cdot \delta I(t + \tau) \rangle}{\langle I(t) \rangle^2} \quad (2.3)$$

$I(t)$ is the fluorescence intensity at the time t , $\delta I(t)$ and $\delta I(t + \tau)$ are the intensity fluctuations at the time t or $t + \tau$ around $I(t)$, τ is the lag time and $\langle I(t) \rangle$ is the time averaged intensity, equivalent to:

$$\langle I(t) \rangle = (1/t) \int_0^t I(t) dt \quad (2.4)$$

The characteristic lag times for each diffusing component were extracted from the experimental autocorrelation function $G(\tau)$ using a fitting function derived for a free diffusing object in a 3d-Gaussian profile.⁶³

$$G(\tau) = \sum_i \rho_i \left(1 + \frac{\tau}{\tau_{D,i}}\right)^{-1} \left(1 + \frac{\tau}{\xi^2 \cdot \tau_{D,i}}\right)^{-1/2} \quad \text{mit} \quad \rho_i = \frac{Q_i^2 \cdot N_i}{(\sum_j Q_j \cdot N_j)^2} \quad (2.5)$$

With $\tau_{D,i}$ beeing the characteristic lag time of the component i and ξ the aspect ratio of the Gaussian profile ($V_G = \pi^{3/2} \cdot w_0^3 \cdot \xi$). With the help of the weighting parameter ρ_i and the quantum yield Q_i it is possible to calculate the number ratio of each component i . Assuming an equal quantum yield for all components leads to:

$$\langle N \rangle = \frac{1}{\sum_i \rho_i} \quad (2.6)$$

In many cases the experimental autocorrelation function shows a significant intensity signal at small lag times, usually related to fast transitions from a triplet state. To account for this process an additional factor was introduced.

$$G(\tau) = \frac{1 - \theta + \theta \cdot e^{-\tau/\tau_\theta}}{1 - \theta} \sum_i \rho_i \left(1 + \frac{\tau}{\tau_{D,i}}\right)^{-1} \left(1 + \frac{\tau}{\xi^2 \cdot \tau_{D,i}}\right)^{-1/2} \quad (2.7)$$

Here θ is the proportion of fluorophores in a triplet state and τ_θ the respective lag time. Finally, the arising lag times can be converted to the diffusion constants via Equation 2.8.

$$\tau_{D,i} = \frac{w_0^2}{4D_f} \quad (2.8)$$

2.2 Small Angle Neutron Scattering

Some of the most valuable tools to study the shape and interaction at the nanoscale are scattering methods. Modern colloidal and surface science is vitally dependent on those experimental techniques to determine particle size, dispersion stability or particle mobility. Especially, small angle X-ray scattering (SAXS) has proven to be a capable tool to characterize the interactions between the particles in the presence of proteins.^{29,31}

One of the model system treated in this theses, silica and lysozyme, was examined using X-ray scattering in great detail. In particular, the pH modulated interaction of the protein silica particle aggregates was deduced to a sticky hard sphere potential.³¹ In the following work this finding was further specified to a range of salinities.³² Combining these results with data from other methods Bharti et al. was able to identify specific interaction stages of the silica particles with attached lysozyme, depending on the external conditions. These findings could be generalized to cytochrome *c*, another hard protein with a similar isoelectric point than lysozyme.⁶⁴

These results were made possible by the fact that the silica particles and the surrounding medium have a large difference in the electron density. This ensures a strong X-ray scattering signal which can be easily detected with modern laboratory equipment. As the protein shows only a small contrast difference, the resulting intensity curve originate nearly entirely from the particles in the system. This circumstance almost intrinsically neglects the information about the state of the used protein. That the information about the protein adsorbed on the particles are anything but negligible has been shown by several studies. Vertegel et al. presented circular dichroism (CD) spectroscopy results of adsorbed lysozyme indicating a particle size sensitive nature of the protein adsorption. A similar effect on the conformational structure of human carbonic anhydrase was published in the same year by Lundqvist et al. (for details see Section 1.1).^{40,41}

2.2.1 Technical Background

Small angle neutron scattering (SANS) was used to expand the capabilities of scattering experiments so the information about both, the particles and the protein, can be retained. In contrast to X-rays neutrons are scattered by the nuclei. This gives rise to entirely different contrast scenarios compared to SAXS. A system consisting of cytochrome *c* adsorbed on silica particles in deuterium oxide (D₂O) was chosen. Cytochrome *c* and silica show a very similar difference in the scattering length density (SLD) from D₂O towards neutrons. This ensures that the resulting scattering signal arises from the complete ensemble of silica particle and adsorbed protein.

In a neutron scattering experiment the sample is irradiated by a beam of neutrons (Fig. 2.2 a). These neutrons are produced in research neutron sources, typically an atomic reactor or a spallation source. These sources produce free neutrons with a distribution of wave length and propagation directions. For a successful SANS experiment it is a prerequisite to know these two parameters. To select one wavelength from the spectrum a velocity selector is used. This form of monochromator made use of the particle character of neutron matter waves and let only pass neutrons of a certain velocity. Collimation of the beam is typically ensured by

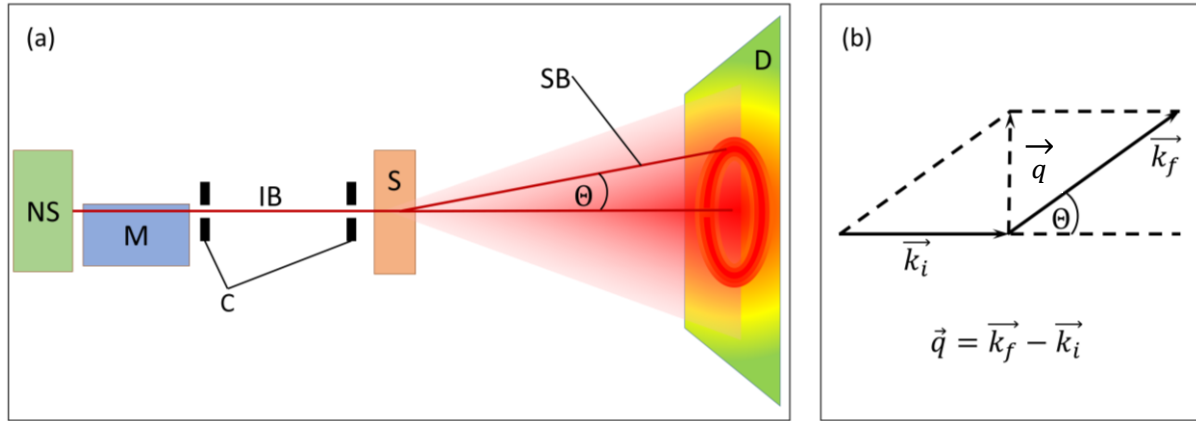


Figure 2.2: (a): Schematic view of a SANS setup. The incident beam (IB) of neutrons is generated in the neutron source (NS) and passed through a monochromator (M) to select the desired wavelength. Followed by a number of collimation slits (C) and the sample (S). The intensity of the scattered beam (SB) is measured with the detector (D). (b): Schematic view of the geometry of an elastic scattering event. The wave vector of the incoming neutron \vec{k}_i and of the (at an angle θ) scattered neutron \vec{k}_f sum up to the scattering vector \vec{q} according to Equation 2.10.

a set of slits placed at variable distances depending on the necessary beam quality. The collimated and monochromatic neutron beam is then scattered at the sample. After that, the scattered beam is passing through an evacuated chamber towards the neutron detector. As neutrons do not readily interact with matter it takes special materials to efficiently detect the neutron flux. Often ^3He or BF_3 proportional detectors are used. The detector can be placed at variable distances to increase the accessible angular range. When the detector is placed close to the sample, it is possible to measure larger angles and long distances between the sample and detector allow very small angles.

In scattering experiments it is useful to represent the scattering intensity curves as a function of the scattering vector q . The scattering vector q is dependent on the wavelength λ of the incident beam and the scattering angle θ . Equation 2.9 gives the mathematical expression of relation of these three measures.

$$q = \frac{4 \cdot \pi \cdot \sin \theta}{\lambda} \quad (2.9)$$

Considering an elastic scattering process, without energy transfer during that scattering event, the scattering vector can be described as the difference between the incoming wave vector \vec{k}_i and the scattered wave vector \vec{k}_f (Eq. 2.10). This relation is depicted as a scheme in Figure 2.2b.

$$\vec{q} = \vec{k}_f - \vec{k}_i \quad (2.10)$$

A scattering intensity curve $I(q)$ contains information about the size and shape of the scatterer (form factor) as well as about the interactions between the individual scatterers (structure factor). These properties can be extracted from the data by fitting with an appropriate analytical

model or comparing with numerical simulations. In the presented case of cytochrome *c* adsorbed on silica beads a ‘raspberry-type’ model was used to fit the intensity profile. Further details on this very model are given in Section 2.2.2 and the data analysis and the detailed results are presented in Chapter 5.

2.2.2 Raspberry Form Factor Model

The scattering intensity $I(q)$ can be described as a product of different factors by the following equation (Eq. 2.11)

$$I(q) = \varphi \cdot \Delta\rho^2 \cdot V \cdot P(q) \cdot S(q) \quad (2.11)$$

Where φ is the volume fraction of the scattering entities, V is the volume of the single scatterer, $\Delta\rho$ is the scattering length density (SLD) difference of the scatterer and the surrounding medium, $P(q)$ is the form factor and $S(q)$ is the structure factor. The difference of the scattering length density $\Delta\rho$ is often called the scattering contrast and can be calculated with the following equation.

$$\rho = \sum_i b_i \frac{\delta N_A}{m} = N \sum_i b_i \quad (2.12)$$

Where δ is the bulk density of the material, m is the relative molar mass, N is the number density of the scatterers and b_i is the scattering length of the nucleus i .

The structure factor $S(q)$ in Equation 2.11 describes the global arrangement of the scattering particles in the sample and mathematically relates to the Fourier transform of the pair correlation function. Therefore, an analysis of the structure factor can be used to investigate the interaction and the structure formation inside the dispersion. This has been done in great detail in earlier works^{31,32} and is briefly summarized in the introduction.

The form factor $P(q)$ in Equation 2.11 contains information about the individual scattering particle. Generally, the form factor is the Fourier transform of the pair distribution function. For the analysis in Chapter 5 a specific form factor was used to account for the special ‘raspberry-like’ shape of the cytochrome *c*/silica composite. This model was developed by Kjersta Larson-Smith, Andrew Jackson and Danilo C. Pozzo to describe the scattering signal from Pickering emulsions.⁴⁴ Starting from the work of Pederson⁶⁵ for the scattering signal from polymer micelles they evolved the model to account for differently sized small particles placed at the interface of an bigger spherical particle. This complex particle shape is sketched in Figure 2.3. The derived equation for ‘raspberry-like’ particles is given in Equation 2.13.

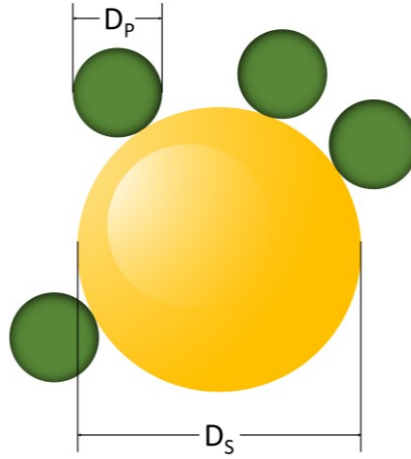


Figure 2.3: Schematic visualization of a ‘raspberry-like’ particle composite with a central large particle and several smaller particles attached to its surface. The central particle has the diameter D_s and the smaller particles have the diameter D_p .

$$I(q) = \left(\phi_s V_s \Delta \rho_s^2 + \frac{\phi_p^2 \phi_p^a V_s}{\phi_s} \Delta \rho_p^2 \right) P_{ps}(q) + (\phi_p (1 - \phi_p^a) V_p \Delta \rho_p^2) \Psi_p^2(q) \quad (2.13)$$

Where ϕ_p and ϕ_s are the total volume fractions of smaller and bigger central particle respectively, ϕ_p^a is the fraction of small particles bound to the surface of the bigger particle, V_p and V_s are the volumes of the particles, $\Delta \rho_p$, and $\Delta \rho_s$ are the scattering length density contrasts of the particles and $\Psi_p^2(q)$ is the form factor of the smaller particles. $P_{ps}(q)$ is the form factor of the entire ‘raspberry-like’ particle (Eq. 2.14).

$$P_{ps}(q) = \frac{1}{M^2} \left[(\Delta \rho_s)^2 V_s^2 \Psi_s^2 + N_p (\Delta \rho_p)^2 V_p^2 \Psi_p^2 + N_p (N_p - 1) (\Delta \rho_p)^2 V_p^2 S_{pp} + 2 N_p \Delta \rho_s \Delta \rho_p V_s V_p S_{ps} \right] \quad (2.14)$$

with

$$M = \Delta \rho_s V_s + N_p \Delta \rho_p V_p$$

Where N_p is the average number of small particles at the surface of the large particle, M is a prefactor taking into account the total scattering length density of the complete ‘raspberry-like’ composite, S_{ps} and S_{pp} are the large-small and small-small particle correlation terms (Eq. 2.15 and 2.16).

$$S_{ps} = \Psi_s \Psi_p \frac{\sin(q(R_s + \delta R_p))}{q(R_s + \delta R_p)} \quad (2.15)$$

$$S_{pp} = \Psi_p^2 \left[\frac{\sin(q(R_s + \delta R_p))}{q(R_s + \delta R_p)} \right]^2 \quad (2.16)$$

$$\Psi_s = \frac{3[\sin(qR_s) - qR_s \cos(qR_s)]}{(qR_s)^2} \quad (2.17)$$

$$\Psi_p = \frac{3[\sin(qR_p) - qR_p \cos(qR_p)]}{(qR_p)^2} \quad (2.18)$$

Were R_s and R_p are the radii of the central larger particle and the smaller particles sitting at its surface. The factor δ relates to the fraction of R_p being outside of the central particle. This is important for Pickering emulsions, where the small particles immersed in the central droplet to some extent. In the presented case of proteins adsorbing at solid silica particles this does not apply and the factor δ was kept at the value 1, as the protein cannot penetrate the central silica particle.

This form factor also accounts for free smaller particles in the dispersion and not attached in the interface of the bigger sphere. It need to be mentioned that the smaller particles are treated as monodisperse particles. However, the polydispersity of the bigger particle can be analyzed.

2.3 Protein Dipole Moment

The main backbone of a protein is a polymer consisting of single α -amino acids bound together by a condensation reaction forming a peptide bond. Every amino acid carries a residue at the α -carbon atom which can range from a simple hydrogen atom (glycine) to more complex side chains like an imidazole group (histidine). Some of the amino acids found in proteins carry ionizable side chains like carboxy acids (aspartic acid) or amino groups (lysine). Depending on the pH these groups are in a specific protonation state and thus differently charged. This leads to different net charges of the protein and to a different charge distribution on its surface. As a

consequence of this asymmetric electric charge distribution proteins possess an electric dipole moment. The dipole moment vector $\vec{\mu}$ is defined according to Equation 2.14 as the vector sum of all charges q_i at the distance r_i from a constant reference point r_r . Typically the center of mass is chosen as reference point and the resulting vector is pointing from the negative towards the positive charge.

$$\vec{\mu} = \sum_i q_i (\vec{r}_i - \vec{r}_r) \quad (2.19)$$

In the case of protein molecules this is not straight forward as several charges and hundreds of atoms need to be considered. A combination of different software packages were used in order to calculate the electric dipole moment vector for cytochrome *c*. This section gives a summary of the process needed to calculate the dipole moment vector and the final results are shown in Chapter 5.

The foundation of the calculation are the protein structure and the precise atomic positions of cytochrome *c*. For all calculations the solution structure 2GIW from reduced horse heart cytochrome *c* was used as provided by the RCSB protein data bank (PDB).⁶⁶ This structure includes the main protein backbone for cytochrome *c* as well as the heme *c* group.

In order to assign the correct charges for a series of solution pH the software PDB2PQR was used.^{67,68} This package assigns the titration state of each ionizable group in the structure for a chosen pH value. The pK_a values were predicted by PROPKA^{69,70} on the basis of the proteins 3-dimensional structure. This step is crucial as the pK_a value of a side chain in close vicinity to other groups can vary significantly.^{71,72} At the end of this process a single .pqr file was generated containing both the atomic positions and the correct protonation state of each functional group.

The electric dipole moment at the given pH is calculated with a python code written by Miguel Ortiz-Lombardia.⁷³ This code calculates the magnitude and the direction of the dipole moment vector from the position of each charge relative to the center of mass. Results were visualized with the program UCSF Chimera.⁷⁴

In a final step the electrostatic potential on the surface of the protein was visualized using the Adaptive Poisson-Boltzmann Solver (APBS) plugin for UCSF Chimera. APBS is a software designed to solve the equations of continuum electrostatics for large molecules such as proteins.⁷⁵ The full documentation of the software can be found online.⁷⁶

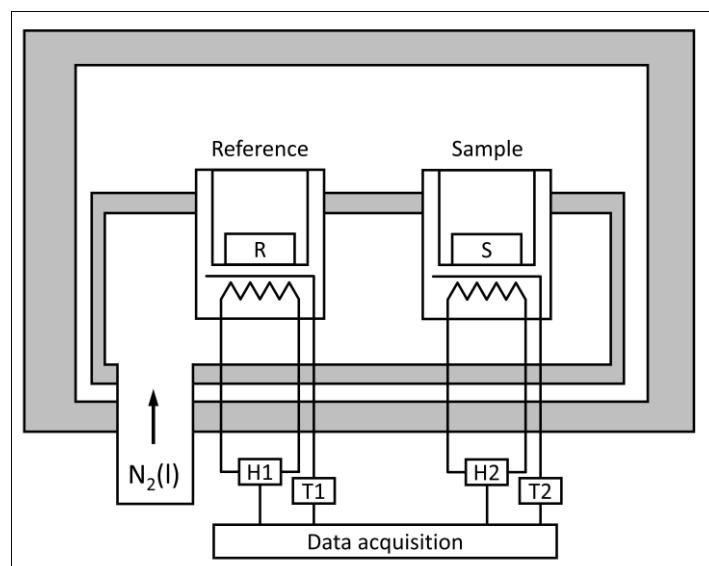


Figure 2.4: Schematic drawing of a power-compensated DSC. Two identical furnaces (Reference and Sample) with individual heating (H1 and H2) and temperature sensors (T1 and T2) are placed in an insulated chamber and cooled (in the present case with liquid nitrogen). The temperature of each furnace cell is controlled by a computer-aided data-acquisition and controlling unit. The power difference between reference and sample is measured and converted into the heat flow.

2.4 Differential Scanning Calorimetry

As explained in Section 1.4 the phase behavior of binary mixtures was investigated as part of this thesis (results are presented in Chapter 7). One of the best tools to experimentally determine the phase transition temperatures inside narrow pores is differential scanning calorimetry (DSC). This technique has been used in the past to study the phase behavior of pure liquids in silica pores of different size.

In a DSC experiment the difference in heat flow between a sample and a reference is measured while both are heated to the same temperature. The principle setup scheme is shown in Figure 2.4. The experimental setup consists of two identical heatable sample chambers which are placed in thermal contact to a liquid nitrogen cooled heat sink. Both sample chambers are heated to a programmed temperature higher than the temperature of the heat sink. The power needed to maintain/increase the sample temperature is measured for each sample cell. Difference in heat flow between sample and reference cell are detected as a function of the sample temperature and provide the information about phase transitions in the sample. This type of DSC technique is also known as power-compensated DSC.⁷⁷

For one typical experiment approximately 50 mg of mesoporous silica material were contacted with 100 μL of an aqueous solution of the desired salt and placed in a sealed aluminum sample container. During the measurement it is crucial that the scan speed is chosen correctly. A DSC experiment provides the best signal to noise ratio at high scan speeds but very

high scan speeds are prone to a smearing of the signals. Most experiments were conducted with a temperature scan speed of 0.5 K min^{-1} . This value was experimentally determined in earlier studies in the group of Prof. Findenegg.⁷⁸ For a few samples a variety of scan speeds (0.5 , 1 , 3 K min^{-1}) were used in order to combine both, good temperature resolution and sensitivity.

Chapter 3 Characterization of Protein Adsorption onto Silica Nanoparticles: Influence of pH and Ionic Strength¹

3.1 Introduction

Globular proteins are strongly adsorbed to hydrophobic as well as hydrophilic interfaces due to the patchwise hydrophobic/hydrophilic character of their surface. The 'multipolar' nature of proteins – as distinct from 'bipolar' surfactants – leads to specific phenomena in the adsorption onto nanoparticles and emulsion droplets;⁷⁹ whereas surfactants cause a stabilization of dispersions and emulsions, adsorption of proteins makes the particles/droplets 'sticky', when attractive patches exist on opposite sides of the protein molecule. In such cases, the adsorption of the protein can cause bridging aggregation and flocculation of the particles.^{31,32,79,80} This chapter presents a study of protein adsorption onto silica nanoparticles under the influence of this protein-induced flocculation.

The interaction of proteins with nanoparticles (NPs) plays an important role in biotechnology and biomedical applications. In a biological environment, the NPs are exposed to a variety of proteins which may or may not be adsorbed to the particle surface, depending on the strength of protein-particle interaction.⁸¹ In the past decade, many aspects of protein interaction with NPs have been investigated.⁸² It has been found that the strength of protein – surface interaction and the secondary structure of adsorbed proteins is affected by the NP size^{40,41,83,84} and the hydrophilic or hydrophobic nature of the NPs.^{84–87} Electrostatic interactions play an important role in the adsorption of proteins at hydrophilic/charged surfaces. It is thought that conformationally stable ('hard') proteins are adsorbed at charged surfaces only under electrostatically attractive conditions.⁶ Specifically, at a negatively charged surface, only proteins with a net positive charge should be adsorbed, i.e., proteins having an isoelectric point IEP higher than the pH of the solution. However, recent studies of protein adsorption into polyelectrolyte brushes have shown that a protein can be strongly adsorbed into a brush having the same charge as the protein, i.e., adsorption takes place at the 'wrong side' of its isoelectric point.^{88–90} It was proposed that this is a consequence of the 'patchy' charge distribution on the protein surface, which implies that a protein of net negative charge can still have patches of positive charge. When a protein near the surface is oriented such that a positive patch points toward the negatively charged surface, an attractive interaction of entropic origin can arise as a result of the release of counter-ions.^{88,91} In fact, it has long been recognized that the binding

¹ Reproduced with permission from J. Meissner, A. Prause, B. Bharti, G. H. Findenegg, *Colloid Polym Sci* **2015**, 293, 3381. Published open access under the Creative Commons Attribution 4.0 International license (<https://creativecommons.org/licenses/by/4.0/>).
<http://dx.doi.org/10.1007/s00396-015-3754-x>

strength of a protein is determined by a small number of charged groups located in the contact region on the surface of the protein.⁹² An alternative explanation for protein adsorption at the wrong side of the isoelectric point is based on the charge regulation effect. Since the ionizable groups on the protein represent weak acids and bases, their charge is dependent on pH, and thus, their degree of dissociation will be influenced by the local electrostatic field near the surface. Next to a negatively charged surface, the pH is lower and the protein charge more positive than in the bulk solution.^{93,94}

The role of electrostatic interactions in protein adsorption onto silica and metal oxide surfaces has been considered in many studies.^{95–98} Commonly, it is found that the adsorbed amount as a function of pH reaches a maximum near IEP of the protein.^{95,97} Since the net charge is zero at IEP, the electrostatic repulsion between adsorbed protein molecules is at a minimum, and thus, the molecules can attain a closer packing at the surface than when carrying a net charge. Van der Veen et al.⁹⁷ performed a comparative adsorption study of two proteins of different IEP at a macroscopic silica surface. It was found that added electrolyte affects the protein adsorption at the two sides of IEP in opposite ways, which indicates the importance of electrostatic protein – protein and protein – surface interactions. Here, we present a similar comparative study for the adsorption of proteins at silica nanoparticles (SiNP). In this case, the adsorption behavior may also be affected by the surface curvature and the protein-induced aggregation of the particles, which in turn is also dependent on pH and ionic strength.^{31,32} Protein adsorption onto SiNP can be determined either by measuring the depletion of the solution after equilibration with the SiNP, or indirectly from the increase in size of the SiNP due to the formation of a protein layer. The latter method avoids errors in the measurement of protein concentration, but it is indirect, as it relies on a suitable adsorption isotherm equation.⁹ A variety of isotherm equations for protein adsorption have been discussed in the literature, from classical ligand-binding models developed in biochemistry^{99,100} to models derived from modern statistical mechanics.¹⁰¹ Most of the models assume that adsorption is limited to some maximum level, usually a monolayer of protein molecules. Although this will be a reasonable assumption in many circumstances, weaker adsorption beyond a monolayer has also been reported, particularly in a pH range close to the isoelectric point of the protein.³¹

Lysozyme (Lyz) and β -lactoglobulin (β -Lg) were chosen for this comparative adsorption study. The two proteins have similar size and molar mass but a widely different isoelectric point. Important characteristics of the two proteins are given in Table 3.1. Lyz is a conformationally stable (“hard”) protein due to 4 intramolecular disulfide bonds, and no significant association of the protein occurs at concentrations relevant in the present context. β -Lg has only two intramolecular disulfide bonds and is less stable than Lyz toward partial unfolding. It represents a mixture of two generic variants (A and B) differing only in two positions along the chain.¹⁰² Depending on pH, temperature, ionic strength, and concentration, β -Lg is present in different oligomeric forms.¹⁰³ It was of interest to find out how these

differences in surface charge distribution and aggregation behavior affect the adsorption of the two proteins at SiNP.

3.2 Materials and Methods

3.2.1 Materials

Ludox TMA colloidal silica (Sigma-Aldrich) was used as the adsorbent in this study. The Ludox dispersion was dialyzed for 5 days against DI water (water changed 3 times per day) to remove remaining salt. Its mean particle diameter D_s was 21 nm (determined by dynamic light scattering). Its specific surface area a_s was 128 m²/g (value from the manufacturer), in agreement with the geometric surface area derived from the particle diameter, $a_{\text{geom}} = 6/\rho_s D = 130 \text{ m}^2/\text{g}$, based on a mass density of silica $\rho_s = 2.20 \text{ g/cm}^3$. The value of $a_s/a_{\text{geom}} = 1.02$ indicates a low surface roughness of the particles.¹⁰⁴ The electrophoretic mobility of the Ludox particles was determined by electrophoretic light scattering of a 1 wt% dispersion as described elsewhere,³¹ using a Nano-Zetasizer (Malvern Instruments, UK). Three measurements, each consisting of at least 50 runs, were performed for each sample.

Lysozyme from chicken egg white lyophilized powder (Sigma-Aldrich, $\geq 40,000$ units/mg protein, lot SLBH9534V, purity $\geq 90\%$) and β -lactoglobulin from bovine milk (Sigma Aldrich, lot SLBC4958V, purity $\geq 90\%$) were used in this study.

3.2.2 Protein Adsorption Measurements

The amount of protein adsorbed on the SiNP was determined by measuring the depletion of the supernatant solution after equilibration of the sample. For each adsorption isotherm at given pH and salt concentration, a stock solution of buffer (10 mM formiate, MES, BICINE, or CAPS) was freshly prepared and adjusted to the desired pH with aqueous HCl or NaOH solution (1 M). Stock solutions of protein (10 mg/mL) and NaCl (250 mM) were then prepared in the buffer

Table 3.1: Characteristic parameters of the proteins.

Protein	Dimensions	Molar weight MW	Isoelectric point IEP
	nm	kDa	-
Lysozyme	$3 \times 3 \times 4.5$	14.3	11.1 ²³
β -lactoglobulin	$3.6 \times 3.6 \times 3.6$	18.4	5.2 ³⁰

solution. A portion of dialyzed Ludox TMA dispersion (about 30 wt%) was diluted in a volume ratio 1:2 with buffer solution to obtain the Ludox TMA stock solution (about 10 wt%). The mass fraction of silica in this stock solution was checked gravimetrically for each adsorption isotherm. The three stock solutions (SiNP, protein, and buffer) were then mixed in known proportions to arrive at eight different protein concentrations (0.5 – 5 mg/mL), three different NaCl concentrations (0, 25, and 100 mM), and a constant mass fraction of Ludox TMA (about 1 wt%). The samples were equilibrated for 20 h at 20 °C in closed vials using a thermo-mixer. After equilibration, the samples were centrifuged for 3 h at 15,000 rpm (21,000g) to separate the supernatant from the silica. The possibility of systematic errors caused by sedimentation of non-adsorbed protein during centrifugation was checked by determining sedimentation isotherms of β -Lg in the absence of SiNP but under otherwise the same conditions (protein concentration, pH, salt concentration and centrifugation time) as in the adsorption measurements. It was found that this error was negligibly small under the experimental conditions.

Protein concentration in the supernatant solution was determined by UV-vis spectrometry. Sample spectra were compared to a protein standard (1 mg/mL), prepared from the same protein stock solution, in the wavelength range 265 – 300 nm. The best-fit value of the concentration was obtained by minimizing the sum of square deviation in absorbance from the concentration standard in the chosen wavelength range.¹⁰⁵ The surface concentration Γ of adsorbed protein (mass per unit surface area) was calculated from the depletion of the supernatant solution by the relation

$$\Gamma = \frac{V(c_0 - c_{eq})}{m_s a_s} \quad (3.1)$$

where V is the volume of protein solution of initial mass concentration c_0 and final concentration c_{eq} after equilibration with a mass m_s of silica of specific surface area a_s . The adsorbed amount was also expressed by the number of protein molecules per silica particle,

$$N = \Gamma \frac{N_A \rho_s a_s D^3 \pi}{6 M_p} \quad (3.2)$$

where M_p is the molar weight of the protein and N_A the Avogadro constant.

3.2.3 Adsorption Isotherm Equation

The liquid-phase version of the Guggenheim – Anderson – De Boer (GAB) model was used to represent the protein adsorption data. Similar to the BET relation, the GAB multilayer gas

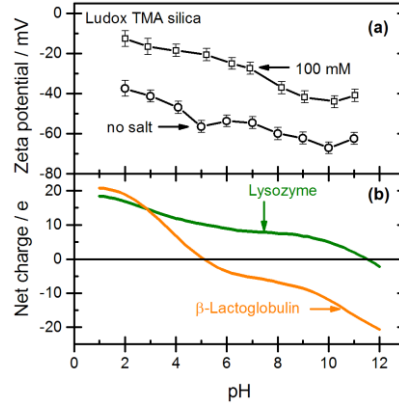


Figure 3.1: (a) Zeta potential of Ludox TMA silica particles as a function of pH for two different ionic strengths (see Table 3.1). (b) Estimated net charge of lysozyme and β -lactoglobulin as a function of pH.

adsorption model¹⁰ assumes that the state of adsorbate molecules in the second and all higher adsorption layers is the same, but different from that in the first layer. A further assumption of the GAB model is that the state of adsorbed molecules in the second and higher layers is also different from the bulk liquid state. The liquid-phase version of the GAB model takes up the concept of two distinct adsorption states: There are N_m equivalent adsorption sites per unit area to which adsorbate molecules bind strongly, and each occupied site can accommodate successively further adsorbate molecules in a weaker sorption state. This three-parameter adsorption isotherm has the form¹¹

$$\Gamma = \Gamma_m \frac{K_S c_{eq}}{(1 - K_L c_{eq})(1 + K_S c_{eq} - K_L c_{eq})} \quad (3.3)$$

where $\Gamma_m = N_m M_P / N_A$ is the surface concentration of strongly adsorbed protein, K_S is the adsorption constant for molecules in the strong adsorption state, and K_L the adsorption constant of the weak adsorption state. Equation 3.3 reduces to the Langmuir equation when $K_L = 0$, but it yields values of Γ greater than Γ_m at high concentrations c_{eq} when $K_L > 0$. The familiar BET equation for vapor adsorption is recovered from Equation 3.3 by setting $K_L c_{eq} = p/p_0 > 0$ and introducing the parameter $C = K_S/K_L$.

3.3 Results

3.3.1 Nanoparticle and Protein Characteristics

The electrophoretic mobility μ_e of the Ludox TMA NPs was determined at several pH values in the absence of salt and in 100 mM NaCl, and the zeta potential ζ was calculated from the

mobility by the Henry equation. The electrokinetic surface charge density σ_0 of the particles was estimated from the zeta potential using the Gouy-Chapman relation.¹⁰⁶ Results for μ_e , ζ and σ_0 for several pH values are collected in Table 3.1. The dependence of the zeta potential on pH is shown in Figure 3.1a. Note that the zeta potential of the Ludox TMA particles is negative in the entire pH range, i.e., no isoelectric point is observed down to pH 2.

The net charge of the proteins was estimated from the numbers of the individual acidic and basic amino acids and their respective acidity constants.¹⁰⁷ The dependence of the estimated net charge on pH is shown in Figure 3.1b. Both proteins have a high positive net charge at pH 2, but for β -Lg, the net charge falls off steeply with increasing pH and becomes negative above pH 5.2 = IEP. Lyz contains a larger number of basic amino acids than β -Lg; hence, its net charge falls off less steeply, and its isoelectric point is reached only at pH 11. Accordingly, in the case of lysozyme the protein and the silica particles are oppositely charged from pH 2 to pH 11. In the case of β -Lg the protein and silica particles are oppositely charged up to pH 5.2 but equally charged at higher pH.

Table 3.1: Electrophoretic mobility, zeta potential, and electrokinetic charge density of Ludox TMA silica nanoparticles as a function of pH without added salt and with 100 mM NaCl.

Added salt	pH	Ionic strength	μ_e	ζ	σ_0
		mM	$10^{-8} \text{m}^2 \text{s}^{-1} \text{V}^{-1}$	mV	E nm^{-2}
0 mM	2.0	10	-1.84	-37	-0.01
	3.0	1	-2.03	-41	-0.03
	4.1	7	-2.41	-47	-0.06
	5.0	1	-2.77	-57	-0.03
	6.0	4	-2.72	-54	-0.06
	7.0	9	-2.83	-55	-0.09
	8.0	3	-3.01	-60	-0.06
	9.0	8	-3.22	-62	-0.10
	10.0	3	-3.36	-67	-0.07
	11.0	8	-3.24	-63	-0.10
100 mM	2.0	110	-0.27	-13	-0.06
	2.9	101	-1.00	-17	-0.08
	4.0	106	-1.12	-19	-0.09
	5.2	101	-1.24	-21	-0.10
	6.2	106	-1.51	-25	-0.12
	6.9	109	-1.65	-27	-0.14
	8.2	104	-2.23	-37	-0.19
	9.1	108	-2.52	-42	-0.22
	10.2	104	-2.65	-44	-0.23
	11.0	108	-2.47	-41	-0.22

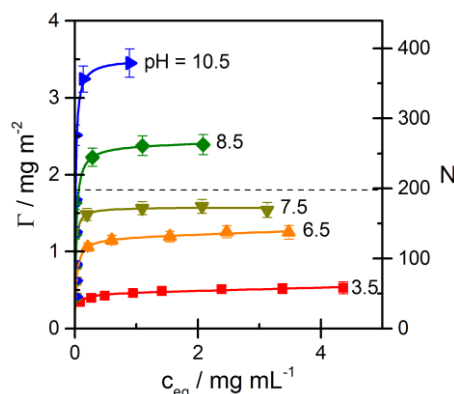


Figure 3.2: Adsorption isotherms of lysozyme on Ludox TMA for several pH values without added salt: Experimental data (symbols) and fits by the GAB model (lines). The adsorbed amount is expressed as protein mass per unit area (Γ) and by the mean number of protein molecules per silica particle (N). The monolayer capacity based on a dense packing of protein molecules in side-on orientation ($A_0 = 13.5 \text{ nm}^2$) is indicated by the dashed line.

3.3.2 Lysozyme Adsorption

The adsorption of Lyz on Ludox TMA SiNPs was studied in a pH range 3.5 to 11.2 in the absence of salt and in 25 and 100 mM NaCl solutions. Figure 3.2 shows adsorption isotherms (20 °C) for a series of pH values up to the isoelectric point in the absence of added salt. Adsorption is expressed by the surface concentration Γ (mg/m^2) and by the average number of protein molecules per silica particle (N) and is plotted against the concentration c_{eq} of protein in the equilibrated solution. The isotherms are of high-affinity type, i.e., sharply increasing at low concentrations and leveling off at higher concentrations. The adsorption level attained in the experimental concentration range is below $0.5 \text{ mg}/\text{m}^2$ at pH 3.5, but strongly increasing with pH to a value close to $4 \text{ mg}/\text{m}^2$ at pH 11.2 (not shown in Fig. 3.2). From the cross-sectional area of Lyz adsorbed side-on ($A_0 \approx 4.5 \text{ nm} \times 3 \text{ nm} = 13.5 \text{ nm}^2$), the monolayer capacity is about $1.8 \text{ mg}/\text{m}^2$, as indicated by the dashed line in Figure 3.2. It can be seen that this adsorption level is nearly reached at pH 7.5, but higher values are attained closer to IEP. A higher monolayer capacity (about $2.6 \text{ mg}/\text{m}^2$) would result from head-on adsorption of the Lyz molecules. However, molecular simulation studies indicate that side-on adsorption is the preferred orientation of Lyz on negatively charged silica surfaces.^{43,108} Hence, the results in Figure 3.2 indicate that adsorption exceeding a monolayer of protein molecules occurs at pH > 8.

Figure 3.3 illustrates the influence of added NaCl on the adsorption isotherm of Lyz at a low and a high pH. In both cases, the high-affinity character of adsorption isotherms is lost when salt is added, but the influence on the adsorption level at higher protein concentrations is

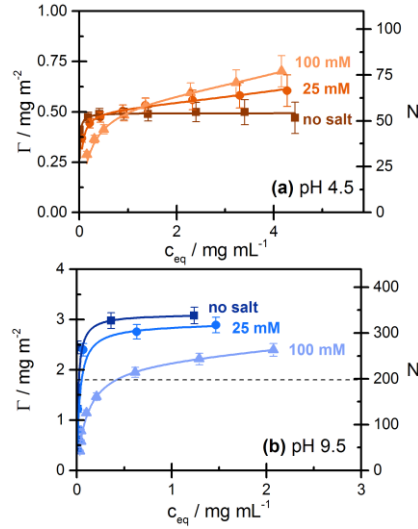


Figure 3.3: Adsorption isotherms of lysozyme on Ludox TMA: Influence of added salt at pH 4.5 (a) and pH 9.5 (b): filled square, no added salt; filled circle, 25 mM NaCl; filled triangle, 100 mM NaCl, and fits by the GAB model; see caption of Figure 3.2 for details.

different in the two pH regimes: At pH 4.5 (Fig. 3.3a), when the protein is highly charged, adsorption continues to increase in the presence of salt, becoming higher than the plateau value reached in the absence of salt. At pH 9.5 (Fig. 3.3b), when the adsorption level exceeds one nominal monolayer, added salt causes a significant decrease of the adsorption level at all protein concentrations studied in this work.

The experimental adsorption data can be represented by the GAB isotherm equation (Eq. 3.3), as shown by the full curves in Figures 3.2 and 3.3. Values of the parameters Γ_m , K_S and K_L obtained by fitting the adsorption data with Equation 3.3 are presented as a function of pH in Figure 3.4. The limiting surface concentration Γ_m of strongly adsorbed protein (Fig. 3.4a) is increasing with pH and reaches values above 3 mg/m² near IEP. Hence, in this pH region, the surface concentration of strongly bound protein clearly exceeds a monolayer of closely packed molecules. The adsorption constant K_S for the strongly bound protein (Fig. 3.4b), which relates to the high-affinity region of the adsorption isotherms, exhibits no systematic dependence on pH, but a systematic decrease with increasing salt concentration. The adsorption constant K_L of Lyz in the weakly bound state (Fig. 3.4c) is smaller by 2 – 3 orders of magnitude than K_S . Like K_S , it shows no systematic dependence on pH but some increase with the ionic strength. To quantify the contribution of the weak adsorption state to the overall adsorption, we introduce the adsorption ratio $\Gamma(c^*)/\Gamma_m$, where $\Gamma(c^*)$ represents the adsorbed amount at a reference concentration, c^* in the flat region of the isotherms as calculated by Equation 3.3. Values of $\Gamma(c^*)/\Gamma_m < 1$ indicate that at the chosen reference concentration, the adsorbed amount is lower than the limiting concentration Γ_m of strongly adsorbed protein, while $\Gamma(c^*)/\Gamma_m > 1$ implies that the weak adsorption state contributes to the overall adsorption. Figure 3.4d shows the adsorption ratio as a function of pH for a reference concentration $c^* = 2$ mg/mL. Values of

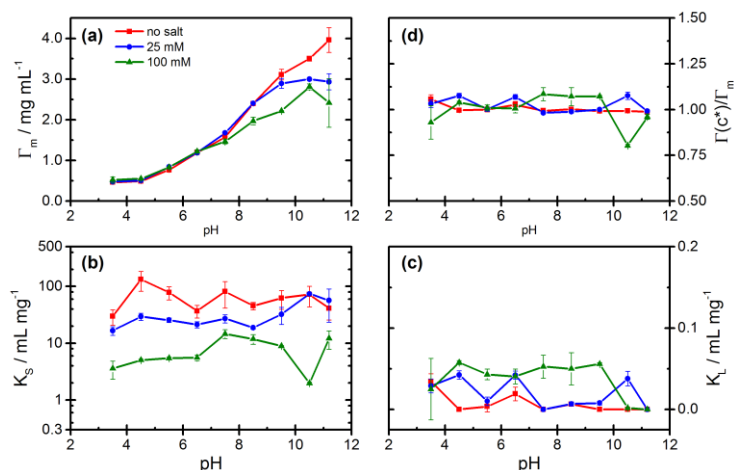


Figure 3.4: Lysozyme adsorption: Fit values of the GAB parameters as a function of pH for three ionic strengths (no salt, 25 mM, 100 mM NaCl): (a) limiting surface concentration Γ_m of strongly bound protein; (b) adsorption constant K_s ; (c) adsorption constant K_L ; (d) adsorption ratio $\Gamma(c^*)/\Gamma_m$ for $c^* = 2$ mg/mL (see text).

$\Gamma(c^*)/\Gamma_m$ close to 1 are found in the absence of salt, indicating that in this case all adsorbed Lyz is strongly bound. At $\text{pH} > 7$, where added salt causes a decrease of the adsorbed amount (Fig. 3.3), values of $\Gamma(c^*)/\Gamma_m > 1$ indicate that the salt-induced decrease of adsorption involves the participation of weak adsorption sites. These findings will be discussed in Section 4.4.

3.3.3 β -Lactoglobulin Adsorption

Adsorption isotherms of β -Lg on Ludox TMA for a series of pH values in the absence of salt are shown in Figure 3.5. It can be seen that adsorption sharply increases from pH 2 to pH 4 (Fig. 3.5a) and sharply decreases from pH 4 to pH 7 (Fig. 3.5b). All isotherms for $\text{pH} < 7$ exhibit a high-affinity adsorption regime, even at pH 2, where the limiting adsorption is only 0.2 mg/m^2 . Beyond this high-affinity regime, a further increase of adsorption with protein concentration is observed at pH values near IEP. This effect is most pronounced at pH 4. A monolayer of densely packed β -Lg molecules (cross-sectional area $A_0 \approx 3.6 \text{ nm} \times 3.6 \text{ nm} \approx 13 \text{ nm}^2$) corresponds to a surface concentration of ca. 2.3 mg/m^2 (dashed line in Fig. 3.5). This adsorption level is well exceeded at pH 4 but not at pH 5 (i.e., close to $\text{IEP} = 5.2$). At pH 6, when the net charge of the protein has changed from positive to weakly negative, there is still significant adsorption of the protein, but at pH 7 and higher, no adsorption of β -Lg is detected in the absence of salt.

The influence of salt on the adsorption of β -Lg at different pH values is shown in Figure 3.6, where the four panels demonstrate a reversal of the influence of salt on the protein adsorption in the range from pH 4 to 7: At pH 4 (Fig. 3.6a), the highest adsorption is found in the absence of salt and the lowest adsorption at 100 mM salt. Changing from pH 4 to pH 5

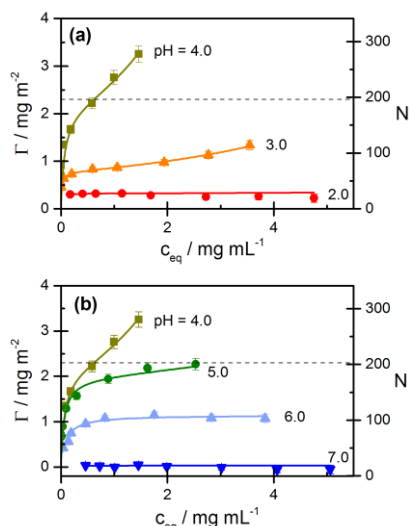


Figure 3.5: Adsorption isotherms of β -lactoglobulin on Ludox TMA for several pH values without added salt: (a) $\text{pH} \leq \text{pH } 4$; (b) $\text{pH} \geq \text{pH } 4$. Experimental data (symbols) and fits by the GAB model (lines). The monolayer capacity based on a dense packing of monomeric protein ($A_0 = 13 \text{ nm}^2$) is indicated by the dashed line; see also caption of Fig. 3.2.

(Fig. 3.6b) causes a drastic decrease of adsorption in the absence of salt, but no significant decrease at 25 or 100 mM salt; as a consequence, the adsorption at no salt is now intermediate between that at 25 and 100 mM salt. Changing from pH 5 to pH 6 (Fig. 3.6c) causes further strong decrease in adsorption at no salt, and also a strong decrease at 25 mM salt, but again, no decrease of adsorption at 100 mM salt. Finally, at pH 7 (Fig. 3.6d), the adsorption in the absence of salt has fallen to zero, and the adsorption at 25 mM salt has fallen below the adsorption at 100 mM salt, thus completing the inversion of the protein adsorption level as a function of salt concentration.

The adsorption data for β -Lg can again be represented by the GAB equation (Eq. 3.3), as shown by the full curves in Figures 3.5 and 3.6. The parameters Γ_m , K_S and K_L obtained from fits of the adsorption data and values of the adsorption ratio $\Gamma(c^*)/\Gamma_m$ at the reference concentration $c^* = 2 \text{ mg/mL}$ are shown as a function of pH in Figure 3.7. The limiting surface concentration Γ_m of strongly bound protein (Fig. 3.7a) increases sharply at low pH, reaching a maximum at pH 4–5 and falls off more or less steeply at higher pH values, depending on the salt concentration. The highest values of Γ_m , attained at pH 4–5 and low salt concentration correspond to nearly a monolayer of densely packed β -Lg monomers (2.3 mg/m^2). At pH above IEP = 5.2, the values of Γ_m demonstrate the inversion of the influence of salt on the protein adsorption in this pH range. Unlike Γ_m , the adsorption constant K_S of strongly bound protein (Fig. 3.7b) decreases in a monotonic way from low to high pH, without any singular behavior near IEP. It also decreases with increasing salt concentration, though to a lesser extent than in the case of Lyz. Remarkably, values of K_S well above 1 mL/mg are still found in a pH range where both the surface and the protein are negatively charged. In contrast to K_S , the adsorption constant K_L of β -Lg in the weakly bound state (Fig. 3.7c) exhibits a pronounced maximum at

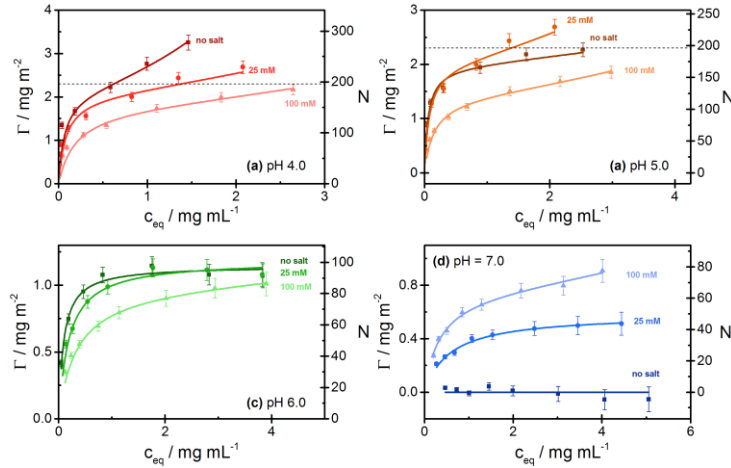


Figure 3.6: Adsorption isotherms of β -lactoglobulin on Ludox TMA at (a) pH 4; (b) pH 5; (c) pH 6; (d) pH 7. Experimental data: filled square, no salt; filled circle, 25 mM NaCl; filled triangle, 100 mM NaCl; full lines: fit by the GAB equation. The estimated monolayer capacity is indicated by a dashed line. See caption to Fig. 3.2 for further details.

pH 4 in the absence of salt, which disappears on addition of salt. In the presence of salt, K_L gradually decreases from pH 3 to pH 6 but appears to increase again at higher pH. The graphs of the adsorption ratio $\Gamma(c^*)/\Gamma_m$ for β -Lg as a function of pH (Fig. 3.7d) again show the singular role of the weak adsorption state of β -Lg at pH 4 in the absence of salt, where a pronounced maximum, $\Gamma(c^*)/\Gamma_m \approx 2$, is observed, implying that 50% of the protein is adsorbed in the weakly bound state. Except for this singular point, $\Gamma(c^*)/\Gamma_m$ values in a range 1.1 to 1.3 are found for the pH range 3 – 5 and values close to 1 at higher pH. This indicates that protein in the weakly bound state plays a significant role in the neighborhood of the isoelectric point, but not elsewhere.

3.4 Discussion

Because Lyz and β -Lg have greatly different values of IEP, electrostatic interactions with the negative silica surface are causing a different dependence of adsorption on pH. A comparison of the adsorption of the two proteins at the SiNP is shown in Figure 3.8, where the surface concentration $\Gamma(c^*)$ of adsorbed protein at a common concentration $c^* = 2$ mg/mL is plotted as a function of pH. For Lyz, where weak adsorption states play no major role, the values of $\Gamma(c^*)$ are similar to those of Γ_m at given pH and ionic strength (see Fig. 3.4d). In the case of β -Lg, for which weak adsorption states are significant in the neighborhood of IEP, values of $\Gamma(c^*)$ are higher than Γ_m at pH values close to IEP (see Fig. 3.7d).

For Lyz in the absence of salt, the surface concentration $\Gamma(c^*)$ increases with pH in a nearly linear manner in the entire experimental pH range up to pH 11.2 \approx IEP.

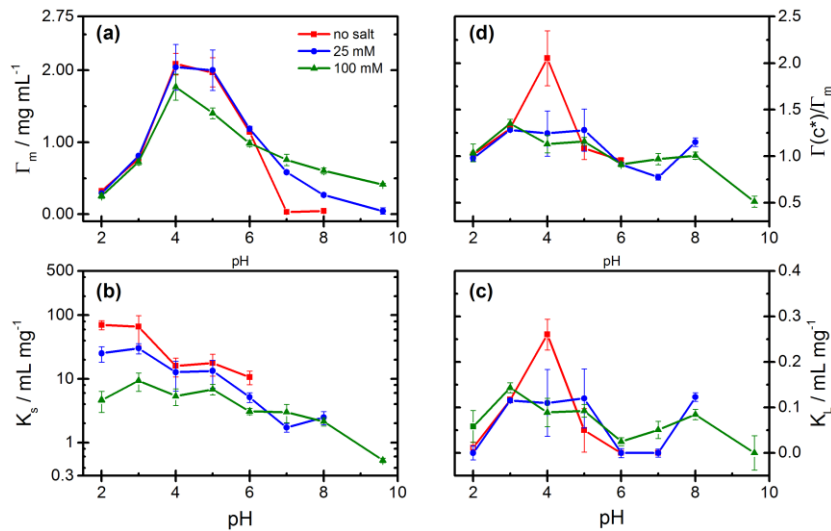


Figure 3.7: β -Lactoglobulin adsorption: Fit values of the GAB parameters as a function of pH for three ionic strengths (no salt, 25 mM, 100 mM NaCl): (a) limiting surface concentration Γ_m of strongly bound protein; (b) adsorption constant K_S ; (c) adsorption constant K_L ; d adsorption ratio $\Gamma(c^*)/\Gamma_m$ for $c^* = 2$ mg/mL (see text).

At $\text{pH} < 7$, the surface concentration is less than a complete monolayer. In this regime, added salt reduces the initial high-affinity adsorption but promotes further adsorption at higher protein concentrations (Fig. 3.3a). The salt-induced reduction of high-affinity adsorption can be attributed to a screening of the attractive electrostatic interaction between protein and the surface (lowering of the binding constant K_S), and the salt-induced promotion of adsorption at higher protein concentrations can be attributed to a screening of the repulsive electrostatic interactions between protein molecules in the adsorbed layer. The interplay of these two effects causes the observed change in isotherm shape (Fig. 3.3a) and a weak increase in $\Gamma(c^*)$ with salt concentration in the region below pH 7, as shown in Figure 3.8.

At $\text{pH} > 8$ the adsorbed amount of Lyz exceeds the amount corresponding to a densely packed monolayer. In this pH regime, added salt causes a weaker increase of $\Gamma(c^*)$ with pH than in the absence of salt, and a maximum in $\Gamma(c^*)$ appears at a pH near IEP. With increasing salt concentration, this maximum becomes more shallow, but we are unable to decide whether it is located at or somewhat below IEP, due to the limited precision of our data and the lack of data for $\text{pH} > \text{IEP}$. Our results do not confirm the existence of a sharp adsorption maximum at a $\text{pH} < \text{IEP}$ reported for the adsorption of Lyz on a flat silica surface in the absence of salt,⁹⁷ but except for this point, our results are consistent with those reported in the literature.⁹⁷ In particular, we also find that added salt causes a decrease in the adsorbed amount in a range of $\text{pH} < \text{IEP}$, in which the adsorbed amount exceeds one monolayer of protein molecules. This finding is surprising at first sight in view of the notion that higher ionic strength reduces the repulsive protein – protein interaction and thus enhances adsorption. Presumably, the formation of a second adsorbed protein layer in the pH region near IEP involves attractive electrostatic interactions between oppositely charged patches on protein molecules in the first and second

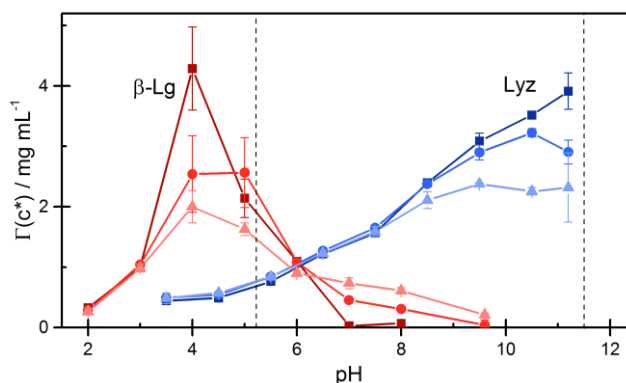


Figure 3.8: Comparison of lysozyme and β -lactoglobulin adsorption onto silica nanoparticles: Adsorbed amount $\Gamma(c^*)$ at the reference concentration $c^* = 2$ mg/mL plotted against pH: filled square, no salt; filled circle, 25 mM NaCl; filled triangle, 100 mM NaCl. The isoelectric points (IEP) of the proteins are indicated by vertical dashed lines.

layer. An increase of ionic strength will screen these interactions and thus cause a reduction of the adsorbed amount, as it is observed for Lyz in this study. Indeed, at 100 mM NaCl, the maximum adsorption of Lyz near IEP has been reduced to hardly more than one nominal monolayer (Fig. 3.8).

In our earlier work,^{31,32} we found that pH and added salt has a pronounced influence on the protein-induced aggregation of SiNP near the isoelectric point. In the absence of salt, large-scale aggregation occurs over a wide pH range, but the aggregates re-disperse at pH 10. Hence, at $\text{pH} \geq 10$, in the absence of salt, the observed adsorbed amount represents the adsorption onto isolated (non-aggregated) SiNP. On the other hand, in the presence of 100 mM NaCl salt, the silica-protein hetero-aggregates do not redisperse near IEP,^{31,32} and thus, the measured adsorbed amount represents the amount adsorbed in the confined geometry between silica particles. Presumably, part of the observed salt-induced decrease in the adsorbed amount near pH 11 is caused by this transition from adsorption onto free particles to adsorption between silica particles in the large-scale aggregates.

For β -Lg, we could characterize the adsorption behavior for pH values on both sides of the isoelectric point (Fig. 3.8). In the pH regime below IEP, the dependence of $\Gamma(c^*)$ on pH and salt concentration qualitatively resembles the behavior of Lyz, although the variation of $\Gamma(c^*)$ with pH is occurring in a narrow pH region due to the low value of IEP. Since the SiNP used in this study are negatively charged down to pH 2 (cf. Fig. 3.1a and Table 3.1), the similar pH and salt dependence of $\Gamma(c^*)$ of the two proteins at $\text{pH} < \text{IEP}$ indicates that in both cases, the behavior is dominated by electrostatic interactions. The low level of adsorption up to pH 3 indicates that in this regime, the attractive protein – surface interactions are nearly balanced by repulsive protein – protein interactions. Both of these interactions are screened by added salt, so that the adsorption level is only weakly affected by salt. The very strong increase in adsorption from pH 3 to pH 4 in the absence of salt, to values much beyond one nominal monolayer, may again be attributed to a transition from repulsive to attractive protein – protein

interactions in the pH range near IEP. This interpretation is supported by the salt-induced reduction of adsorption at this pH. Interestingly, the adsorbed amount at pH 5 (closest to IEP) is much lower than this maximum value and less dependent on the ionic strength. In an earlier study of β -Lg adsorption onto silica surfaces, Elofsson et al.¹⁰³ reported that the pH dependence of adsorption was caused mainly by the pH dependent variation in self-association of the protein in solution. At room temperature and pH values below 4 and above 5.2, the protein exists predominantly in form of dimers and monomers, with an increasing tendency for the dimer to dissociate into monomers at lower and higher pH, respectively. The dissociation of the dimer is the strongest in the absence of salt, due to a higher (less screened) electrostatic repulsion between the monomeric units.¹⁰⁴ In a narrow pH region near pH 4.6, the dimers aggregate to a larger oligomeric unit (presumably an octamer), and this secondary aggregation is enhanced by a decrease in ionic strength.^{103,104} It is tempting to attribute the very high adsorption of β -Lg at pH 4 in the absence of salt, and its strong dependence on the ionic strength at this pH, to the adsorption of this higher oligomer. However, in this case, one would expect a high value of $\Gamma(c^*)$ not only at pH 4 but also at pH 5 in the absence of salt, which is not the case. In this context, we also have to consider that according to a recent report,⁸³ the monomer – dimer association equilibrium of β -Lg in the adsorbed state is affected by curvature of the adsorbing surface. In a study of β -Lg adsorption at a nanoscale hydrophobic surface, it was found⁸³ that the association is weakened by surface curvature, to the extent that no adsorbed dimers were detectable on particles of 25 nm diameter. It would be of interest to find out if such a curvature dependence of protein association also prevails in the adsorption onto hydrophilic NP.

The adsorption behavior of β -Lg at pH > IEP, where the protein has a negative net charge and is electrostatically repelled by the equally charged surface, confirms that adsorption of globular proteins on the 'wrong side' of the isoelectric point is not limited to polyelectrolyte brushes^{88–91} but can also occur on charged inorganic surfaces.^{94,97} Adsorption of β -Lg at pH > IEP may involve electrostatic interactions with the negative silica surface, either due to the persistence of positive patches at the protein surface, or due to charge regulation effects.^{93,94} Non-electrostatic contributions to the adsorption energy must also play a significant role in the adsorption of this protein on the SiNP. At pH 7 and 8, the repulsive electrostatic protein – surface and protein – protein interaction can over-compensate this attractive non-electrostatic adsorption energy in the absence of salt, so that no adsorption occurs. In the presence of salt, the repulsive electrostatic interactions are screened and the non-electrostatic adsorption energy dominates, causing increasing adsorption with increasing salt concentration. Hence, the observed inversion of the salt dependence of the adsorption at pH > IEP can be attributed to the competition of electrostatic and non-electrostatic contributions to the adsorption energy.

As a final remark, we have to point out that the adsorption of the proteins will be affected by the surface chemistry of the SiNP. This applies particularly to the adsorption behavior at low

pH. As shown in Figure 3.1a, the Ludox TMA particles used in the present work have a negative zeta potential down to pH 2. In contrast, the SiNP of our earlier work,³¹ which were prepared by a different route than Ludox TMA, had a zeta potential near zero below pH 4, and no adsorption of Lyz was found on these particles below pH 4. This difference in adsorption behavior at low pH can again be rationalized by electrostatic interactions as outlined above.

3.5 Conclusion

The present study has highlighted the important role of electrostatic interactions in the adsorption of the globular proteins Lyz and β -Lg onto negatively charged silica nanoparticles. For both proteins, two adsorption regimes as a function of pH were identified for $\text{pH} < \text{IEP}$: At low pH, the competition of attractive protein – surface interactions with the repulsive protein – protein interactions causes adsorption limited to one monolayer of protein molecules. At pH values closer to IEP, repulsive interactions between protein molecules become less important and attractive protein – protein interactions resulting from oppositely charged patches on two proteins become relevant, leading to adsorption well above one monolayer of protein at low ionic strength. In the case of β -Lg ($\text{IEP} \approx 5$), for which the adsorption behavior could be studied on both sides of IEP, a pronounced maximum in adsorption was observed somewhat below IEP in the absence of salt, and an inversion of the salt effect on the adsorption level was found in the pH region around IEP. This inversion is attributed to a competition of electrostatic and non-electrostatic contributions to the adsorption energy. The role of protein association to dimers and higher oligomers appears to dominate the adsorption behavior near IEP, but further work is needed to clarify details of this behavior.

Chapter 4 Evolution of Hetero-Aggregate Structure at Different Protein Loadings²

4.1 Introduction

In preceding work the structural properties of hetero-aggregates formed by silica nanoparticles (SiNP) and adsorbed protein were studied by small angle X-ray scattering (SAXS).^{31,32} Similar to the findings explained in the previous Chapter 3 a strong pH and salinity dependence of these structural parameters was found. The structure of the hetero-aggregates is governed by the pH and salinity via the interaction strength between the Lyz and the SiNP.

SAXS experiments require moderate particle and protein concentrations. For very low concentrations the sensitivity is too weak for reliably experimental scattering data. At very high concentrations of particles and proteins the samples tend to multiple scattering, which makes the evaluation of the resulting data impossible as the general scattering theory is not valid for multiple scattering. In addition, the spatial resolution of the used laboratory scale SAXS apparatuses was limited by the assessable q -range. Due to these experimental limitations these studies left open the question how the particles are aggregating when either a very small number or a very large number of protein molecules are available.

In order to overcome the limitations of SAXS in the extreme protein loading scenarios fluorescence correlation spectroscopy (FCS) and confocal laser scanning microscopy (CLSM) was used. This combination of techniques allowed to study a very broad loading range from 0.1 to 5,000 Lyz per particle, and also offered the opportunity to monitor the aggregates with direct optical methods. The aggregate sizes for low protein loadings were investigated with FCS. The dense and turbid samples obtained for higher concentrations were observed with CLSM and a 3D reconstructions of these micrographs were made. The surface-area-to-volume ratio of the found aggregates was used as a measure for the structural properties.

The FCS and CLSM techniques require that the probed sample is fluorescent. This was achieved by labeling lysozyme with a fluorescein dye. Additionally, the adsorption parameter (Chapter 3) for labeled and native lysozyme were compared, to ensure the general relevance of the results obtained with the labeled protein.

² The experiments presented in this chapter were performed by Albert Prause in his Bachelor thesis which was supervised by Prof. Findenegg and myself. In particular, I was strongly involved in the planning of the experimental program and day-to-day supervision of the experiments, as well as the data evaluation and interpretation.

4.2 Materials and Methods

4.2.1 Materials

Commercial Ludox TMA (Sigma Aldrich) silica particle dispersions (SiNP) were used for the studies presented in this chapter. The particles had an average particle size of 27 nm and a polydispersity of $s = 0.13$ (SAXS). To remove possible impurities and additives the stock solution was dialyzed (using a membrane with a molecular weight cutoff of 14.000 kDa) against water which was changed three times per day. According to the manufacturer data sheet, the specific surface area of the material was $a_s = 128 \text{ m}^2\text{g}^{-1}$. For the experiments Milli-Q water from Millipore QPAC was used ($18 \text{ M}\Omega \text{ cm}$).

Lyophilized hen egg white lysozyme (Lyz, Sigma Aldrich, $MW = 14,388 \text{ Da}$, $\geq 90 \%$), fluorescein-5-isothiocyanat (FITC), Merck and Sigma Aldrich), acetic acid (AcOH, Th. Geyer, $\geq 99.5 \%$), 2-(bis(2-hydroxyethyl)-amino)-acetic acid (BICINE, Sigma-Aldrich, $\geq 99 \%$), 3-(cyclohexyl-amino)-1-propane sulfonic acid (CAPS, Sigma-Aldrich, $\geq 98 \%$) was used without purification.

4.2.2 Protein Labeling

301 mg of lysozyme (Lyz) was dissolved in 6.92 mL BICINE buffer (10mM pH 8.3) and the pH was adjusted to 8.3 again. Under stirring 8.15 mL of a FITC stock solution (1 mg/mL, in BICINE, pH 8.3) was slowly added to the native lysozyme (Lyz_{native}) solution. The mixture was stirred at 20 °C for 15 h. The pH was adjusted to pH = 4 (HCl, 1 M) and the mixture was stirred for additional 30 min. The labeled Lyz (Lyz_{FITC}) was purified by size exclusion chromatography (PD-10 column, GE Health Care, Matrix: Sephadex G-25) using the gravity protocol. The collected orange solution was lyophilized and the solid orange product (Lyz_{FITC}) was stored at -30 °C.^{109,110}

4.2.3 Adsorptions Measurements

Adsorption experiments were performed as described in Chapter 3. In a typical experiment, samples of 2 mL were prepared by mixing aliquots of stock solutions of SiNP dispersion, Lyz_{FITC} and NaCl to achieve the desired compositions. The SiNP with the adsorbed protein were sedimented by centrifugation (21,000g) and the supernatant was collected. The concentrations of protein and dye in the supernatant were determined by UV-vis spectroscopy

of the protein backbone (280 nm) and the dye (491 nm). The adsorbed amount was calculated according to the method described in Chapter 3.

4.2.4 Fluorescence Correlation Spectroscopy

A Leica TCS SP5 II confocal microscope equipped with a HCX PL APO CS 63.0×1.20 water UV immersion objective and an argon-laser (488 nm) was used for the FCS and CLSM experiments. The samples were prepared on cover slides (Zeiss, 18 mm x 18 mm, thickness: $170 \pm 5 \mu\text{m}$). The pinhole aperture was set to $111.48 \mu\text{m}$. The confocal volume (0.23 fL) and its aspect ratio ($\xi = 6$) was measured after every restart of the instrument with an aqueous Rhodamine 6G solution (5 nM). A fresh reference sample of LyZ_{FTC} and FITC solution was measured for new day of instrument use.

For FCS experiments 3 sets of TMA dispersions (0.01, 0.10 and 1.00 wt%, CAPS 10 mM, pH 9.6) were prepared. To those dispersions aliquots of LyZ_{FTC} were added to achieve the desired concentrations (1, 5, 10 and $20 \mu\text{g mL}^{-1}$). A sample ($20 \mu\text{L}$) was measured three times for 10 min with a low laser intensity ($< 2 \text{ mW}$ in the confocal volume). The sample was covered during the experiment to avoid evaporation of the solvent or possible parasitic light incidence. The theory is described in more detail in Chapter 2.

4.2.5 Confocal Laser Scanning Microscopy

The same microscope setup was used as for the FCS experiments. For the CLSM experiments 3 sets of TMA dispersions (0.01, 0.10 and 1.00 wt%, CAPS 10 mM, pH 9.6) were prepared and mixed with aliquots of LyZ_{FTC} to achieve the desired concentrations (10, 20, 50, 100, 150, 200, 300, 400 and $500 \mu\text{g mL}^{-1}$) of LyZ_{FTC}. A sample ($20 \mu\text{L}$) was pipetted on a cover slide and allowed to rest for 5 min. Signal gain of the detector was set to 500 V. Every measurement gave a three-dimensional (3D) stack of micrographs with a volume of $246 \times 246 \times 123.4 \mu\text{m}$ with a lateral resolution of $0.48 \mu\text{m/pixel}$ and a height resolution of $0.50 \mu\text{m/pixel}$.

The 3D-stacks were analyzed with the Fiji¹¹¹ software package using the 3D-object counter.¹¹² In a first step the contrast was normalized and the intensity threshold for the object analysis was set to 75. The object analysis gave values for the surface and the volume of all objects in the sample volume. From the sum of all object surfaces $\sum_i A_i$ and the total object volume $\sum_i V_i$ the surface-area-to-volume ratio A/V was calculated according to Equation 4.1 for further interpretation of the data. The theory is described in more detail in Chapter 2.

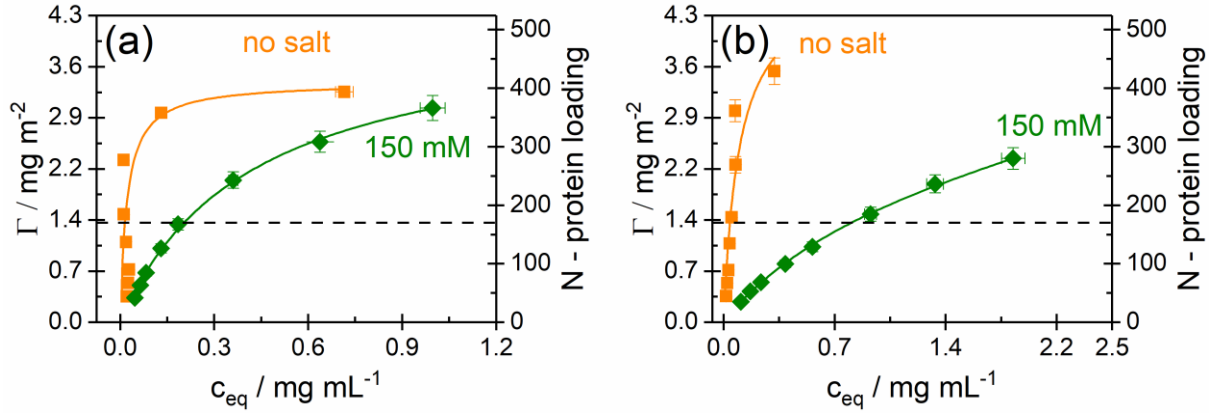


Figure 4.1: Experimental adsorption isotherms for $pH = 9.6$ (a) and $pH = 10.5$ (b). Shown are the data for samples with added salt (green symbols) and without added salt (orange symbols). The solid lines represent the fits using the GAB-adsorption model, the dashed line corresponds to one close-packed layer of protein molecules at the particle surface. This figure is modified from the Bachelor thesis of Albert Prause.

$$A/V = \frac{\sum_i A_i}{\sum_i V_i} \quad (4.1)$$

4.3 Results

4.3.1 Adsorptions Comparison

Adsorption isotherms for FTC-labeled lysozyme (Ly_{FTC}) on TMA particles and fits of the data with the GAB model are shown in Figure 4.1. The isotherms shown are taken at high pH close to the IEP of Ly_{FTC} to match the conditions in the fluorescence experiments. For the case of no added salt (orange data points and solid lines in Fig. 4.1) the adsorbed amount rises steeply and reaches a maximum value already for low equilibrium concentrations of Ly_{FTC} (<0.5 mg/mL). Under these conditions the adsorbed protein amount is well beyond the value for one monolayer of protein which is indicated by the black dashed line in the diagrams. The limiting adsorbed amount at pH 10.5 without added salt was beyond the experimental concentration range.

The addition of salt changes the steepness of the isotherms drastically (green data points and solid lines in Fig. 4.1). The limiting adsorbed amount is reached at higher equilibrium concentrations >1 mg/mL) in the case of pH 9.6.

The adsorption isotherms were analyzed by a fit to the GAB adsorption model (Eq. 3.3) for adsorption from liquid phases (cf. Chap. 3). The resulting best fit values for the model parameters are displayed as a function of the bulk pH in Figure 4.2. Panel 4.2a shows the limiting adsorption Γ_m which is increasing with increasing pH. When no salt is added to the

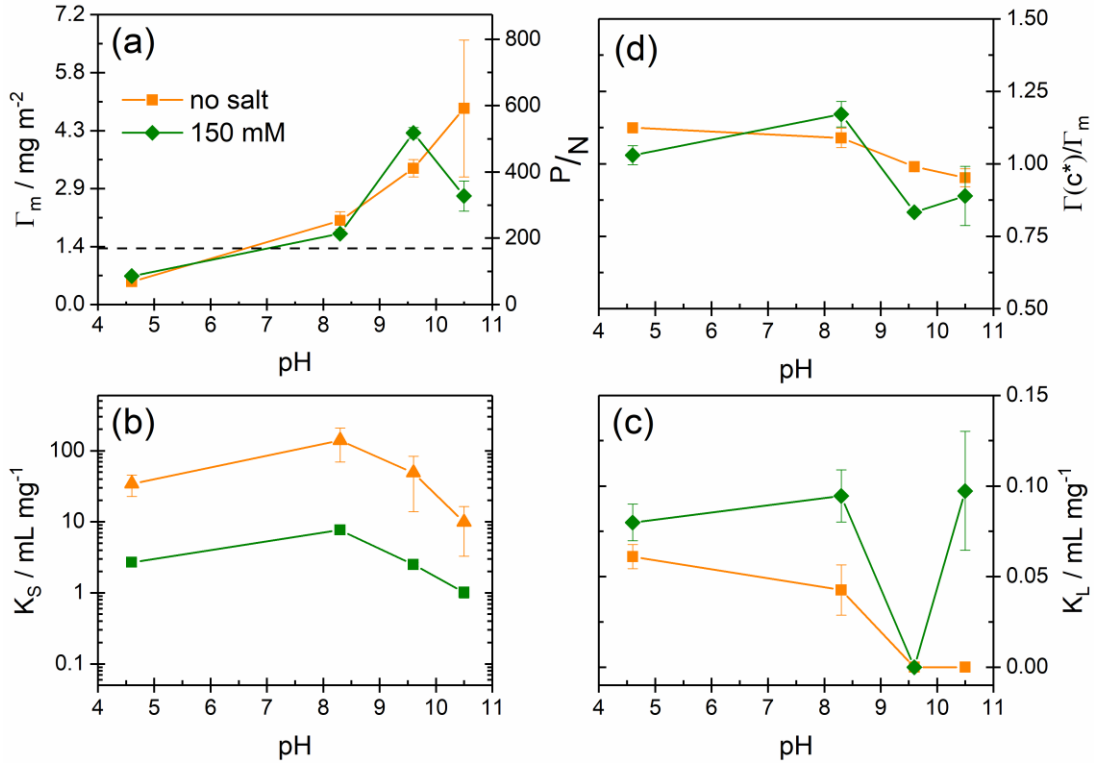


Figure 4.2: Best fit values of the GAB-model parameters for Lyz_{FTC}/SiNP as a function of the bulk pH. The limiting adsorption (a), adsorption constants K_S (b) and K_L (c) and the adsorption ratio $\Gamma(c^*)/\Gamma_m$ for $c^* = 2 \text{ mg/mL}$ (d) are shown.

system this behavior continues for the experimental pH range. However, the value of the maximum adsorbed amount for this sample shows a large error which can be rationalized by the experimental concentration range. The other GAB-model parameters show no significant change within the experimental pH range. The adsorption constant K_S peaks around pH 8 and drops for higher pH values. Constant K_L is for the entire pH low and decreases with higher pH. All best fit values for the parameters of the GAB-adsorption model are summarized in Table 4.1.

Table 4.1: Comparison of the GAB model parameters for the adsorption of FTC-labeled and native lysozyme (Lyz_{FTC} and Lyz_{native}) on Ludox TMA nanoparticles presented in Figure 4.2.

pH	Lyz _{FTC}				Lyz _{native}			
	4.6	8.3	9.6	10.5	4.5	8.5	9.5	10.5
$\Gamma_m / \text{mg m}^{-2}$	0.6	2.1	3.4	4.0	0.5	2.4	3.1	3.5
$K_S / \text{mL mg}^{-1}$	34	140	49	10	134	46	62	72
$K_L / \text{mL mg}^{-1}$	0.06	0.04	0	0	0	0	0	0

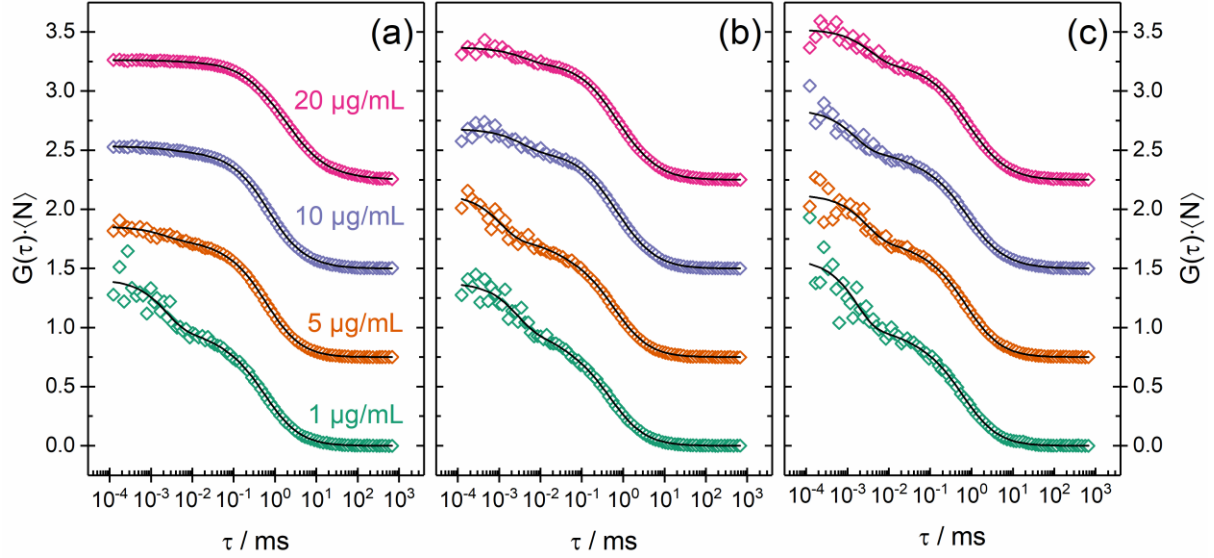


Figure 4.3: Normalized experimental correlation functions from the investigated Lyz/SiNP samples. The panels correspond to SiNP concentrations of (a) 0.01 wt%, (b) 0.1 wt%, (c) 1 wt%. The correlation functions in the individual panels represent different concentrations, as indicated in panel (a); the same concentrations are shown in the panels (b) and (c). For clarity the correlation functions are shifted relative to each other by a constant increment of 0.75. This figure is modified from the Bachelor thesis of Albert Prause.

4.3.2 Fluorescence Correlation Spectroscopy

All correlation functions gathered for the three sets of samples are displayed in Figure 4.3. Every experimental correlation function was normalized to the total number of fluorophores $\langle N \rangle$ in the sample. Experimental correlation functions were fitted with Equation 2.7 (cf. Chapter 2). The mean number of fluorophores in the confocal volume was calculated with Equation 2.6.

The analysis was done with 2 or 3 components for every correlation function. A small amount of free fluorescein dye (FTC) was found in most samples. Its characteristic time constant was determined in a separate experiment and kept constant during the fitting process. Using Equation 2.8 the fitted characteristic diffusion times were converted into the diffusion constants D_f . The corresponding hydrodynamic radius (R_h) of each component was calculated via the Stokes-Einstein equation (Eq. 4.2).

$$R_h = \frac{k_B T}{6\eta\pi D_f} \quad (4.2)$$

The resulting values for the diameter of the diffusing species and the corresponding number fractions of fluorescent particles are plotted in Figure 4.4 against the number of proteins per nanoparticle in the sample (Lyz/SiNP). Over the entire experimental range small clusters with a $D = 2R_h = 33 \pm 5$ nm are found. This size is close to the diameter of the primary TMA

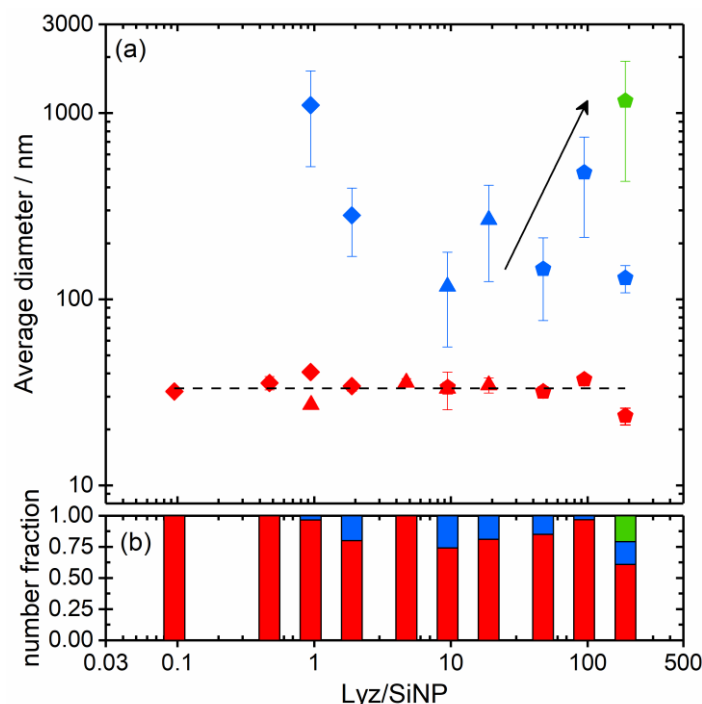


Figure 4.4: (a) Average diameters of diffusing species in Lyz/SiNP samples as calculated from the characteristic diffusing times (see text) obtained by FCS. The parameters are plotted versus Lyz/SiNP. (b) Number fraction of the different diffusing species in the samples. The colors of the bars indicate the size of the species corresponding to the colors given panel (a). This figure is partially reproduced from the Bachelor thesis of Albert Prause.

SiNP($D_s = 27$ nm). Starting at a loading of 1 Lyz/SiNP, a second fraction of particles with a larger but varying diameter D become detectable. At a protein loading of 1 Lyz/SiNP these larger aggregates have a diameter of $D \approx 1$ μm , but the size of these larger aggregates decreases as the protein loading is further increased. At a loading of 10-20 Lyz/SiNP D is found to be close to 100 nm. For even higher loadings the diameter increases again to D close to 1 μm . For the sample with the highest protein loading (Lyz/SiNP = 200) a third component appeared in the FCS data. This indicates that the population of larger aggregates is polydispers.

Over the entire range of Lyz/SiNP the number fraction of small particles in the confocal volume is high (Fig. 4.4b). Here it is important to note that one large aggregate, consisting of many bridged SiNP is detected as one diffusing entity. Therefore, number fraction is dominated by the small clusters.

4.3.3 Confocal Laser Scanning Microscopy

The long-range structure of the large aggregates was studied with CLSM, as this technique provides information in the micrometer length scale. The set of the reconstructed 3D images is

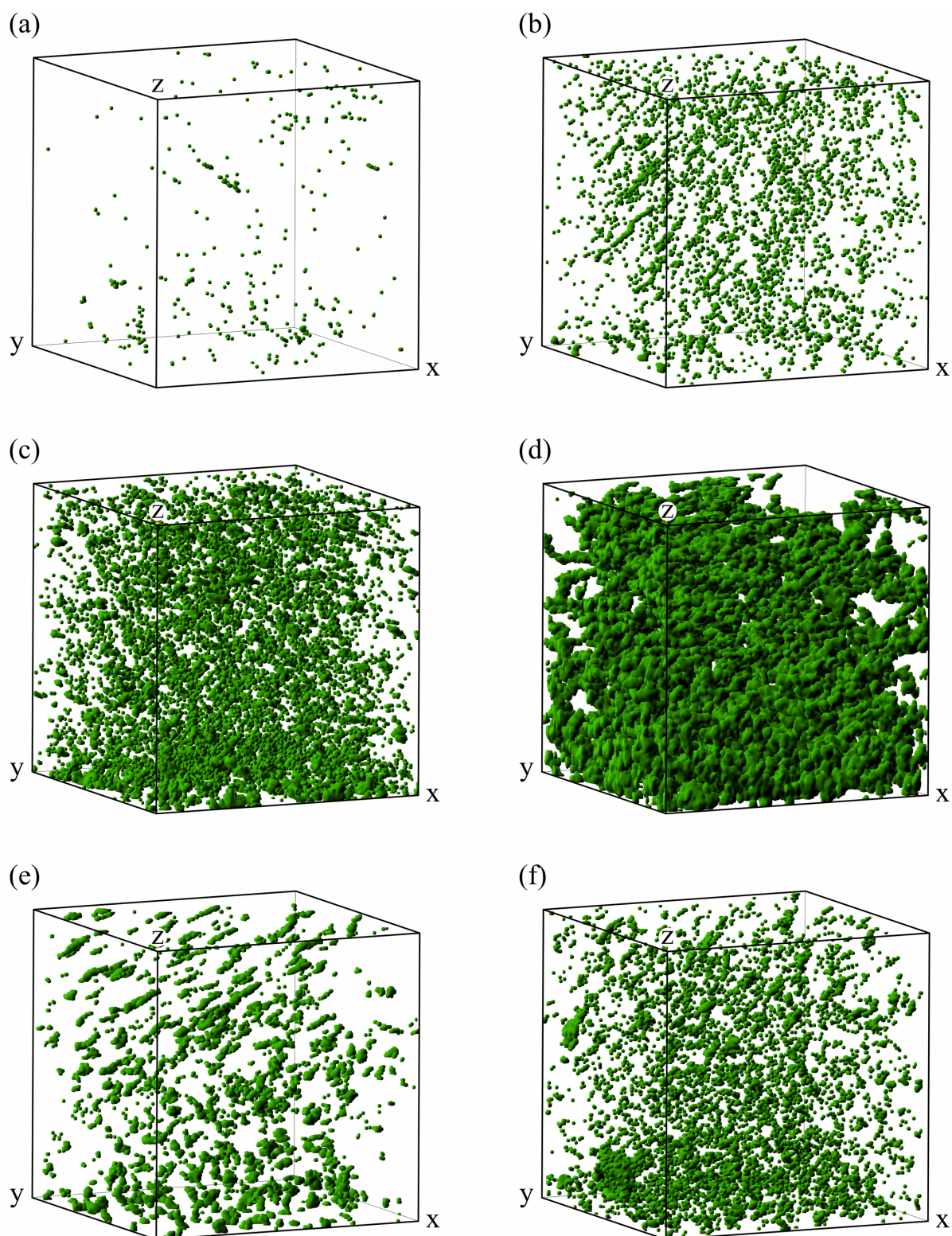


Figure 4.5: 3D reconstructions of 2D CLSM micrographs of the samples of SiNP with Lyz. The visible structures are formed by hetero-aggregation of individual SiNP (depiction in false color). Every panel shows one 3D stack for one specific loading ratio (Lyz/SiNP) after normalization and image processing. (a) $\text{Lyz/SiNP} = 9.4$, (b) $\text{Lyz/SiNP} = 28.3$, (c) $\text{Lyz/SiNP} = 142$, (d) $\text{Lyz/SiNP} = 377$, (e) $\text{Lyz/SiNP} = 953$, (f) $\text{Lyz/SiNP} = 4715$. Every 3D stack has a box size of $123 \times 123 \times 123 \mu\text{m}^3$. This figure is reproduced from the Bachelor thesis of Albert Prause.

displayed in Figure 4.5 where the panels (a) and (b) correspond to 0.01 wt% of SiNP, (c) and (d) to 0.1 wt% of SiNP and (e) and (f) to 1 wt% of SiNP. The Lyz_{FTC} concentration was adjusted accordingly to achieve a wide range of protein loadings from 9.4 Lyz/SiNP in panel (a) going up to nominal 4715 Lyz/SiNP in panel (f).

At low loadings (Fig. 4.5a) only very few and small aggregates are visible. The number of these small aggregates increases when the amount of added protein is increased (Fig. 4.5b). When the loading is further increased the aggregates grow in size and number. Near the bottom of the observed sample volume larger aggregates are found due to sedimentation. Figure 4.5d shows a dense network, filling the entire observation volume. This space-filling network breaks up into smaller elongated aggregates for even higher loadings (Fig. 4.5e) and finally (Fig. 4.5f) relatively small and compact aggregated at very high loadings.

The surface-area-to-volume ratio A/V was extracted from the data by the method described in Section 4.2.4 and the results are displayed as a function of the nominal protein loading in Figure 4.6. For low protein loadings up to 20 Lyz/SiNP , A/V is found to be constant within the error margin ($A/V \approx 10 \pm 0.5 \mu\text{m}^{-1}$). As the protein loading increases A/V drops slowly to $A/V \approx 8 \pm 0.7 \mu\text{m}^{-1}$. Exceeding the nominal monolayer capacity of 170 Lyz/SiNP , A/V drops sharply to approximately $3 \mu\text{m}^{-1}$. This drop is followed by a gradual increase of A/V for higher protein loadings until reaching $A/V = 6.5 \pm 1.2 \mu\text{m}^{-1}$ at the end of the experimental protein loading range of 4715 Lyz/SiNP .

4.4 Discussion and Outlook

4.4.1 Adsorptions Comparison

The results of the adsorption measurements for Lyz_{FTC} on Ludox TMA are compared with results for native Lyz in Table 4.1. The limiting adsorption Γ_{m} of Lyz_{FTC} is systematically higher than for $\text{Lyz}_{\text{native}}$ and most significant for high pH values (beyond the IEP of Lyz). For lower pH values the differences are within the error margin of the measurement. Nevertheless, this can indicate a minor difference in the adsorption behavior of Lyz_{FTC} and $\text{Lyz}_{\text{native}}$. One possible explanation for this observation can be found in the manipulated chemical composition of Lyz_{FTC} . The hydrophobic dye could cause the formation of a fraction of dimers adsorbing to the SiNP and thus increasing the Γ_{m} . At low pH conditions Lyz carries a high positive charge. Hence, the formation of dimers is prohibited by charge stabilization. At pH values close to the IEP the net charge of Lyz might not be sufficient to stabilize the modified Lyz_{FTC} .

The interaction strength of the first strongly adsorbed layer of protein is characterized by K_{S} (cf. Chap. 3). The values of K_{S} for Lyz_{FTC} are comparable within the error margin to the

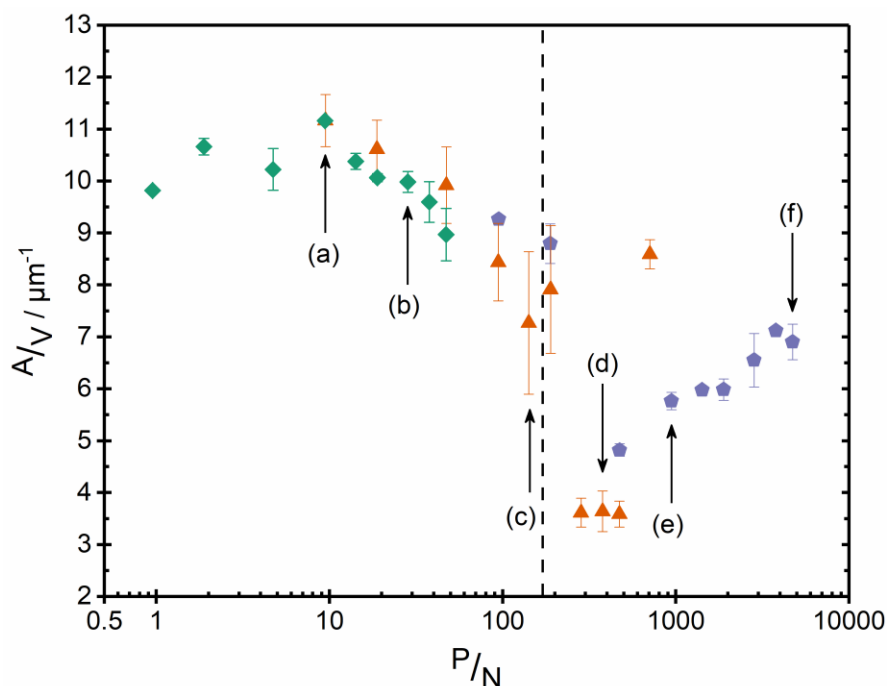


Figure 4.6: Nominal surface to volume ratio of Lyz/SiNP aggregates for different loading ratios. The concentration of SiNP in the samples is indicated by the color and the symbol shape. Red diamonds: 1 %; blue triangles: 0.1 %, green circles: 0.01 %. Surface and volume of the aggregates are analyzed from CLSM scans by the software Fiji.⁶² The marked data points correspond to the respective 3D graphic in Figure 4.5. This figure is modified from the Bachelor thesis of Albert Prause.

values of K_S for $\text{Lyz}_{\text{native}}$. Therefore, it is valid to assume the adsorption strength of native and modified Lyz towards the silica surface to be similar. The third GAB-model parameter, K_L , is a measure for any further than one adsorbed layer. In both cases, Lyz_{FITC} and $\text{Lyz}_{\text{native}}$, K_L is nearly zero. This implies a monolayer adsorption. However, the adsorption of dimers, formed by bridging between the FTC groups would not show up in this measure, as the dimer adsorbs as one single particle.

Summarizing the adsorption quantification we see a very similar behavior for Lyz_{FITC} and $\text{Lyz}_{\text{native}}$ on Ludox TMA SiNP. Significant differences are measurable at pH values higher than the IEP of the protein. Regarding the FCS/CLSM experiments, which were conducted at lower pH (pH=9.6) no major differences in adsorption behavior due to the functionalization with FTC are expected.

4.4.2 Fluorescence Methods

The aggregation behavior on short length scales was investigated by FCS and the results are summarized in Figure 4.4. The correlation curves obtained by FCS experiments were fitted assuming two or three diffusing species inside the confocal volume (additionally to free FTC). One of the species, which was found in all samples, had a hydrodynamic diameter of 33 nm

(Fig. 4.4, red points). This diameter conforms roughly to the diameter of one SiNP with two adsorbed Lyz. This supports earlier findings of individual particles with adsorbed protein close to pH 10.³¹ These clusters are charge stabilized by the negative charge of the central SiNP not compensated by the adsorbed Lyz.

A second population of larger objects is detectable in the FCS data from Lyz/SiNP samples (Fig. 4.4, blue points). Judging on this, already one Lyz per SiNP is enough to form larger networks of connected particles. The error bars for these aggregates are large which is not surprising, as these large aggregates are not spherical and not monodisperse, as CLSM micrographs show (Fig. 4.5). Of course, such an irregular population of objects is expected to produce a broad distribution in the diffusion times leading to a large uncertainty in the calculated sizes. FCS is not suited for the analysis of irregular aggregates, further information is obtained with CLSM.

Comparing the number ratios of the small and large species in the confocal volume (Fig. 4.4) it seems that the small particles are the majority. But this is a mathematical artifact, as one large aggregate, consisting of thousands of SiNP, is counted as one single diffusing particle. A more useful value is the mass fraction but a conversion is not possible as the exact volume of the large aggregates is not precisely known.

For a better understand the structure and its evolution with increasing protein loading a 3D images were reconstructed from stacks of 2D CLSM micrographs. In order to investigate a broad range of protein loadings the samples were prepared with different initial particle concentrations. Therefore, the overall amount of aggregates is different between some of the samples. For a comparable analysis of the 3D structures the surface-area-to-volume ratio A/V was calculated using Equation 4.1. The results of this analysis are displayed in figure 4.6 as a function of the nominal protein loading Lyz/SiNP. A plot of A/V versus a mutual Lyz/SiNP axis shows a general trend and merges together without further normalization. This is an indication for the applicability of this analysis. A low A/V for a given volume of aggregates is expected for spherical and large structures. When the aggregates are small or show an irregular network structure A/V increases.

The effect of sedimentation was evaluated by analyzing the A/V for the upper and lower half of one sample (377 Lyz/SiNP, Fig. 4.5d). The calculation resulted in $A/V = 4$ for the upper half, compared to $A/V = 3$ for the lower half of the sample. This result is expected, as the larger and most compact aggregates (with a lower A/V) should sediment faster than the smaller branched ones. Nevertheless, the found differences are nearly within the error margin of the used method. Therefore, the effect of sedimentation is not further discussed in this study.

Final results of A/V analysis are displayed in Figure 4.6, following the evolution of the aggregate structure as a function Lyz loading. At low Lyz loadings (Lyz/SiNP < 10) the A/V remains constant on a high value. The aggregates found in this regime are compact in shape. Beginning with Lyz/SiNP = 10 the A/V drops, first slightly then sharply, until a minimum at

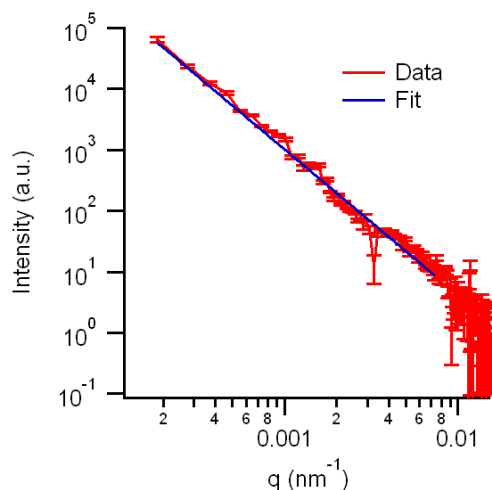


Figure 4.7: Static light scattering (SLS) profile $I(q)$ for Lyz/SiNP (1 wt% Ludox TMA, 3 mg/mL Lyz_{native}). Courtesy of Dr. Heinz Amenitsch (TU Graz). The experiment was performed with a flat cell SLS apparatus capable of measuring turbid samples.⁶⁴ The blue line represents a Porod fit resulting in a power law of 2.38 indicating a fractal dimension of 2.38.

protein loadings around the monolayer capacity of Lyz/SiNP = 170. This implies that the aggregates become denser and more compact. It is interesting, that the start of the drop in Figure 4.6 coincides with the appearance of larger objects in the FCS results (Fig. 4.4). The SiNP repel each other because the negative charges on the particles are not fully compensated by the adsorbed Lyz. This results in a sponge-like network structure. At loadings beyond the monolayer capacity A/V increases again until the end of the experimental Lyz/SiNP range, the network structure breaks up into smaller and more compact parts. The excess of Lyz in the system lead to charge compensation of the SiNP, even though the single Lyz are only weakly charged at this pH. The network structure contracts and reduces its external surface.

These results are comparable with earlier findings for pH titrations by Bharti et al. This is unsurprising as both effects (pH and Lyz concentration) relay on the same influence factors: Residual charge on the SiNP. During a pH titration the net charge of the aggregates is regulated by the protonation state of SiNP. In the current experiment a similar effect is achieved by regulating the charge on the SiNP by the amount of Lyz in the system. This reproducibility strengthens the assumption that the adsorption of Lyz is dominated by electrostatic forces and proves that A/V is a useful parameter for the analysis of CLSM data.

For future work the analysis of the 3D CLSM data should be extended to the fractal dimension. This would enhance the comparability and wide spread use of this method even further.¹¹³ The software package used for this analysis includes a method for calculating the 2D fractal dimension, which can be transferred to 3D fractal dimensions via $D_{\text{frac, 3D}} = D_{\text{frac, 2D}} + 1$.^{114–116} Strictly this approach is limited to particle sizes larger than the experimental resolution. It would be necessary to compare the results from this method with an independent experiment, like static light scattering (SLS). Hence, fractal dimensions can be derived from a Porod fit. However, turbid samples, like Lyz/SiNP, are notoriously difficult to measure with SLS

techniques because their tendency for multiple scattering. The effect of multiple scattering can be minimized by maintaining a high transmission ($T > 0.9$) with a small sample cell thickness. To test the feasibility of this approach one sample was send to Dr. Heinz Amenitsch at the TU Graz (Fig. 4.7). The custom SLS apparatus at the TU Graz is equipped with a special flat geometry sample cell with variable thickness. Making it possible to maintain a high transmission and reduce the influence of multiple scattering. The data was fitted with a Porod fit resulting in a fractal dimension of $D_{\text{frac}} = 2.38$. This example shows that SLS is a potential addition to the presented experiments and can contribute to the structure evaluation of Lyz/SiNP composites.

Chapter 5 Orientation of Cytochrome *c* Adsorbed on Silica Particles³

5.1 Introduction

In the past decade nanoscience has found its way into numerous biomedical applications, such as targeted molecular delivery, in-vivo imaging, sensing, and gene therapy.^{117–119} In all these application the nanosized particles come in direct contact with the biomolecular environments containing various proteins. The efficiency and biocompatibility of the functional nanomaterials is strongly influenced by their interaction and binding with surrounding proteins.^{120,121} Hence, developing a fundamental understanding on how proteins interact with nanoparticles is of eminent importance. The binding of proteins onto nanoparticles is a net result of convoluted surface and bulk effects, such as electrostatics, van der Waals, hydrophobic, and steric interactions.^{120,122,123} The contribution of each force in the surface self-assembly of protein is governed by physiochemical characteristics of the protein, particle, and surrounding medium.¹²⁴ Several recent studies have been focused on developing a better understanding of these bio-nano interactions. While most of the reports investigate the change in the secondary structure of proteins upon adsorption,^{125,126} less attention was paid to the determination of their spatial orientation on the surface.

Proteins are biopolymers with a highly complex composition and anisotropic shape. The anisotropic nature of proteins leads to the possibility to bind a substrate in numerous configurations. However, only a few orientations are thermodynamically favorable.^{30,42} For example, cytochrome *c* forms a macroscopically ordered film when a non-covalent high-affinity binding occurs between the protein and the substrate. Whereas the film is disordered when the substrate has sites with variable binding energies.¹²⁷ These binding characteristics not only influence the assembly of the protein on surfaces, but also impact its biochemical properties, including enzymatic activity.^{40,128,129}

The spatial organization of the proteins can be investigated using methods such as, labelling proteins with probes to determine local surface binding sites,⁴² and via measuring protein redox potentials. The labelling of proteins with fluorescent probes significantly alter the binding energy of the specific site,¹³⁰ and not all proteins show redox behavior limiting the practical applicability. Accordingly, complementary methods for determining protein orientation at surfaces are highly desirable.

³ The work presented in Chapter 5 is a draft of a manuscript which is in preparation and will be submitted for publication in the near future. J. Meissner, J. Justin, Z. Di, G. H. Findenegg, B. Bharti, *in preparation*.

5.2 Materials and Experimental Techniques

In this chapter small angle neutron scattering (SANS) was used to investigate the effect of surface charge distribution on the orientation of cytochrome *c* onto silica nanoparticles. The primary structure of cytochrome *c* consists of 104 amino acids, two of which are connected to a heme *c* group via thioether bonds. The outer shape of the folded cytochrome *c* protein can be approximated as an ellipsoid of dimensions $2.6 \times 3.0 \times 3.2 \text{ nm}^3$.¹³¹ Silica dispersions were used as model nanoparticles to study the binding of the protein. The particles were synthesized using previously reported methods,^{132,133} and their diameter was fine-tuned by adjusting the reaction temperature and stirring speed. The physical characteristics of the nanoparticle dispersion synthesized are provided in Table 5.1 (corresponding SANS profiles in Fig. 5.6).

The shape and size of the protein in D_2O without any silica nanoparticles was determined using SANS. The experimental SANS profiles were measured in the pH range 2 – 11, and were fitted using the form factor of randomly oriented oblate ellipsoids.¹³⁴ The SANS intensity curves and the resulting fit values of equatorial (D_p^{eq}) and axial (D_p^{ax}) diameters are displayed in the Appendix (Fig. 5.7). We find that the diameter of cytochrome *c* remained constant within the experimental error margin over the studied pH range, with $D_p^{\text{eq}} \sim 3.7 \text{ nm}$ and $D_p^{\text{ax}} \sim 2.1 \text{ nm}$. The observed protein size and its independence on the solution pH is in agreement with previous reports.^{135,136} Structural changes between the two redox states of cytochrome *c* are small.^{135,137}

The focus of the present study is the determination of the spatial orientation of cytochrome *c* on silica nanoparticles. To access information about the orientation of the protein it is necessary to measure scattering originating from the cytochrome *c* adsorbed onto silica nanoparticles. From neutron scattering profiles a lot information about the surface-bound protein can be obtained, as the contrast of proteins and particles to deuterated water (D_2O) is high (i.e. its neutron scattering length densities are very different). In order to suppress incoherent scattering from hydrogen to a minimum the nanoparticles dispersions were synthesized directly in D_2O . The experiments were performed on 1 wt% (3.2 wt% for SiNP41) silica particle dispersions containing a fixed amount of cytochrome *c*. The amount of

Table 5.1: The particle size, its polydispersity and the experimental volume fraction determined by fitting experimental SANS profiles of the silica particle dispersions. The curve fitting was performed using the form-factor of spheres, randomly distributed in D_2O , with a log-normal size distribution. The respective SANS intensity curves $I(q)$ are displayed in Figure 5.6.

Sample	Diameter D_{SiNP} /nm	Polydispersity	Volume fraction
SiNP7	7	0.17	0.0051
SiNP13	13	0.14	0.0051
SiNP41	41	0.13	0.0164

cytochrome *c* was chosen in such a way that at pH 8.3 basically all protein was adsorbed on the particles, and no free protein remained in solution. The pH of the dispersion was varied in the range 2-11, by the addition of minimum amount of 0.1N HCl or 0.1N NaOH. The resulting SANS profiles were then analyzed using SasView software package.¹³⁸

5.3 The ‘Raspberry-like’ Form Factor

A SANS profile of a dispersion is obtained by radially averaging the corresponding 2D scattering pattern. The scattered intensity, $I(q)$, is related to the shape, size, concentration, composition and spatial distribution of the scattering objects as¹³⁹

$$I(q) = N\Delta\rho^2 P(q)S(q) \quad (5.1)$$

where N is the number of the scattering objects, $\Delta\rho$ scattering length density contrast of the particles against the matrix (here D₂O), and q is the scattering vector related to neutron wavelength (λ) and angle of scattering (θ) as $q = 4\pi/\lambda \sin \theta/2$. In Equation 5.1, $P(q)$ and $S(q)$, respectively, are form factor and structure factor. The form factor, $P(q)$, is a function of particle shape, and size; and $S(q)$ is the measure of spatial correlation between these particles. For particle dispersions, the characteristic interparticle separation (center-to-center distance) are always larger than the single particle diameter, hence the $S(q)$ selectively affects the $I(q)$ at low scattering vectors. Whereas the $P(q)$ selectively influences the scattering intensity at higher scattering vectors. In this article, we focus on the model dependent analysis of the form factor $P(q)$, and ignore contributions from structure factor i.e. $S(q) = 1$, which have been addressed in previous reports.^{32,140}

A typical SANS profile obtained for a silica dispersion with $D_S = 7$ nm, containing 4.68 mg/mL of cytochrome *c* at pH 8.3 is shown in Figure 5.1a. The smeared oscillation observed at $q \sim 1$ nm⁻¹ is the signature of form factor of silica nanoparticles with adsorbed protein. The oscillation at $q \sim 0.2$ nm⁻¹ is the result of structure factor originating from high concentration of repulsive silica particles in the dispersion. Since we are interested in determining the orientation of cytochrome *c* on silica nanospheres, we specifically focus on the range $0.2 < q < 3$ nm⁻¹.

Accessing a detailed picture of nanoscaled structures by the application of scattering techniques relies on an appropriate form factor model which represents the geometrical conditions of the sample. In Figure 5.1 three different form factor models representing three possible scenarios for the assembly of cytochrome *c* and silica nanoparticles are compared with an experimental scattering profile. These are: (a) A mixture of non-interacting spheres and ellipsoids; (b) particles with a uniform shell of discrete thickness, and (c) particles decorated with individual spherical objects (‘raspberry-like’ particles).

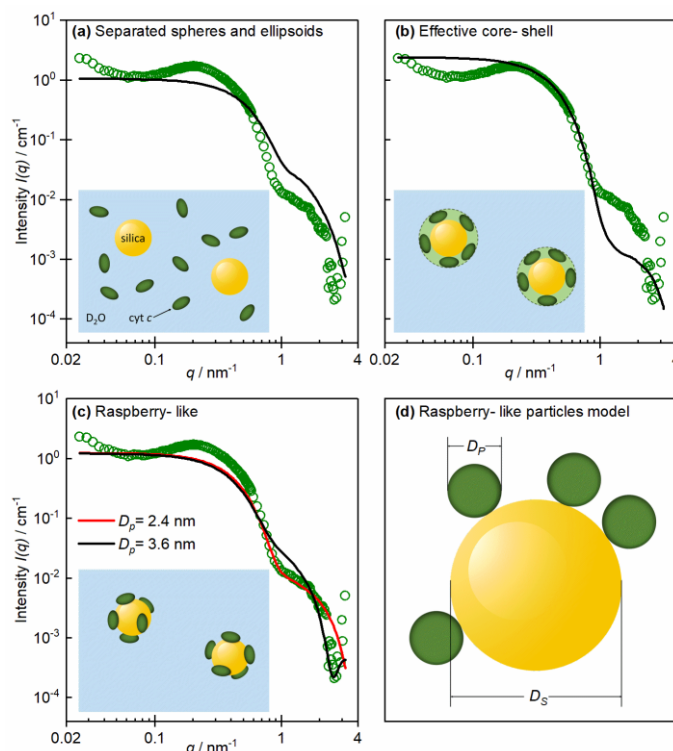


Figure 5.1: (a), (b) and (c): Neutron scattering profiles $I(q)$ of 1 wt% SiNP7 and 4.68 mg/mL cytochrome *c* in D_2O at pH 8.3 (points). In panel (a), (b) and (c) the solid line represents a simulation of different scenarios based on the experimental parameters. The inset sketches illustrate the conceptual picture of the model used for the respective simulation. (a) The silica particles and the protein molecules are modeled as separate, non-interacting entities. (b): The silica particles are surrounded by an effective shell of proteins with a homogeneous SLD. (c): Silica particles and protein are modeled as composite consisting of a central silica particle decorated with individual cytochrome *c* molecules, each with its individual SLD. The solid red and black lines represent simulation results for 2 different sizes for the attached cytochrome *c*. Tabulated simulation parameters are given in Table 5.2. (d) The sketch depicting the 'raspberry-like' scattering model used for the simulations in (c).

The composite form factor of a mixture of non-interacting spheres and ellipsoids, representing the silica NPs and cytochrome *c*, respectively, is shown in Figure 5.1a. In this case, the theoretical scattering intensity was calculated by the linear combination of two form factors. The parameter values used to simulate the scattering profile are given in Table 5.2. As can be seen in Figure 5.1a, this model prediction of the scattering intensity gives a poor representation of the experimental scattering profile in the q -range between 0.5 and 1.5 nm^{-1} . This clearly shows that the model of coexisting independent species is not appropriate for the present system. Earlier studies have shown that at this pH and protein concentration, cytochrome *c* is strongly bound to the surface of the silica nanoparticles.⁶⁴ Hence the model of independent non-interacting silica and cytochrome *c* is unrealistic, and linear combination of the individual form-factors for spheres and ellipsoids does not reproduce the experimental scattering profile (Fig. 5.1a).

The model describing the adsorbed protein as a uniform shell around the central silica particle is shown in Figure 5.1b (parameters in Table 5.2). The details of the analytical expression used to simulate the core-shell particle scattering profile are provided elsewhere.¹⁴¹

The fraction of SiNP surface covered with protein was calculated as $\phi_p^a = (N_{\text{protein}} A_{\text{protein}}) / A_{\text{SiNP}}$ where A_{protein} and A_{SiNP} are the surface area of protein and SiNP respectively and N_{protein} the number of proteins on the surface. As can be observed in Figure 5.1b, this simple core-shell model fails to represent the scattering intensity variation at $q > 0.5 \text{ nm}^{-1}$, where it underestimates the scattered intensity. One major drawback of the core-shell model is the assumption of uniform protein layer (shell) formation around the particles, which ignores the discrete nature of adsorbed protein molecules separated from each other by the dispersing medium. Moreover, the higher experimental scattering intensity at $q > 0.5 \text{ nm}^{-1}$, is a signature of larger surface area probed by the incident neutrons. This observation is reminiscent of adsorption of non-ionic surfactants onto silica surface, where similar decrease in scattering profile indicated the formation of discrete micelles on nanocurved surfaces.^{142,143}

A scattering model accounting for such scatterers was reported by Larson-Smith et al.⁴⁴ The authors derived an analytical model for interpreting the scattering profiles from Pickering emulsions as ‘raspberry-like’ particles (RB-model). The model assumes a random distribution of small particles on a larger central spherical particle (Fig. 5.1d). The form factor of the raspberry-like particles can be calculated by solving Debye equations.^{44,144} The net scattering intensity from a ‘raspberry-like’ particle is given as

Table 5.2: Model parameters of the simulations in Figure 5.1. Simulations were based on the assumption of (a) individual, non-interacting SiNP and cytochrome *c* particles; (b) a core-shell particle consisting of a central silica sphere and a uniform shell of cytochrome *c* molecules; (c) a central silica sphere decorated with individual cytochrome *c* molecules.

Parameter	(a) Individual scattering spheres and ellipsoids	(b) Core-shell model	(c) ‘raspberry-like’ particles
$D_{\text{SiNP}}/\text{nm}$	7.2	7.2	7.2
$\text{PDI}_{\text{SiNP}}/-$	0.171	0.171	0.171
$\varphi_{\text{SiNP}}/-$	0.0050	$0.0231)^1$	0.0050
$D_{\text{protein}}/\text{nm}$	$D_p^{\text{ax}} = 2.4$ $D_p^{\text{eq}} = 3.6$	$2.4)^2$	2.4/3.6
$\varphi_{\text{protein}}/-$	0.0041	0.0041	0.0041
$\text{SLD}_{\text{SiNP}}/\text{\AA}^2$	$3.48 \cdot 10^{-6}$	$3.48 \cdot 10^{-6}$	$3.48 \cdot 10^{-6}$
$\text{SLD}_{\text{protein}}/\text{\AA}^2$	$3.07 \cdot 10^{-6}$	$5.64 \cdot 10^{-6}$	$3.07 \cdot 10^{-6}$
$\text{SLD}_{\text{solvent}}/\text{\AA}^2$	$6.09 \cdot 10^{-6}$	$6.09 \cdot 10^{-6}$	$6.09 \cdot 10^{-6}$
$\phi_p^a/-)^3$	$-)^4$	$-)^4$	0.54/0.35

¹ volume fraction of the complete core-shell particle; ² corresponds to the shell thickness in the core-shell model;

³ fraction of SiNP surface covered with protein was calculated as $\phi_p^a = (N_{\text{protein}} A_{\text{protein}}) / A_{\text{SiNP}}$; ⁴ this parameter is not necessary in this model

$$I(q) = \left(\phi_s V_s \Delta \rho_s^2 + \frac{\phi_p^2 \phi_p^a V_s}{\phi_s} \Delta \rho_p^2 \right) P_{ps}(q) + (\phi_p (1 - \phi_p^a) V_p \Delta \rho_p^2) \Psi_p^2(q) \quad (5.2)$$

where ϕ_p and ϕ_s are the total volume fraction of protein and silica respectively, ϕ_p^a is the fraction of protein bound to silica surface, V_p and V_s are respective volumes of a cytochrome *c* molecule and a silica nanoparticle, $\Delta \rho_p = |\rho_{\text{protein}} - \rho_{\text{D}_2\text{O}}|$, and $\Delta \rho_s = |\rho_{\text{silica}} - \rho_{\text{D}_2\text{O}}|$ are the neutron scattering length density contrasts of protein and silica against the dispersing medium (here D_2O); $P_{ps}(q)$ and $\Psi_p^2(q)$ are the form factors of ‘raspberry-like’ particles, and protein molecules. This model accounts for the scattering from the protein molecules bound to the silica nanoparticles as well as the unbound protein in the dispersion. In this experimental study, all parameters of Equation 5.2 are known, except the cytochrome *c* diameter (D_p), and the fractional surface coverage of the central particle (ϕ_p^a). Hence, the experimental SANS profiles of cytochrome *c* bound to silica nanoparticles can be fitted using the RB-model with only D_p and ϕ_p^a as free parameters.

Analytical simulations of the RB-model using two protein radii and experimental SANS data for SiNP7 are shown in Figure 5.1c. The simulation with $D_p = 2.4$ nm represents well the experimental SANS profile whereas a simulation with $D_p = 3.6$ nm shows major deviations from the experimental data around 1 nm^{-1} . The high- q region ($q > 0.4 \text{ nm}^{-1}$), which corresponds to shorter length scales, sensitive to the local orientation of protein, is well reproduced by the RB-model. This simple example shows the applicability of the RB-model to the present experimental system of protein bound silica nanospheres. The sensitivity of the RB-model to small differences in D_p (Fig. 5.1c), offer a unique possibility to precisely determine the radius of adsorbed proteins.

The SANS experiments were performed for dispersions of SiNP of three different sizes containing cytochrome *c* at different pH values. The amount of protein was kept constant for all silica dispersions. The RB-form factor model was used to fit the experimental SANS profiles in the pH range 2-11. The corresponding fits for SiNP7, and SiNP13 dispersion containing the protein are shown in Figure 5.2, and the fits for SiNP41 are shown in the Appendix (Fig. 5.7). All the parameter values used in the fitting process are provided in Table 5.3 and 5.4 in the Appendix. As can be seen from Figure 5.2a and 5.2b, the RB-model gives an excellent fit of the experimental scattering curves. Specifically, the model is able to reproduce the high- q scattering observed in Porod’s regime, which can be attributed to surface roughness induced by the adsorbed protein on silica surface. The discrepancies between the model and experimental scattering at low- q regime can be attributed to the formation of protein bridged silica aggregates. The aggregation of SiNP is observed only in the pH range 4.5 – 7.0, and greatly influences the scattering intensity profile at $q < 0.6 \text{ nm}^{-1}$. This can also be observed in the photographs of the samples shown in Figure 5.2c and 5.2d. A detailed study of silica particle

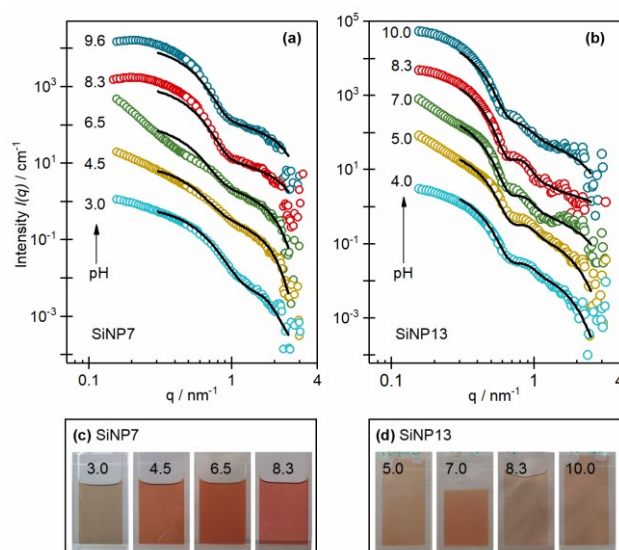


Figure 5.2: Small angle neutron scattering intensity profiles $I(q)$ for (a) SiNP7 and (b) SiNP13 particles in D_2O with a fixed amount of cytochrome c at different bulk pH values as indicated in the graph. Solid lines represent fits with the RB-model. Tabulated fit parameters are given in Table 5.3 in the Appendix. The curves are shifted by a constant factor of 10 for better visualization. The photographs show the samples for (c) SiNP7 and (d) SiNP13 silica particles, as measured in the SANS experiments. Only the sample at pH 4.5 – 7.0 showed pronounced bulk aggregation, all other dispersions remained stable upon protein addition.

aggregation induced by the adsorption of lysozyme and cytochrome c has been reported previously.^{31,32} In addition, a difference in color of the silica-cytochrome c dispersion was observed at different pH values which can be attributed to the change in the oxidation state of the iron in the heme c group of the adsorbed cytochrome c .

It is important to note that the protein binds onto the silica surface due to local electrostatic attraction, and a change in pH modulates these surface charge driven interactions.³¹ It was previously shown that the amount of cytochrome c bound to the silica surface changes significantly with change in pH.⁶⁴ Hence, in the dispersions used for the SANS experiments in Figure 5.2 not the same fraction of protein was bound to the silica surface. However, the fractional surface coverage of silica at a given pH can be estimated using protein binding isotherms (Fig. 5.9, Appendix), which can be compared with the surface coverage values estimated using RB-model based curve fittings. The fractional silica surface covered with protein as obtained by RB-model fitting and the estimated coverage from adsorption isotherms for SiNP7 are shown in Figure 5.3b (data for SiNP13 and SiNP41 are shown in the Appendix Fig. 5.10). As can be observed, the experimentally calculated silica surface coverage and the RB-model fit values are in good agreement. This further ascertains the applicability of the fitting model to this specific experimental dispersion.

The RB-model allows a precise determination of the diameter of protein adsorbed onto the nanoparticle surface. The apparent diameter (D_p) of the adsorbed protein obtained by model fitting shows a decrease with increasing pH for all three silica particle dispersions. The fit value of D_p decreases from 3.5 nm in acidic pH to 2.2 nm for neutral and basic pH. In the case of

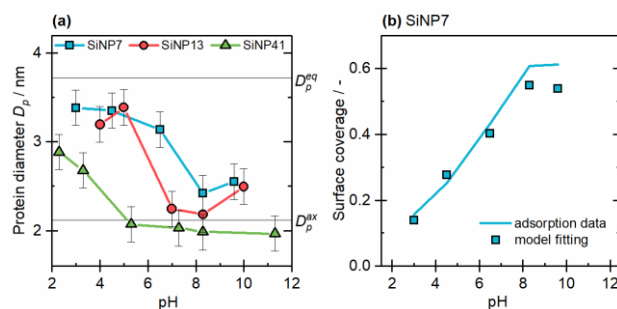


Figure 5.3: (a) Protein diameter as derived from neutron scattering experiments by fitting the scattering intensity profiles with a form factor model for ‘raspberry-like’ particles. Three different particle sizes were evaluated. All dispersions show a drop in the diameter of adsorbed cytochrome *c* with increasing pH. Solid lines indicate the equatorial (semi-major axis) and axial (semi-minor axis) diameter of native cytochrome *c* derived from neutron scattering experiments. (b) Comparison of the fractional surface covered with cytochrome *c* as obtained from the RB model fitting of the SANS data (points) with the expected coverage derived from adsorption isotherms (solid line) for the SiNP7.

SiNP7 and SiNP13, the apparent size change begins at $\text{pH} > 4$, and is completed at $\text{pH} 7$. Whereas in the case of SiNP41, apparent size transition begins at much lower pH (~ 2), and completes at $\text{pH} < 6$ (Fig. 5.3a). The average equatorial diameter of the oblate cytochrome *c* molecule has been determined by SANS measurements (Fig. 5.7, Appendix), and are represented by dashed lines in Figure 5.3a. It is important to remember that the diameters of native unadsorbed cytochrome *c* were found to be stable over the entire experimental pH range. A pH induced deformation of the shape of protein is therefore not expected in the adsorbed state. This assumption is confirmed by Kondo et al.³⁹, where the authors compared CD spectra of different proteins in their native and adsorbed state and concluded that hard proteins (e.g. cytochrome *c*) undergo only minor changes upon adsorption on small silica nanoparticles. Baring the values for the equatorial and axial diameter of native cytochrome *c* in mind, it can be hypothesized that the protein adsorbs onto silica in a ‘head-on’ configuration at low pH , and a ‘side-on’ state at higher pH values (Fig. 5.3a). This change in configuration of cytochrome *c* is in agreement with previous report on the pH driven re-orientation of human carbonic anhydrase II on silica surface, where the similar effect was observed.⁴²

5.4 Charge Distribution on Cytochrome *c*

To gain insight into the origin of the reorientation of protein on silica nanoparticles, the pH induced change in the surface charge distribution on cytochrome *c* was estimated. Depending upon the amino acid composition of a protein and their local physiochemical environment, the ionization state of functional group varies significantly. This results into a non-uniform distribution of charges on a protein, which further induces a net non-zero dipole moment, $\vec{\mu}$, in the protein. Here the dipole moment was used as a quantitative measure of asymmetry in the

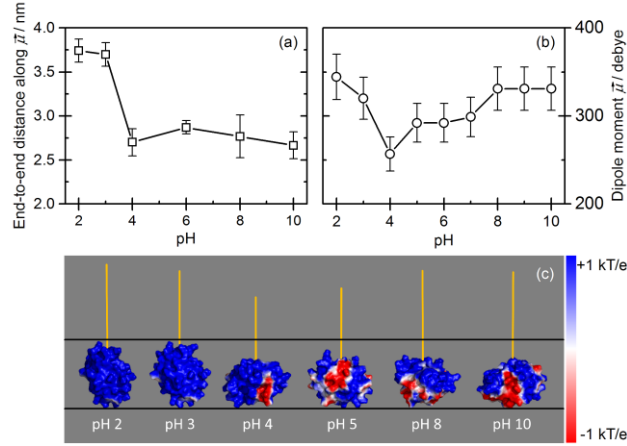


Figure 5.4: (a) Left ordinate: End-to-end distances of cytochrome *c* (circles) measured along the dipole moment axes for different pH values. Each point is an average of at least 6 interatomic distances between the point where the dipole moment vector intersects the protein surface and the opposite side. (b) Magnitude of the dipole moment (squares) of cytochrome *c* as a function of pH. (c) Electrostatic surface maps for the 2GIW structure of cytochrome *c* for different pH as indicated below the structure. The dipole moment vector is represented as a line, with its length proportional to the magnitude of the dipole moment vector. Here the protein is visualized such that the dipole moment vector remains parallel to the viewing plane.

surface charge distribution, and was correlated with the pH dependent binding of cytochrome *c* on silica nanoparticles.

The atomic coordinates of the solution structure 2GIW⁶⁶ of cytochrome *c* in the protein data base (PDB) were used to perform the calculations. The correct protonation state of cytochrome *c* was calculated for each pH with PDB2PQR software tool.^{67,68} The net dipole moment was calculated using the vector sum, as⁷¹

$$\vec{\mu} = \sum_i q_i (\vec{r}_i - \vec{r}_r) \quad (5.3)$$

where the i -th charge q_i is at the distance r_i from a constant reference point r_r . This procedure neglects any conformational changes of cytochrome *c* induced by changing the pH. Electrostatic surface maps of cytochrome *c* were generated using the software Adaptive Poisson – Boltzmann Solver⁷⁵ in combination with the protonation data given by PDB2PQR. Further details on the procedure are provided in Chapter 2.3.

The calculations performed assisted in the construction of detailed 3D surface electrostatic maps of the protein at different pH and corresponding dipole moment was calculated using Equation 5.3. The magnitude of the dipole moment remains nearly constant around 300 Debye over the entire pH range (Fig. 5.4b). This value is in good agreement with the experimentally measured dipole moment values for horse heart cytochrome *c*.¹⁴⁵ However, the orientation of the dipole moment relative to the protein changes greatly with pH (Fig. 5.4a). The electrostatic surface maps for cytochrome *c* at different pH are shown in Figure 5.4c, the viewing perspective is such that imaging plane remains parallel to dipole moment vector. Hence

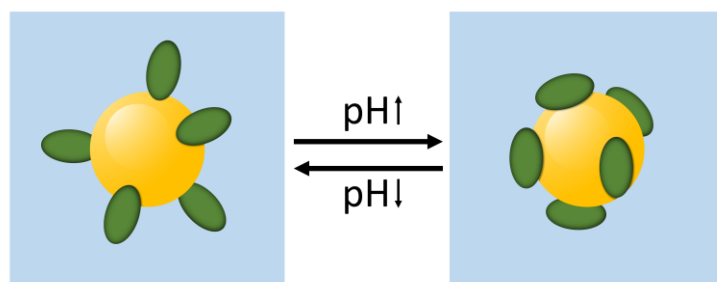


Figure 5.5: Schematic view of the proposed pH-dependent adsorption behavior for cytochrome *c* (green ellipsoids) on silica nanoparticles (yellow spheres). A shift in pH leads to a change in the orientation of the adsorbed cytochrome *c* molecule.

the rotation of cytochrome *c* (Fig. 5.4c), is a signature of the changes in surface charge distribution patterns. The calculations show a change in the direction of dipole moment vector at pH 4. This behavior can be rationalized by measuring the end-to-end distance of the cytochrome *c* along the direction of dipole moment vector. The variation of this distance with pH is displayed in Figure 5.4a. The figure clearly shows that the dipole moment for $\text{pH} < 4$ is oriented parallel to the equatorial axis (longer) of cytochrome *c*. At higher pH the dipole moment becomes parallel to the shorter axis of cytochrome *c*.

5.5 Discussion and Conclusions

Comparing the results of the SANS experiments with the calculations of the dipole moment of cytochrome *c* it stands out that the observed changes in the protein orientation are occurring at similar pH values. This implies a connection between the reduction of D_p and the shift of the dipole moment of cytochrome *c*. Since the dipole moment vector points towards the positive side of separated charges, in the present case this refers to the larger positive patch on cytochrome *c*. At low pH the dipole moment points along the semi-major axis thus the protein molecule is forced to align in a way that the dipole moment points towards the negatively charged silica surface. For higher the bulk pH the dipole moment reorients along the semi-minor axis and consequently the orientation of the entire protein relative to the surface will change accordingly (Fig. 5.5). Such preferential protein binding via its positive patch has been shown experimentally for human carbonic anhydrase II⁴² and simulated for lysozyme on amorphous silica surfaces.⁴³ In all these cases the interaction resulting into the binding of protein to silica surfaces is primarily electrostatic. Fraaje et al.¹⁴⁶ concluded on the basis of total internal reflection fluorescence microscopy, that the orientation of cytochrome *c* on a planar SnO_2 electrode (positively charged at pH 4) can be affected by the interfacial potential during the adsorption process. More complex situation arise when the binding of protein occurs with hydrophobic or entropy driven interactions which are beyond the scope of the present study. However, the SANS based experimental methodology of determining the protein orientation on

surfaces developed here can be applied to understand non-electrostatic complex bio-nano interactions, and corresponding effects on the protein functionality.

In conclusions, the equilibrium orientation of ellipsoidal shaped protein, cytochrome *c*, on the surface of silica nanoparticles was studied. Small angle neutron scattering technique was used to determine the local orientation of the protein on silica nanoparticles of 7, 13, and 41 nm diameter. A ‘raspberry-like’ particle model was used to analyze the experimental scattering profiles in the pH regime 2 – 11. For all three silica nanoparticle sizes, it was found that at $\text{pH} < 4$, the protein adsorbs with a ‘head-on’ configuration. Whereas at higher pH values, the protein reorients on the silica surface with a ‘side-on’ configuration as a preferential binding state. The experimental observation were interpreted based on the change in the surface charge distribution on protein molecules. On the basis of electrostatic surface mapping and the end-to-end distance of cytochrome *c* along the dipole moment vector, it was concluded that the observed reorientation of the protein molecule on silica surface is due to the reorganization of the surface charges on the protein. The experimental findings, and their theoretical interpretation provide a new methodology of investigating and predicting protein orientations on nanocurved surfaces. This approach may assist in better understanding of bio-nano interactions, which would further help in developing new platforms for advanced biomedical applications.

5.6 Appendix

5.6.1 Characterization of Silica Particles and Cytochrome *c*

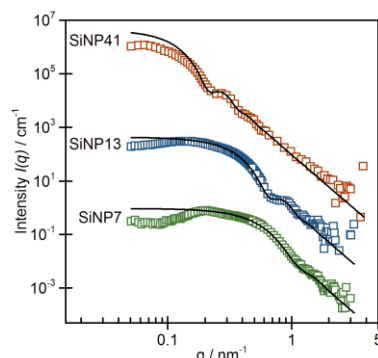


Figure 5.6: Small angle neutron scattering intensity profiles $I(q)$ for SiNP7, SiNP13 and SiNP41 particles in D_2O without any added of cytochrome *c* at pH 8.3. Solid lines represent fits with a form factor model accounting for non-interacting solid spheres. Tabulated fit parameter are given in Table 5.1. The curves are shifted by a constant factor of 100 for better visualization.

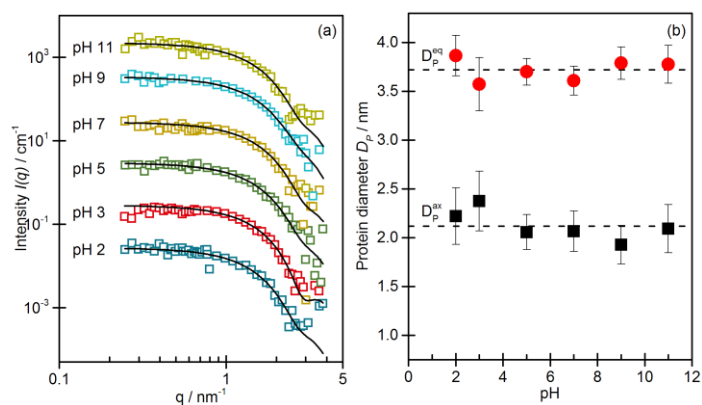


Figure 5.7: (a) Small angle neutron scattering intensity profiles $I(q)$ for cytochrome *c* in D_2O in the absence of nanoparticles at different bulk pH values as indicated in the graph. Solid lines represent fits with a form factor model accounting for non-interacting ellipsoid. The curves are shifted by a constant factor of 10 for better visualization. (b) The resulting fit values for the equatorial and axial axis of the ellipsoidal model for different pH conditions. The dashed line represent the mean value of the displayed data points.

5.6.2 Fitting of SANS Data with the RB-model

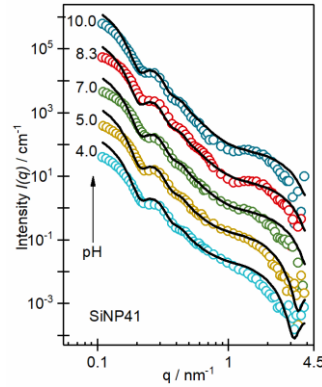


Figure 5.8: Small angle neutron scattering intensity profiles $I(q)$ for SiNP41 particles in D_2O with a fixed amount of cytochrome c at different bulk pH values as indicated in the graph. The curves are shifted by a constant factor of 10 for better visualization.

Table 5.3: Values of the fixed general parameters used for the RB-model fitting of the SANS intensity curves Figure 5.2 and 5.8. With the diameter of the silica particle D_{SiNP} , its polydispersity s_{SiNP} , volume fractions of silica φ_{SiNP} and cytochrome c $\varphi_{protein}$, scattering length densities SLD of silica, solvent and cytochrome c and Δ parameter accounting for penetration of the central particle by the outer particles.

	SiNP7	SiNP13	SiNP41
D_{SiNP}/nm	7.2	12.9	40.8
$s_{SiNP}/-$	0.17	0.14	0.13
$\varphi_{SiNP}/-$	0.0051	0.0051	0.0164
$\varphi_{protein}/-$	0.0041	0.0012	0.0032
$SLD_{SiNP}/\text{\AA}^2$		$3.48 \cdot 10^{-6}$	
$SLD_{solvent}/\text{\AA}^2$		$6.09 \cdot 10^{-6}$	
$SLD_{protein}/\text{\AA}^2$		$2.90 \cdot 10^{-6}$	
$\Delta/-$		1.00	

Table 5.4: Best fit values of the open parameters for the RB-model fitting of the SANS intensity curves Figure 5.2 and 5.8 at different pH. The diameter of the adsorbed cytochrome c , D_{prot} , and the fraction of the nanoparticle surface covered with protein $\varphi_{surf, p}$.

SiNP7			SiNP13			SiNP41		
pH	$\frac{D_{prot}}{nm}$	$\varphi_{surf, p}$	pH	$\frac{D_{prot}}{nm}$	$\varphi_{surf, p}$	pH	$\frac{D_{prot}}{nm}$	$\varphi_{surf, p}$
3.0	3.4	0.14	4.0	3.2	0.03	2.3	2.9	0.40
4.5	3.4	0.28	5.0	3.4	0.06	3.3	2.7	0.47
6.5	3.1	0.40	7.0	2.2	0.41	5.3	2.1	0.49
8.3	2.4	0.55	8.3	1.9	0.47	7.3	2.0	0.90
9.6	2.6	0.54	10.0	2.2	0.32	8.3	2.0	0.70
						11.3	2.0	0.85

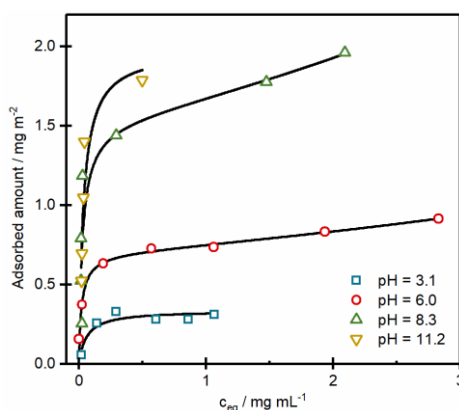


Figure 5.9: Adsorption isotherms for cytochrome *c* on silica nanoparticles (Ludox TMA, $D_{SINP} = 27$ nm) at different pH conditions (as indicated in the legend). Solid lines are fits with the GAB model introduced in Chapter 3. Best fit values are given in Table 5.5. Experiments were performed according to the established methods, for details see Chapter 3.

5.6.3 Adsorption Isotherms and Calculation of Expected Surface Coverage

In order to estimate the surface coverage of cytochrome *c* on the silica particles during the SANS measurements a series of adsorption isotherms were collected at different pH conditions. The results are displayed in Figure 5.9 together with the respective GAB model fits (cf. Chap. 3), best fit values for GAB parameter are tabulated in Table 5.5. As the GAB parameter are highly pH dependent the individual values of each sample were interpolated for the respective pH conditions. Together with the knowledge of the starting concentration of cytochrome *c* in the SANS sample it is possible to calculate the adsorbed amount. Fractional surface coverages are calculated based on the assumption of a side-on footprint of the cytochrome *c* molecule. Figure 5.10 shows the fractional surface coverage for the SANS samples as deduced by the isotherms together with the fitting results by the RB-model. It is important to compare these values, as this parameter was used to judge about the quality of the fit. Although, some minor deviations between the expected and the fitted fractional surface coverage the values are in good agreement.

Table 5.5: Best fit values of the GAB parameters for the experimental adsorption isotherms in Figure 5.9.

pH	3.1	6.0	8.3	11.2
Γ_m	0.34	0.71	1.52	1.98
K_S	16.3	45.1	36.4	28.0
K_L	0	0.08	0.10	0

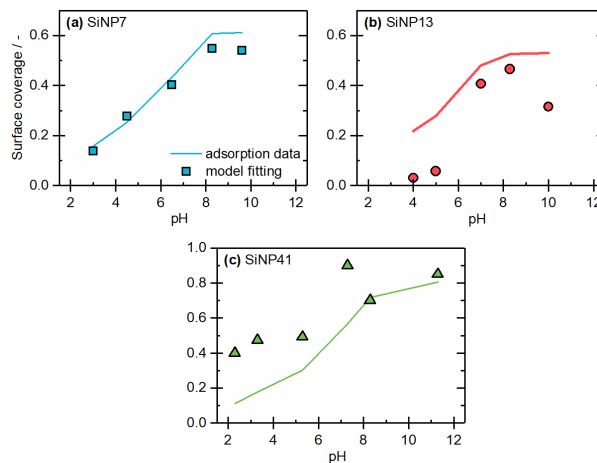


Figure 5.10: Comparison of the fractional surface coverages as deduced from the adsorption isotherms (Fig 5.9) and the best fit values from the RB-model from the SANS measurement for (a) SiNP7, (b) SiNP13 and (c) SiNP41. The points represent the data points from the RB-model, the solid lines are connecting the calculated points from the adsorption data at the respective pH.

5.6.4 Instrumental Details SANS

For the SANS experiments presented here two sets of SANS data were used, collected at two different neutron sources. The data for native cytochrome *c* and the 40 nm silica particles with adsorbed cytochrome *c* were collected at the instrument PAXY at the Laboratoire Léon Brillouin (LLB) in Saclay (France). During a second beam time, the data for 7 nm and 14 nm silica particles with adsorbed cytochrome *c* were collected. These experiments were done at the KWS 1 instrument at the Forschungsreaktor München II (FRM II) neutron source in Garching, Germany. The experimental details on the used instrumental setups at the respective instruments are summarized in Table 5.6.

Table 5.6: Best fit values of the GAB parameters for the experimental adsorption isotherms in Figure 5.9.

	Setup	K1	K2	K3
Paxy	Wavelength λ / nm	5.00	5.00	17.00
	Collimation length / m)*)*)*
	Detector distance / m	1.1	5.0	5.0
	Beam size / mm ²	10 × 10	10 × 10	10 × 10
KWS 1	Wavelength λ / nm	4.50	4.50	4.50
	Collimation length / m	8.0	20.0	20.0
	Detector distance / m	2.0	4.0	20.0
	Beam size / mm ²	30 × 30	30 × 30	30 × 30

)* At this instrument the collimation length was automatically optimized according to the sample/detector distance.

Chapter 6 Protein Immobilization in Surface-Functionalized SBA-15: Predicting the Uptake Capacity from the Pore Structure⁴

6.1 Introduction

Ordered mesoporous silica (OMS) materials have attracted much attention as hosts for the immobilization and thermal stabilization of enzymes,^{12–14} and as delivery systems for proteins and peptides.^{14–16} Favorable properties of OMS materials include their large internal surface area combined with high mechanical strength,¹⁴⁷ the possibility to adjust the size and arrangement of the pores, and the ability to modify the surface properties to match the targeted enzyme.^{12,16} In addition, recent studies indicate that immobilization at the walls of nanosized pores can cause enhanced thermal stability and enzymatic activity compared to the free protein.^{21–24} This trend has been attributed to the high surface curvature of the pore wall and the resulting crowded microenvironment of the protein in the pores, which may provide stability against unfolding.

The protein immobilization capacity of OMS materials depends on their specific pore volume and pore size distribution.^{17,148,149} SBA-15 and other materials prepared with block copolymer surfactants as the structure-directing template exhibit a complex pore structure with irregular intrawall micro- and mesopores in addition to the regular main channels. The level of secondary porosity depends on the synthesis temperature, the postsynthesis heat treatment, and the procedure of template removal. The pore structure of SBA-15 has been studied by state-of-the-art gas adsorption analysis^{150,151} and structure-sensitive methods including small-angle XRD^{152–154} and neutron scattering,¹⁵⁵ and electron tomography.¹⁵⁶ Surface-functionalized SBA-15 materials prepared by co-condensation of the silica precursor with functional siloxanes¹⁹ can exhibit even higher degrees of structural complexity. In the past, these structural features have not been taken into account in the assessment of the protein uptake capacity. Usually it is inferred that the amount of immobilized protein is directly proportional to the specific pore volume of the sample. However, this assumption is not justified for samples exhibiting secondary porosity, when part of the pore volume is not accessible for the protein.

It is well-established that the adsorption of conformationally stable (“hard”) proteins like lysozyme to silica surfaces is dominated by electrostatic interactions.^{31,32,157} Accordingly, the protein binding strength and limiting adsorption are strongly dependent on pH and on the ionic strength of the solution.^{158–160} Globular proteins can fill the pore space of OMS most efficiently at a pH corresponding to their isoelectric point (IEP),^{149,161} because the repulsive

⁴ Reproduced with permission from J. Meissner, A. Prause, C. Di Tommaso, B. Bharti, G. H. Findenegg, *J. Phys. Chem. C* **2015**, 119 (5), 2438. Copyright 2015 American Chemical Society.
<http://dx.doi.org/10.1021/jp5096745>

electrostatic interaction between the protein molecules is minimal at this point. Many reports in the literature suggest that the immobilization capacity of OMS for proteins can be enhanced by surface-functionalization with acidic or basic groups, to promote stronger electrostatic interaction between the host and guest.^{12–15,24,148,162–164} Hence, to promote the adsorption of the positively charged lysozyme (IEP = 11) the negative charge density of the pore walls can be increased, either by partial replacement of Si by Al atoms,¹⁶¹ or by surface functionalization with negatively charged groups.^{19,24,165}

In this chapter we show how the secondary porosity of chemically functionalized SBA-15 materials can be characterized quantitatively and taken into account in the assessment of the protein immobilization capacity. Our method for estimating the protein uptake capacity extends the geometrical model of Sang, Vinu, and Coppens,¹⁴⁹ by taking into account the nonideal pore-size distribution of the matrix. The application of the new predictive tool is demonstrated by a comparative study of the uptake of the globular protein lysozyme in native and surface-functionalized SBA-15 materials. Functionalization with propylsulfonic acid was chosen to find out if the adsorption of the positively charged protein can be enhanced by increasing the negative surface charge density at the pore walls. Since the surface of protein molecules exhibits both positively and negatively charged patches, the availability of positive and negative charges at the pore walls might favor protein binding. In order to probe this possibility, SBA-15 was functionalized with a zwitterionic sulfobetaine. Zwitterionic coatings at free surfaces are known to reduce nonspecific adsorption of biomolecules.^{25,166} It was of interest to find out if the protein-repellent nature of zwitterionic coatings is preserved in the confined geometry of nanometer-sized pores, or if the crowded microenvironment in the pores might even cause enhanced binding of the protein. The broader question about the influence of surface-functionalization on the thermal stability or enzymatic activity of the immobilized protein is outside the scope of this article.

6.2 Pore filling Model

A model for estimating the maximum uptake of globular proteins in the cylindrical channels of OMS materials was presented by Sang, Vinu, and Coppens (SVC).¹⁴⁹ This model assumes that the entire pore volume v_p consists of cylindrical pores of uniform diameter D . This can be a good approximation for MCM-41 but not for SBA-15, where secondary (intrawall) porosity makes a significant contribution to the pore volume (see Section 6.3.2). For materials having a distribution of pore sizes the SVC model can be generalized by adding up the number of protein molecules in pores of different sizes. For the maximum amount of protein in the pore space we obtain (see Appendix)

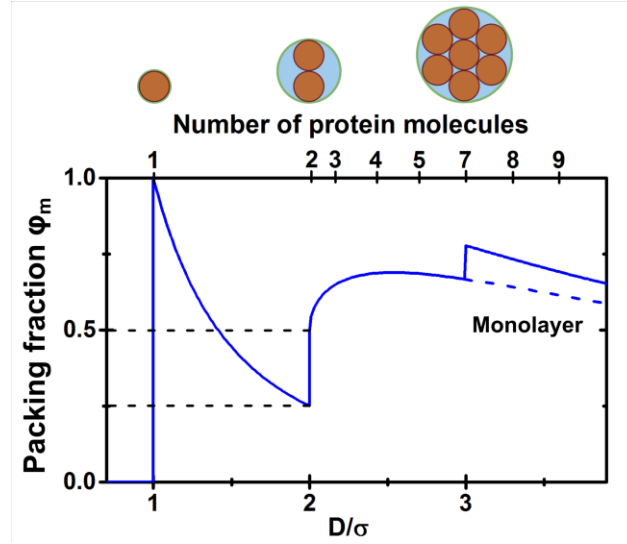


Figure 6.1: Protein packing fraction ϕ_m in cylindrical pores as a function of the reduced pore diameter D/σ . For hard protein molecules (diameter σ) only discrete values of N are possible (top scale), and sharp changes in ϕ_m appear at integer values of D/σ , as indicated by the sketched pores, where the red circles represent protein molecules.

$$n_{\text{pore}} = \frac{1}{N_A v_{\text{prot}}} \int \phi_{\text{prot}}(D) f(D) dD \quad (6.1)$$

where N_A is the Avogadro constant and v_{prot} the volume of a protein molecule; $\phi_{\text{prot}}(D)$ represents the protein packing fraction (maximum volume fraction of protein) in pores of diameter D , and $f(D) = dv_p/dD$ is the pore-size distribution function. Following SVC¹⁴⁹ we assume that prolate-shaped proteins like lysozyme are adsorbed side-on to the pore wall, and we neglect packing effects of molecules in the direction of the pore axis. This is equivalent to assuming that the protein molecules represent cylinders with $v_{\text{prot}} = (\pi/4)\sigma^2\delta$, where σ and δ denote the minor and major cross-sectional diameters. The protein packing fraction then becomes (see Appendix)

$$\phi_m(D) = \frac{N(D)}{(D/\sigma)^2} \quad (6.2)$$

where $N(D)$ is the maximum number of circles (diameter σ) that can be accommodated inside a circle of diameter D . Depending on the size ratio D/σ this number is given by

$$N(D/\sigma) = \begin{cases} 0 & D/\sigma < 1 \\ 1 & 1 < D/\sigma < 2 \\ N_1 & 2 < D/\sigma < 3 \\ N_1 + 1 & 3 < D/\sigma < 4 \end{cases} \quad (6.3)$$

with¹⁴⁹

$$N_1 = \pi \left(\arcsin \frac{\sigma}{D - \sigma} \right)^{-1} \quad (6.4)$$

Figure 6.1 shows $\phi_m(D)$ plotted as a function of the reduced pore diameter D/σ . The maximum number of particles N that can be accommodated in the cross-section of the pore for given D/σ is also indicated. The steps in $\phi_m(D)$ at integer values of D/σ represent the diameters at which it becomes possible to place one more protein molecule along a pore diameter. When only a single layer of protein molecules is formed at the pore wall while the pore center remains vacant, $\phi_m(D)$ becomes a smoothly varying function above $D/\sigma = 2$, with a shallow maximum near $D/\sigma = 2.5$. For lysozyme in the cylindrical pore channels of the present SBA-15 materials, D/σ is between 2.5 and 3.0, i.e., close to this local maximum in $\phi_m(D)$, but adsorption into secondary pores of diameters $D > \sigma$ will also contribute to the overall protein uptake. Hence a characterization of the secondary porosity of OMS materials is important for the assessment of their protein immobilization capacity.

6.3 Results

6.3.1 Functionalized SBA-15 Materials

Three OMS materials were used in this work: native SBA-15, sulfonic-acid functionalized SBA-15 (SO₃-SBA) and zwitterionic functionalized SBA-15 (Zwi-SBA) (see Appendix). The materials were characterized by powder XRD, nitrogen adsorption, TEM, and TGA. The XRD profiles (Fig. 6.2a) confirm the 2D-hexagonal pore lattice of the materials and give the lattice constant a_0 (Table 6.1). The nitrogen sorption isotherms (Fig. 6.2b) exhibit the characteristic type IV behavior with a H1 hysteresis loop. The pore size distribution of the three samples (shown as inset in the panels of Fig. 6.2b) exhibits a narrow peak corresponding to the main

Table 6.1: Characterization of Pore Texture of the SBA-15 Materials: Lattice parameter a_0 , mesopore diameter \bar{D} (KJS method, adsorption branch), specific surface area a_S (BET method), single point pore volume v_p (extrapolation of linear region to $p/p_0 = 1$), micropore volume v_p^{micro} (t -plot method), mass ratio of functional organic group to silica m_F/m_S (from TGA), and mean particle diameter D_{part} of the samples.

	a_0	\bar{D}	a_S	v_p	v_p^{micro}	m_F/m_S	D_{part}
sample	nm	nm	m ² /g	cm ³ /g	cm ³ /g	-	nm
SBA-15	11.1	7.7	780	0.93	0.05	0	350
SO ₃ -SBA	11.8	8.0	660	0.81	0.02	0.23	120
Zwi-SBA	11.8	8.0	345	0.48	0.02	0.30	300

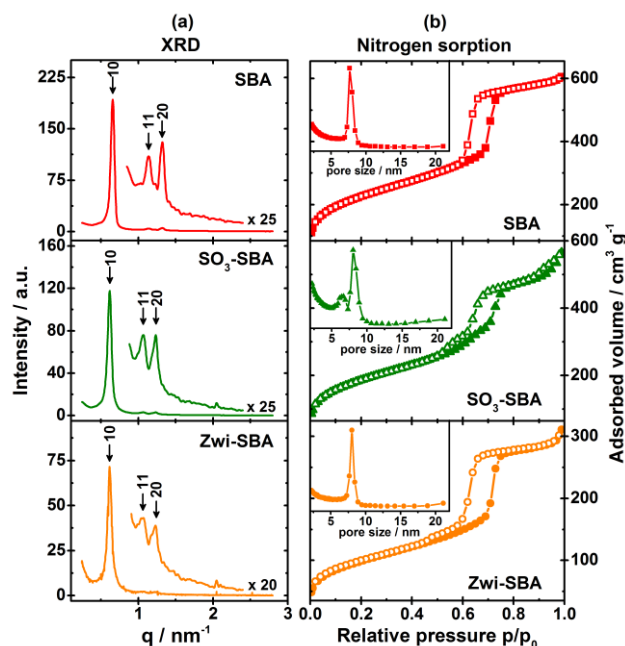


Figure 6.2: Characterization of the three SBA-15 materials: (a) small-angle powder XRD showing the 10, 11, and 20 Bragg reflections; (b) nitrogen adsorption/desorption isotherms and resulting pore size distribution (inset).

cylindrical channels and different levels of intrawall porosity at the lower end of the mesopore range.¹⁵⁰ The SO₃-SBA sample shows, in addition, a satellite peak with pores of 6 – 7 nm next to the peak of the main 8 nm channels. For this sample the hysteresis loop extends down to $p/p_0 = 0.5$, reminiscent of the behavior of plugged SBA-15 materials.¹⁶⁷ The pronounced increase of the adsorption isotherm at $p/p_0 > 0.9$ found for this sample is attributed to condensation of nitrogen in voids between silica particles. This interparticle pore volume was neglected in the further analysis. Parameters derived from the nitrogen adsorption isotherm are included in Table 6.1. The mean particle diameter of the OMS materials, D_{part} , which is needed to estimate the protein adsorption at the external surface of the particles, was determined from TEM images. Values of D_{part} are also included in Table 6.1. Representative TEM images are presented in the Appendix.

TGA scans for the three samples are shown in Figure 6.3, and results derived from TGA are summarized in Table 6.4 of the Appendix. The weight loss of the samples below 100 °C ($5 \pm 0.5\%$ for native SBA-15; $9 \pm 0.5\%$ for the two functionalized materials) is due to the evaporation of adsorbed water. The weight loss above 300 °C can be attributed to the decomposition of the functional organic group and any remaining (nonextracted) template. From the relative mass of the dry samples below the decomposition step ($m_S + m_F = 0.91$ at 100 °C) and above this step ($m_S = 0.74$ for SO₃-SBA; $m_S = 0.69$ for Zwi-SBA, at 500 °C) we obtain the mass ratio of functional organic material to silica, $m_F/m_S = 0.23 \pm 0.02$ (SO₃-SBA) and 0.30 ± 0.02 (Zwi-SBA). These values are consistent with the concentration of functional siloxane chosen in the synthesis: For SO₃-SBA (1 mol% of the silicon atoms added as functional

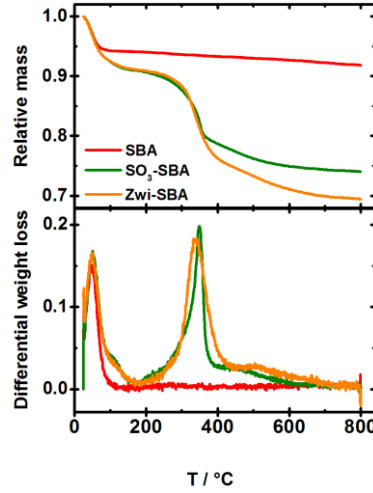


Figure 6.3: TGA and DTA scans of native SBA-15 (SBA), propylsulfonic acid functionalized SBA-15 (SO₃-SBA), and sulfobetaine functionalized SBA-15 (Zwi-SBA).

siloxane) the observed m_F/m_S corresponds to 75% incorporation, for Zwi-SBA (10 mol% of silicon atoms added as functional siloxane) to 86% incorporation of the functional siloxane.

6.3.2 Analysis of Porosity

The data in Table 6.1 form the basis for a determination of the secondary porosity of the SBA-15 materials which is needed in our analysis of the protein adsorption. To derive this relation we focus on a unit cell of the 2D hexagonal pore lattice having unit length in the direction of the channel axis (see Fig. 6.4). The volume of this unit cell (V_{cell}) is made up of the cylindrical pore (V_P), the functional organic layer that surrounds the pore as a cylindrical shell (V_F), and the silica matrix (V_M), that contains the secondary pores. Secondary porosity ε is defined as the volume fraction of pores in the matrix. As explained in the Appendix, it can be calculated from the parameters in Table 6.1 using the relation (Eq. 6.24 in Appendix)

$$\varepsilon = \frac{v_P a \rho_S V_A - (1 + b) V_P}{(v_P a \rho_S + 1) V_A - b V_P} \quad (6.5)$$

where v_P is the total specific pore volume as determined by nitrogen adsorption, ρ_S is the bulk density of silica, $a = 1 + m_F/m_S$, and $b = m_F \rho_S / m_S \rho_F$, where ρ_F represents the density of the organic film at the pore wall. The volumes V_A and V_P in Equation 6.5 are given by $V_A = V_{\text{cell}} - V_P$, with $V_{\text{cell}} = \left(\sqrt{3}/2\right) a_0^2$, and $V_P = (\pi/4) \bar{D}^2$. All quantities except the densities ρ_S and ρ_F can be obtained from Table 6.1. For the evaluation of our data we take $\rho_S = 2.2 \text{ g/cm}^3$ and $\rho_F = 1 \text{ g/cm}^3$. Once the secondary porosity of the sample is known from Equation 6.5, the contributions of the cylindrical and the secondary pores to the total specific pore volume v_P can be calculated as (see Appendix)

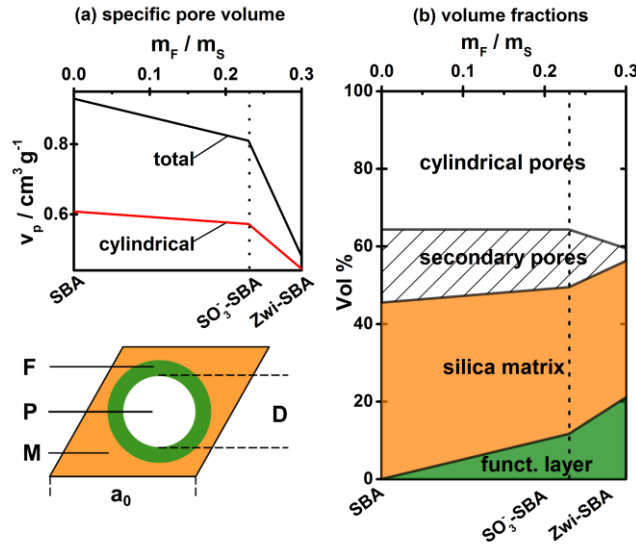


Figure 6.4: Pore structure analysis of the three OMS materials: (a) total specific pore volume v_p and volume of cylindrical pores v_p^{cyl} vs mass ratio m_F/m_S ; (b) volume fraction of cylindrical and secondary pores, functional organic layer, and silica matrix in the three materials vs m_F/m_S . The sketch shows a 2D unit cell of OMS with the cylindrical primary pore (P), the functional organic layer (F), and the silica matrix (M) which contains the secondary pores.

$$v_p^{\text{cyl}} = V_P \frac{1 + b(1 - \varepsilon)}{a\rho_S(1 - \varepsilon)V_A} \quad (6.6)$$

$$v_p^{\text{sec}} = \frac{\varepsilon}{a\rho_S(1 - \varepsilon)} \quad (6.7)$$

and the corresponding specific volumes of silica matrix and functional organic layer are given by $v_S = 1/(a\rho_S(1 - \varepsilon))$, and $v_F = b/a\rho_S$. For native SBA-15 samples, i.e., in the absence of an organic layer, Equations 6.5 – 6.7 apply with $a = 1$ and $b = 0$. The importance of accounting for the secondary porosity of SBA-15 materials is illustrated by the fact that a model without secondary porosity ($\varepsilon = 0$) drastically underestimates the specific pore volume, which in this case is given by $v_p = v_p^{\text{cyl}} = (V_P/\rho_S V_A)$. For our native SBA-15 sample with the parameters a_0 and \bar{D} given in Table 6.1 and $\rho_S = 2.2 \text{ g/cm}^3$, this gives $v_p = 0.36 \text{ cm}^3/\text{g}$, i.e., a value much smaller than the experimental total pore volume ($v_p = 0.93 \text{ cm}^3/\text{g}$). A similar discrepancy is found for SBA-15 samples reported in the literature, including those used by SVC.¹⁴⁹ This implies that the matrix of SBA-15 contains a significant degree of secondary porosity, which affects the overall specific pore volume in two ways: (i) directly, by increasing the pore volume; (ii) indirectly, by decreasing the mass of the matrix.

Results of an analysis of the porosity of our samples on the basis of Equations 6.5 – 6.7 are presented in Figure 6.4. The graph in Figure 6.4a shows the total specific pore volume v_p and the specific volume resulting from the primary cylindrical pores v_p^{cyl} plotted as a function

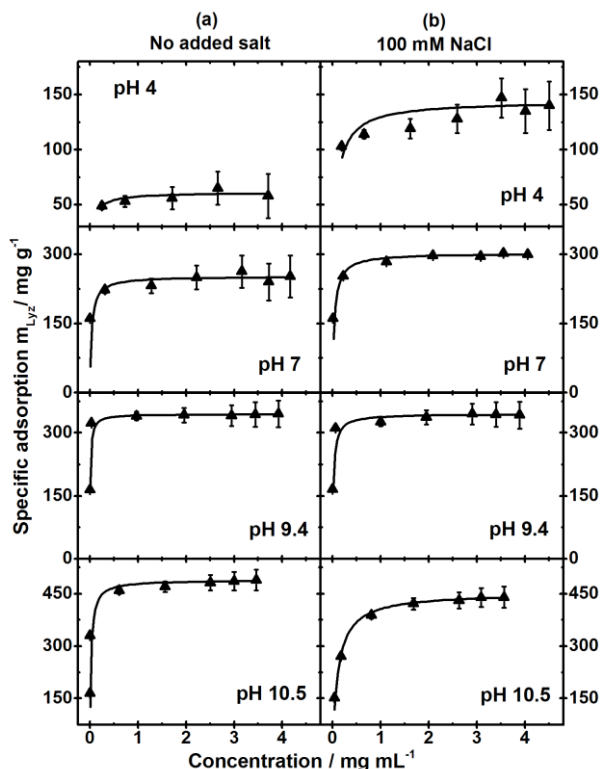


Figure 6.5: Adsorption isotherms of lysozyme in $\text{SO}_3\text{-SBA}$ (20 °C) at pH 4.0, 7.0, 9.4, and 10.5, without added salt (left panels) and in 100 mM NaCl (right panels). The curves represent fits with the Langmuir equation.

of the mass ratio m_F/m_S of the samples. The specific volume of secondary pores (micro- and mesopores) is given by $v_p^{\text{sec}} = v_p - v_p^{\text{cyl}}$. For our native SBA-15 we find that secondary pores make a substantial contribution to the total mesopore volume ($v_p^{\text{cyl}} = 0.61$; $v_p^{\text{sec}} = 0.27$), in agreement with values reported in the literature.^{154–156} In the $\text{SO}_3\text{-SBA}$ sample, secondary pores also make a substantial contribution ($v_p^{\text{cyl}} = 0.57$; $v_p^{\text{sec}} = 0.22$), while for Zwi-SBA the contribution of v_p^{sec} is very small ($v_p^{\text{cyl}} = 0.44$; $v_p^{\text{sec}} = 0.02$). The low secondary porosity of Zwi-SBA conforms with earlier findings¹⁶⁸ that surface-functionalized SBA-15 materials synthesized by the co-condensation route and template removal by solvent extraction exhibit low secondary porosity. The high value of v_p^{sec} found for $\text{SO}_3\text{-SBA}$ is believed to be of a different origin than in the native SBA-15. It can be attributed to the lower degree of structural order of this sample, as manifested by the appearance of a satellite peak in the pore-size distribution (inset in Fig. 6.2b). These somewhat smaller cylindrical pores are believed to constitute a major part of the secondary porosity of this sample. Figure 6.4b characterizes the three OMS materials by showing the relative contributions of cylindrical and secondary pores, organic layer, and silica to the volume of the samples.

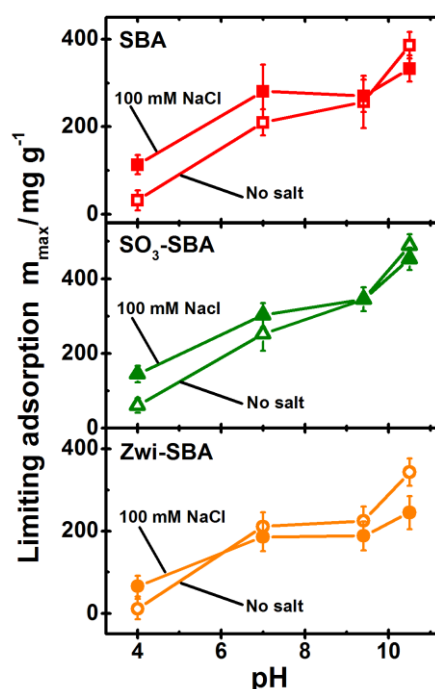


Figure 6.6: Limiting specific adsorption m_{\max} of lysozyme as a function of pH at two ionic strengths (without salt and 100 mM NaCl): native SBA-15 (top); SO₃-SBA (middle); Zwi-SBA (bottom).

6.3.3 Lysozyme Adsorption

Adsorption isotherms of lysozyme in the native and surface-functionalized SBA-15 materials were measured at pH values from 4 to 10.5, without and with added salt (100 mM NaCl). The isotherms for the sulfonic acid modified material are presented in Figure 6.5. The respective results for native and zwitterionized SBA-15 are shown in the Appendix. The adsorption isotherms are of the high-affinity type, reaching a limiting adsorption value at equilibrium concentrations well below 1 mg/mL. Notable exceptions are the isotherms at pH 4 and those at pH 10.5 in the presence of salt. All adsorption isotherms can be represented by the Langmuir equation, from which we extract the parameters limiting adsorption m_{\max} and adsorption equilibrium constant K . The error in m_{\max} is <5% in most cases (up to 10% at pH 4 and pH 10). The error in K is <20% in most cases but up to 100% for the high-affinity isotherms at high pH. Numerical values of m_{\max} and K for the three systems are given in Table 6.5 of the Appendix.

The influence of surface modification on the adsorption affinity of the protein is expressed by the Henry's law adsorption constant $K_H = (\delta\Gamma/\delta c)_{c=0} = K\Gamma_m$, where $\Gamma = m_{\text{lyz}}/a_S$ is the adsorption per unit area and $\Gamma_m = m_{\max}/a_S$ is the limiting adsorption per unit area. K_H is a measure of the interaction of isolated adsorbed protein molecules with the surface. Results for K_H as a function of pH are given in Table 6.2. At pH 4, surface functionalization

with sulfonic acid causes a marked increase of the adsorption affinity K_H of lysozyme relative to native SBA-15, but the enhancement factor $K_H(\text{func})/K_H(\text{nat})$ decreases with increasing pH. Functionalization with zwitterionic sulfobetaine shows an opposite trend, namely an increase of the enhancement factor as pH increases. In all systems the addition of electrolyte causes some increase of the adsorption affinity at low pH, but a pronounced decrease of the affinity at high pH. In the presence of electrolyte the maximum adsorption affinity of lysozyme is not found near its isoelectric point (pH 10.5), but at a lower pH.

The limiting adsorption m_{\max} of lysozyme as a function of pH is presented in Figure 6.6. In all cases m_{\max} strongly increases with pH, reaching high values at pH 10.5. The limiting adsorption is also affected by the addition of salt: At low pH a salt-induced increase of m_{\max} is found, but a salt-induced decrease of m_{\max} is observed at high pH. These trends are parallel to those observed in the adsorption affinity (Table 6.2).

6.3.4 Protein Immobilization Capacity of the Materials

As shown in Figure 6.6 the highest values of the limiting adsorption of lysozyme are found at pH 10.5, i.e., near the IEP of the protein. Hence, the values of m_{\max} at pH 10.5 (without added salt) may be taken as the maximum loading for lysozyme in the three OMS materials. Here we compare these experimental values of m_{\max} with the maximum uptake m_{total} expected on the basis of our porefilling model.

For OMS samples with cylindrical pores of nearly uniform size and a distribution of smaller-sized secondary pores, the expression for the maximum protein uptake in the pore space per gram of OMS (Eq. 6.1) can be written in the form

$$m_{\text{pore}} = C \phi_m(\bar{D}) v_p^{\text{cyl}} + C \int_{\sigma}^{\bar{D}-\vartheta} \phi_m(D) f(D) dD \quad (6.8)$$

Table 6.2: Henry's Law constant K_H (adsorption affinity) of lysozyme adsorption on the three OMS materials at different pH values and two ionic strengths.

sample	$c_{\text{NaCl}}/\text{mM}$	pH 4	pH 7	pH 9.4	pH 10.5
SBA-15	0	0.03	2.0	11	39
SO ₃ -SBA	0	1.5	11	52	32
Zwi-SBA	0	0.02	4.5	61	(260)
SBA-15	100	0.10	6.5	5.9	3.1
SO ₃ -SBA	100	2.0	11	23	6
Zwi-SBA	100	0.03	1.5	26	3.6

with $C = 4M/N_A\pi\sigma^2\delta$, where MW is the molar mass of the protein. The first term on the right-hand side of Equation 6.8 represents m_{cyl} , the specific mass of protein adsorbed in the cylindrical pores of mean diameter \bar{D} . The second term gives m_{max} , the specific mass of protein adsorbed in secondary pores. The integral is taken from a pore size corresponding to the diameter of the protein (σ) to a pore size $\bar{D} - \vartheta$, where ϑ represents the half-width of the distribution of primary cylindrical pore channels. To apply Equation 6.8 to the present OMS materials a normalized distribution function $f(D)$ was derived from the experimental pore size distribution (inset in the panels in Fig. 6.2b) by subtracting a baseline, to account for multilayer adsorption.¹⁵⁰ The baseline was chosen in such a way that the ratio of pore volumes $v_p^{\text{sec}}/v_p^{\text{cyl}}$ extracted from the pore size distribution conforms to the respective ratio given by Equations 6.6 and 6.7. Details of this procedure are explained in Supporting Information.

An analysis of the uptake capacity of the present SBA-15 materials on the basis of Equation 6.8 is given in Table 6.3. For lysozyme ($MW = 14.3 \text{ kg/mol}$), using $\sigma = 3.0 \text{ nm}$, $\delta = 4.5 \text{ nm}$, the prefactor in Equation 6.8 becomes $C = 0.75 \text{ g/cm}^3$. Values of the mean pore size \bar{D} and specific pore volumes (v_p^{cyl} and v_p^{sec}) are taken from Sections 6.3.1 and 6.3.2, and the protein packing function $\phi_m(D)$ is determined by Equations 6.2 – 6.4. The evaluation of Equation 6.8 is exemplified for native SBA-15 and $\text{SO}_3\text{-SBA}$ in Figure 6.7. In both cases the normalized pore size distribution function $f(D)$ exhibits a sharp peak representing the primary pore channels (pore sizes $\bar{D} \pm \vartheta$, with $\vartheta \approx 0.5 \text{ nm}$) and a distribution of smaller secondary pores. Since the protein packing function $\phi_m(D)$ for lysozyme ($\sigma = 3 \text{ nm}$) is nearly constant in the size range of the primary pores, this part of the integral can be replaced by $\phi_m(\bar{D})v_p^{\text{cyl}}$ as in Equation 6.8. The protein uptake in secondary pores is evaluated by numerical integration. Resulting values of m_{cyl} , m_{sec} , and the total uptake capacity of pores, m_{pore} , are given in Table 6.3.

The amount of protein adsorbed at the outer surface of OMS particles depends on the size and shape of the particles and can be estimated only in an approximate way. For elongated cylindrical particles the amount adsorbed at the outer surface is related to the amount adsorbed inside the pore channels approximately by¹⁴⁹

Table 6.3: Uptake Capacity of OMS Materials for Lysozyme ($\sigma = 3 \text{ nm}$) Estimated by Equations 6.8 and 6.9 and Comparison of the Total Uptake Capacity with the Prediction of the SVC Model.)*

sample	cylindrical		secondary		m_{pore}	m_{ext}	m_{total}	m_{SVC}
	v_p^{cyl}	m_{cyl}	v_p^{sec}	m_{sec}				
SBA-15	0.61	314	0.32	96	410	39	449	517
$\text{SO}_3\text{-SBA}$	0.57	295	0.24	95	390	106	496	521
Zwi-SBA	0.44	225	0.04	10	235	25	260	271

)* Specific pore volumes in $\text{cm}^3/(\text{g OMS})$; specific protein uptake in $\text{mg}/(\text{g OMS})$.

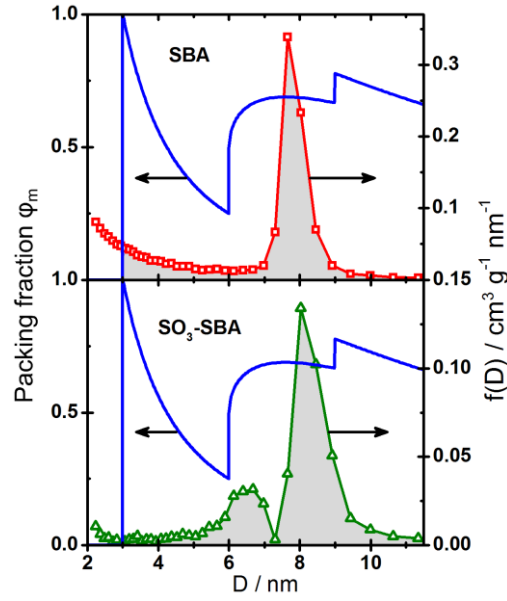


Figure 6.7: Determination of the protein uptake capacity from the normalized pore size distribution $f(D)$ and the protein packing fraction function $\phi_m(D)$ for lysozyme in native SBA-15 (upper graph); SO_3 -SBA (lower graph). The parts of $f(D)$ which contribute to the protein uptake are color-coded.

$$\frac{m_{\text{ext}}}{m_{\text{pore}}} = \left(\frac{a_0}{D_{\text{part}}} \right)^2 \frac{N_{\text{ext}}}{N_1} \quad (6.9)$$

where D_{part} is the mean particle diameter (see Table 6.1) and N_{ext} is the number of protein molecules that can be accommodated along the external perimeter of the cylindrical particles. It can be estimated as¹⁴⁹ $N_{\text{ext}} = \pi [\arcsin(\sigma/(D_{\text{part}} + \sigma))]^{-1}$. According to Equation 6.9, m_{ext} depends strongly on the mean particle diameter, and its contribution to the total protein uptake becomes important for $D_{\text{part}} < 200$ nm. Values of m_{ext} estimated by Equation 6.9 (with m_{pore} given by the SVC model) are included in Table 6.3. The error in m_{ext} (resulting mostly from the uncertainty in D_{part}) is estimated to be <20% for native SBA-15 and Zwi-SBA, and <40% for SO_3 -SBA. For this latter sample the uncertainty in the estimated total uptake $m_{\text{total}} = m_{\text{pore}} + m_{\text{ext}}$ is dominated by the uncertainty of m_{ext} .

Values of m_{total} estimated by Equation 6.8 and 6.9 are given in Table 6.3 and compared with the respective values obtained by the SVC model, in which the uptake in the pores is estimated as $m_{\text{pore}} = C\phi_m(\bar{D})v_p$. Figure 6.8 compares the predicted uptake capacity with the experimental limiting uptake of lysozyme in the three OMS materials at pH 10.5. The uptake capacity estimated by the SVC model is also shown for comparison.

6.4 Discussion

6.4.1 Protein Uptake Capacity

Figure 6.8 shows that the new model gives lower values of the protein uptake than the SVC model, providing a better prediction of the experimental maximum uptake of lysozyme in the OMS materials. For native SBA-15, where the uncertainty in m_{total} caused by adsorption at the external surface is small ($<1\%$), the value of m_{total} estimated by Equations 6.8 and 6.9 is still about 15% higher than the experimental maximum uptake. This may be due to an overestimate of the protein uptake in secondary pores as a result of using an incorrect normalization of the PSD (cf. Fig. 6.7a and Appendix). The SVC model overestimates the uptake capacity of native SBA-15 by more than 30%, as it assumes that the total pore volume is fully accessible to the protein. For SO_3 -SBA the new model predicts the experimental maximum uptake very well. The contribution of m_{sec} to the total uptake is again rather high (Table 6.3). Figure 6.7b shows that in this case most of the secondary porosity comes from the satellite peak in the pore size distribution and a significant part of these pores have diameters $D > 2 \sigma$ and allow for a high protein packing fraction. Accordingly, the SVC model gives a better prediction of the uptake capacity of this sample than for native SBA-15 (Fig. 6.8). For Zwi-SBA the experimental maximum uptake m_{max} in the presence of salt (100 mM) agrees with the predicted total uptake capacity m_{total} , but the value of m_{max} in the absence of salt is significantly higher (Fig. 6.8). This disagreement might be due to an error in the experimental pore volume of Zwi-SBA (cf. Table 6.1) and thus to a wrong prediction of m_{total} . More likely, the disagreement is caused by errors in the experimental adsorption isotherm at pH 10.5 in the absence of salt (see Fig. 6.11 in the Appendix) which also lead to an exceedingly high value of K_H (see Table 6.2). Unfortunately, we could not resolve this question by repeat measurements due to a lack of sample material.

The analysis presented above confirms the widely accepted view that native SBA-15 materials prepared by the classical protocol,¹⁸ and using calcination for template removal, contain a high level of wall porosity.^{150,154–156} Since a large part of these pores are too small for the protein to enter, the SVC model overestimates the uptake capacity of classical SBA-15 materials. In the work of SVC,¹⁴⁹ materials of mean pore diameter from 7.6 to 15 nm were obtained by microwave-assisted hydro-thermal aging at temperatures from 100 to 240 °C. It is well-known that aging at high temperatures (>100 °C) leads not only to an increase in size of the primary pores of SBA-15, but also to the disappearance of microporosity and formation of secondary pores bridging the primary pores, so that the materials transform to a 3D mesopore system.¹⁶⁹ The temperature-induced transformation of narrow to wider secondary pores

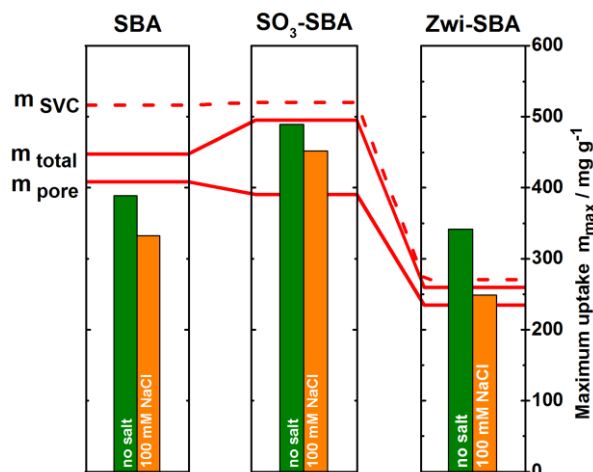


Figure 6.8: Comparison of the experimental maximum uptake of lysozyme by the three OMS materials (pH 10.5 without salt, and with 100 mM NaCl, indicated by the pair of columns) with the estimated uptake capacity of the pore space (m_{pore}) and total uptake capacity ($m_{\text{total}} = m_{\text{pore}} + m_{\text{ext}}$) of the samples (indicated by horizontal bars). The dashed line indicates the total uptake capacity estimated by the SVC model.

explains why the lysozyme uptake in these samples was found to conform to the original SVC model.¹⁴⁹

Our functionalized SBA-15 materials both have a very low micropore volume, possibly due to incomplete removal of PEO chains of the template which protrude into the pore walls.^{150,169} The structurally well-ordered Zwi-SBA also has a very low level of secondary mesoporosity, so that the protein uptake capacity is determined almost solely by the volume of cylindrical pores, as in the SVC model. The structurally less ordered SO₃-SBA material contains a high proportion of disordered pores in a size range in which the protein molecules can pack nearly as well as in the main cylindrical channels (see Fig. 6.7). Accordingly, the protein uptake capacity estimated by the new model is again not much lower than the SVC value (see Table 6.3). These results suggest that the SVC model might be better applicable to functionalized SBA-15 rather than standard native SBA-15 materials, but further work is needed to confirm this conjecture.

6.4.2 Influence of Surface Functionalization

Table 6.2 shows that surface functionalization with sulfonic acid increases the adsorption affinity K_{H} of lysozyme at low pH, when lysozyme molecules are highly charged,^{31,159} while the bare silica surface is nearly uncharged.⁴⁵ Presumably, this is due to the higher negative surface charge density of SO₃-SBA relative to the native silica surface at this low pH. This view is supported by the observed decrease of the enhancement factor $K_{\text{H}}(\text{funct})/K_{\text{H}}(\text{nat})$ with increasing pH, as the surface charge density of the bare silica surface becomes similar to (or even higher than) the SO₃-functionalized surface. Functionalization with zwitterionic sulfobetain has little influence on the adsorption affinity of lysozyme at low pH, but causes an

enhancement of K_H at higher pH. This indicates that the mechanisms of antifouling action of zwitterionic groups¹⁶⁶ are not effective in strongly confined geometries. Further work is needed to better understand this interesting finding. The observation that the adsorption affinity K_H decreases when the ionic strength is increased to 100 mM (Table 6.2) is expected for the ion exchange mechanism of protein adsorption at charged surfaces.¹⁷⁰ This trend is also observed with Zwi-SBA (though to a lesser extent than with the other substrates), which indicates a relatively low zwitterion efficiency of Zwi-SBA.¹⁶⁶

6.5 Conclusion

This study has shown that the porefilling model introduced in Section 6.2 can form a rational basis for assessing the protein immobilization capacity of native and surface-functionalized OMS materials. Whereas in earlier studies of protein immobilization it was assumed that the entire pore volume v_p is made up of cylindrical pores of uniform size, the new model makes a distinction between the volume of primary cylindrical pores (v_p^{cyl}) and the pore volume due to secondary porosity (v_p^{sec}), which may or may not be accessible to the protein, depending on the pore size distribution. We propose a procedure to normalize the experimental pore size distribution in such a way that the ratio (v_p^{sec}/v_p^{cyl}) determined from the pore size distribution is consistent with the values of v_p^{cyl} and v_p^{sec} determined independently from the total specific pore volume (v_p), the diameter of the cylindrical pores (\bar{D}), the lattice constant of the pore lattice (a_0), and the mass ratio of the organic functional layer and silica matrix (m_F/m_S). In Section 6.3.4 it is shown that the amount of protein immobilized in the pores can be estimated from the normalized pore size distribution $f(D)$ of the OMS and the packing fraction function $\phi_m(D)$ of the protein. The new model gives an improved prediction of the uptake capacity for lysozyme in native SBA-15 by accounting for the uptake capacity of the secondary pores in a realistic manner. For the two functionalized materials the prediction of the uptake capacity by the two models is nearly equally good. This can be rationalized by the fact that for one of them (Zwi-SBA) the secondary pore volume is very small, while for the other material (SO₃-SBA) the secondary pore volume is made up mostly of pores in which the protein can pack nearly as well as in the primary pores. Finally, we stress that the new model can be applied not only to OMS materials, but also to the protein uptake in any mesoporous material, if the pore size distribution of the material is known.

6.6 Appendix

6.6.1 Preparation of Mesoporous Materials

Chemicals: Pluronic P-123 ($\text{EO}_{20}\text{PO}_{70}\text{EO}_{20}$ triblockcopolymer), (3-mercaptopropyl)-trimethoxysilane (MPTMS), (N,N-dimethyl-3-aminopropyl)trimethoxysilane, propane sultone, hydrogen peroxide (35wt%), hydrochloric acid (analytical grade), sodium hydroxide ($\geq 98\%$), NaCl ($\geq 98\%$), all from Sigma-Aldrich, and tetraethoxysilane (TEOS) from ABCR ($\geq 98\%$) were used in the synthesis of the OMS materials or the protein adsorption measurements. Milli-Q water from MilliPore QPAC was used for all the experiments.

Native SBA-15 was prepared by the method reported by Zhao et al.,¹⁸ using Pluronic P123 as the template and TEOS as the silica precursor. The precipitated composite material was aged at 95 °C for 24 h and calcined in air at 500 °C for 6 h.

Sulfonic-acid functionalized SBA-15 ($\text{SO}_3\text{-SBA}$) was prepared by co-condensation of the silica precursor with the thiol-precursor MPTMS, as reported by Margolese et al.¹⁹ The molar composition for 4 g of copolymer was 0.0348TEOS : 0.0062MPTMS : 0.0123 H_2O_2 : 0.24HCl : 6.7 H_2O , so that 15 % of the silicon atoms were present in form of the thiol precursor. A TEOS prehydrolysis time of 45 min prior to the addition of MPTMS and H_2O_2 was chosen. According to this protocol,¹⁹ quantitative conversion of the thiol to sulfonate groups is achieved when the oxidant H_2O_2 is added simultaneously with MPTMS. The reaction mixture was stirred for 20 h at 40°C and aged for 24 h at 100°C without stirring. The white precipitate was collected, washed with Milli-Q water and dried at room temperature. The template was then removed by extraction with ethanol (24 h under reflux).

Zwitterion-functionalized SBA-15 (Zwi-SBA) was prepared by a similar protocol as $\text{SO}_3\text{-SBA}$, using 3-(dimethyl(3-(trimethoxysilyl)propyl)-ammonio)propane-1-sulfonate (abbreviated SBS) as the sulfobetain precursor.^{170,171} 4 g of Pluronic P123 was dissolved in 125 g of 1.9 M hydrochloric acid. After equilibration at 40 °C, 7.26 g TEOS were added and prehydrolyzed under stirring at 40°C for 45 min. 1.21 g of SBS was then added. The molar composition for 4 g of copolymer was 0.0348TEOS : 0.0037SBS : 0.24HCl : 6.7 H_2O , so that 10% of the silicon atoms were present in form of the sulfobetaine precursor. The reaction mixture was stirred for 20 h at 40 °C and aged for 24 h at 100 °C without stirring. The white precipitate was collected and treated as in the case of the sulfonic acid functionalized material. The **sulfobetaine precursor (SBS)** was synthesized as described by Litt et al.¹⁷¹ A solution of 2.23 g of 1,3-propane sultone in 18 mL of dried acetone was prepared and 3.75 g of N,N-dimethyl-amino-propyl-trimethoxysilane were added in a dry nitrogen atmosphere. The reaction mixture was stirred at 20 °C for 5 h. The resulting white precipitate was collected and

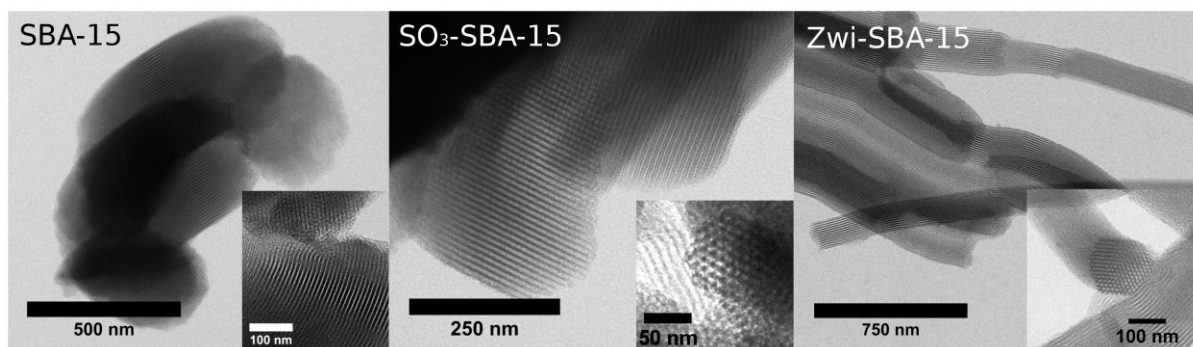


Figure 6.9: TEM images of the three OMS materials: (a) native SBA-15; (b) SO_3 -SBA; (c) Zwi-SBA.

washed with acetone, dried and stored in a desiccator under vacuum. Reaction yield was 81%. The product was characterized by ^1H NMR.

6.6.2 Sample Characterization Methods

Transmission electron microscopy (TEM). Images were obtained with a JEM-2100 instrument (JEOL) operating at 200 kV. Cu grids with a carbon film (thickness 20-10 nm, 200 mesh) were used. The images were processed using the ImageJ software.¹⁷²

Powder XRD with a SAXSess mc² instrument (Anton Paar) was used to record small-angle powder XRD profiles of the OMS materials. The instrument was equipped with a slit collimated Cu K_α X-ray source (0.1542 nm) operated at 40 kV (50 mA). The powder samples were held in the beam path with adhesive tape. The software package Saxsquant 3.50 was used for data reduction.

Nitrogen adsorption isotherms at 77 K were determined on a Gemini III 2375 volumetric surface analyser (Micromeritics). The samples were outgassed at 120 °C for 1h before the measurement and reweighed in air at ambient humidity conditions afterwards (sample weight m_w). The specific surface area and pore volume of the samples was calculated on the basis of m_w by applying a correction for the water content based on the TGA measurements.

In the analysis of the nitrogen adsorption isotherms the mean diameter of the primary pores was determined from the inflection point of the pore condensation step by the generalized KJS relation¹⁷³ which (unlike the NLDFT method) is applicable to the functionalized as well as the native SBA-15 materials. The single-point total pore volume v_p was determined by extrapolation of the linear region in the adsorption isotherm above pore condensation to $p/p_0 = 0$. The micropore volume $v_{p,\text{micro}}$ was determined by the t -plot method.

Thermogravimetric analysis (TGA) of the OMS materials was done using a TGA1 STARe system (MettlerToledo). The heating rate was 10 K/min in the temperature range from 25 to 800 °C.

Analysis of TG scan:

$$m_W = m_{H_2O} + m_F + m_S = 1 \quad (6.10)$$

$$m_0 = m_F + m_S$$

where

m_W = unit mass of sample equilibrated in the lab atmosphere

m_{H_2O} = relative mass of adsorbed water vapor

m_F = relative mass of functional organic layer

m_S = relative mass of silica

Table 6.4: Analysis of TGA data^{a)}

sample	$\frac{M_F}{\text{g/mol}}$	$\frac{m_{H_2O}}{m_{\text{sample}}}$	$\frac{m_F}{m_0}$	$\frac{m_F}{m_S}$	$\frac{n_F/m_s}{\text{mmol/g}}$	$\frac{n_F/a_s}{\mu\text{mol/m}^2}$
SBA-15	-	0.05	0	0	0	0
SO ₃ -SBA	123.15	0.09	0.17	0.23	1.9	2.9
Zwi-SBA	209.3	0.09	0.21	0.30	1.4	4.2

^{a)} M_F , molar mass of functional organic group; m_0 , mass of dry sample; m_F , mass of functional organic group; n_F , amount of functional organic groups; a_s specific surface area of the sample.

6.6.3 Calculation of Matrix Porosity

In this section we derive expressions for the specific pore volumes contributed by the ordered cylindrical pore channels and the disordered secondary pores embedded in the matrix of SBA-15. (Eq. 6.2 and 6.3). We consider a unit cell of the 2D hexagonal lattice (see Fig. 6.3). The total volume per unit length of the pore (V_{cell}) is made up of the cylindrical pore (V_P), the functional organic layer that surrounds the pore as a cylindrical shell (V_F), and the silica matrix (V_M),

$$V_{\text{cell}} = V_P + V_F + V_M \quad (6.11)$$

with

$$V_{\text{cell}} = \frac{\sqrt{3}}{2} a_0^2 \quad (6.12)$$

$$V_P = \frac{\pi}{4} \bar{D}^2 \quad (6.13)$$

In the equations below we also use the volume difference

$$V_A \equiv V_{\text{cell}} - V_P = \frac{\sqrt{3}}{2} a_0^2 - \frac{\pi}{4} \bar{D}^2 \quad (6.14)$$

Note that the symbol V represents volumes per unit pore length (i.e., areas). The subscripts P, F, and M refer to the space occupied by the cylindrical pore, the functional layer and the matrix. The quantities a_0 and \bar{D} represent the lattice parameter and the mean pore diameter as defined in Figure 6.3.

Native SBA-15. For native (unfunctionalized) SBA-15 silica ($V_F = 0$) without any secondary porosity (“ideal SBA-15”) the mass of a unit cell per unit pore length is given by $M_M = \rho_S V_M = \rho_S (V_{\text{cell}} - V_P)$, where ρ_S is the bulk density of silica. The specific pore volume (i.e., volume per unit mass) of such an ideal sample is

$$v_p^{\text{id}} = \frac{V_P}{M_M} = \frac{V_P}{\rho_S V_A} \quad (6.15)$$

For our native SBA-15 material, with the parameters given in Table 6.1 ($a_0 = 11.1$ nm, $\bar{D} = 7.7$ nm) and the density of nonporous silica ($\rho_S = 2.2$ g/cm³), this gives $v_p^{\text{id}} = 0.36$ cm³/g, i.e. drastically smaller than the experimental total specific pore volume of this sample ($v_p = 0.93$ cm³/g). Such a large deviation is typical for SBA-15 materials when the template was removed by calcinations. It implies that in addition to the ordered cylindrical pores the material must contain pores distributed in the matrix in a random manner. The secondary porosity ε is defined as the fraction of matrix volume taken up by these secondary pores. Below we show how ε can be calculated from the parameters a_0 , \bar{D} , and the specific pore volume of the sample, v_p , again with the density of nonporous silica as an additional input parameter.

When a fraction ε of the silica matrix is taken up by secondary pores, then the mass per unit cell is $M_M = \rho_S (1 - \varepsilon) V_M$ and the specific volume of cylindrical pores becomes

$$v_p^{\text{cyl}} = \frac{V_P}{\rho_S (1 - \varepsilon) V_A} \quad (6.16)$$

which is larger by a factor $1/(1 - \varepsilon)$ than v_p^{id} (Eq. 6.15). In addition, the secondary porosity contributes a volume $\varepsilon V_M = \varepsilon (V_{\text{cell}} - V_P)$ per unit cell, i.e., a specific pore volume

$$v_p^{\text{sec}} = \frac{\varepsilon V_A}{\rho_S (1 - \varepsilon) V_A} = \frac{\varepsilon}{\rho_S (1 - \varepsilon)} \quad (6.17)$$

The total specific pore volume then becomes

$$v_p = v_p^{\text{cyl}} + v_p^{\text{sec}} \quad (6.18)$$

When the quantities a_0 , \bar{D} , v_p , and ρ_S are known, the secondary porosity ε can be calculated from Equations 6.15 – 6.17

$$\varepsilon = \frac{v_p \rho_S V_A - V_P}{(v_p \rho_S + 1) V_A} \quad (6.19)$$

with V_P and V_A given by Equations 6.13 and 6.14. The resulting value of ε can be used to determine v_p^{cyl} and v_p^{sec} by Equations 6.16 and 6.17.

Functionalized SBA-15. The formalism outlined above can be applied to SBA-15 materials functionalized by an organic layer which forms a cylindrical shell around the pores of mean diameter \bar{D} (see Fig. 6.3). The unit cell volume V_{cell} is made up of the volumes V_P , V_F , and V_M (Eq. 6.11) and the expressions for V_{cell} , V_P , and V_A (Eq. 6.12 – 6.14) still apply. V_F is related to the volume of silica matrix V_M via the mass ratio of organic film and silica, m_F/m_S , and the respective ratio of mass densities, ρ_F/ρ_S ,

$$V_F = \frac{M_F}{\rho_F} = \frac{1}{\rho_F} \frac{m_F}{m_S} M_M = \frac{1}{\rho_F} \frac{m_F}{m_S} \rho_S (1 - \varepsilon) V_M = b(1 - \varepsilon) V_M \quad (6.20)$$

where $b = \rho_S m_F / \rho_F m_S$. From Equation 6.20, and $V_A = V_M + V_F$, we obtain

$$V_M = \frac{V_A}{1 + b(1 - \varepsilon)} \quad (6.21)$$

The mass per unit cell is now given by the contributions of the silica matrix and the organic layer as

$$\begin{aligned} M_{\text{cell}} &= M_M + M_F = \left(1 + \frac{m_F}{m_S}\right) M_M = \left(1 + \frac{m_F}{m_S}\right) \rho_S (1 - \varepsilon) V_M \\ &= \frac{a \rho_S (1 - \varepsilon) V_A}{1 + b(1 - \varepsilon)} \end{aligned} \quad (6.22)$$

where $a = 1 + m_F/m_S$. As earlier, the specific pore volume is obtained by referring the volume per unit cell to the mass per unit cell. By analogy with Equation 6.15 we thus obtain

$$v_p = \frac{V_P + \varepsilon V_M}{M_M} = \frac{V_P [1 + b(1 - \varepsilon)] + \varepsilon V_A}{a \rho_S (1 - \varepsilon) V_A} \quad (6.23)$$

This relation can again be used to calculate the secondary porosity ε , for which we find

$$\varepsilon = \frac{v_p a \rho_s V_A - (1 + b) V_P}{(v_p a \rho_s + 1) V_A - b V_P} \quad (6.24)$$

Finally, the specific volumes of ordered cylindrical pores, secondary pores and the functional organic layer become

$$v_p^{\text{cyl}} = \frac{V_P}{M_M} = V_P \frac{1 + b(1 - \varepsilon)}{a \rho_s (1 - \varepsilon) V_A} \quad (6.25)$$

$$v_p^{\text{sec}} = \frac{\varepsilon V_M}{M_M} = \frac{\varepsilon}{a \rho_s (1 - \varepsilon)} \quad (6.26)$$

$$v_F = \frac{V_F}{M_M} = \frac{b}{a \rho_s} \quad (6.27)$$

$$v_M = \frac{V_M}{M_M} = \frac{1}{a \rho_s (1 - \varepsilon)} \quad (6.28)$$

The volumes v_p^{cyl} , v_p^{sec} , v_F , and v_M add up to the total volume per unit mass of the sample. By normalization to this specific sample volume we obtain the corresponding volume fractions of cylindrical and secondary pores, functional organic layer and silica matrix, which are shown in graphical form in Figure 6.3.

6.6.4 Normalized Pore Size Distribution Function

To estimate the protein uptake capacity by Equation 6.8, we need to determine the normalized pore size distribution $f(D)$ of the OMS materials. Starting from the pore size distribution (PSD) as obtained by nitrogen adsorption, the determination of $f(D)$ involves two steps: (1) Setting the borderline between primary cylindrical pores and secondary pores at a pore size $\bar{D} - \vartheta$, where \bar{D} is the mean pore diameter of the cylindrical pores and ϑ the half width of the main peak in the psd.¹⁹ And (2) applying a correction to the PSD to account for multilayer adsorption of nitrogen in the primary pore channels and at the external surface of the particles.¹⁵⁰ This is achieved by subtracting a baseline from the experimental PSD. This baseline is higher at pore diameters $D < \bar{D}$ than at $D > \bar{D}$, because multilayer adsorption in the primary pores contributes only at $D < \bar{D}$. The position of the baseline in this regime was determined using the criterion that the ratio of secondary to primary pore volume determined by integration of the two regimes

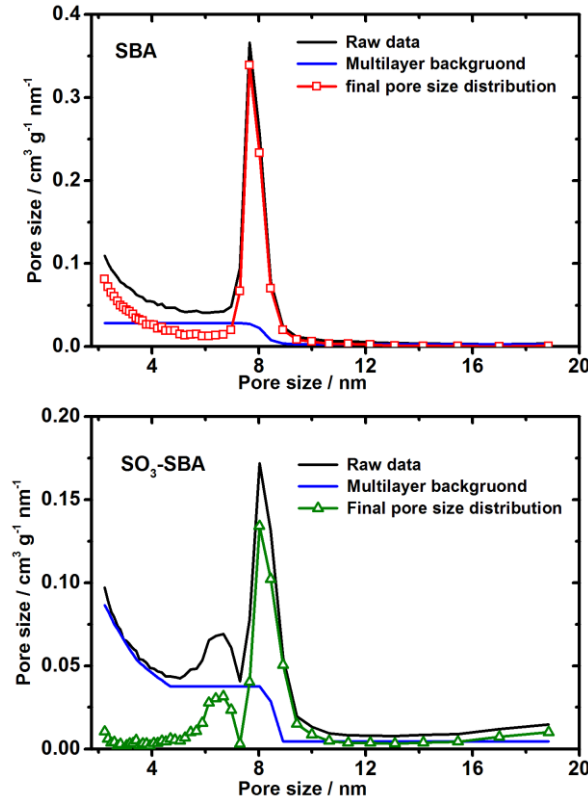


Figure 6.10: Determination of the normalized pore size distribution function $f(D)$ by subtraction of a background from the PSD raw data (see text): (a) native SBA-15; (b) SO_3 -SBA.

of the normalized PSD must be equal to $v_p^{\text{sec}}/v_p^{\text{cyl}}$ as determined by Equations 6.25 and 6.26. Since v_p^{sec} represents the total secondary pore volume (including micropores) while the experimental PSD covers only the mesopore range ($D > 2$ nm) a correction to include the micropore volume was applied as follows: Using the symbols V^{cyl} and $V_{\text{meso}}^{\text{sec}}$ for the volume of cylindrical and secondary pores resulting from the integration of the normalized PSD in the mesopore range, and $V_{\text{meso}} = V^{\text{cyl}} + V_{\text{meso}}^{\text{sec}}$ for the respective overall mesopore volume, the corresponding total pore volume (including micropores), V_{total} , is estimated from the experimental specific pore volume v_p and the specific mesopore volume of the sample, $v_{p,\text{meso}} = v_p - v_{p,\text{micro}}$, as

$$V_{\text{total}} = \frac{v_p}{v_{p,\text{meso}}} V_{\text{meso}} \quad (6.29)$$

and the overall secondary pore volume (including micropores) is

$$V^{\text{sec}} = V_{\text{total}} - V^{\text{cyl}} \quad (6.30)$$

Hence the criterion for the baseline of the PSD at $D < \bar{D}$ is

$$\frac{V^{\text{sec}}}{V^{\text{cyl}}} = \frac{v_p^{\text{sec}}}{v_p^{\text{cyl}}} \quad (6.31)$$

Figure 6.10 illustrates the baseline correction of the PSD for native SBA-15 and SO₃-SBA. In the case of native SBA-15 the procedure outlined above can be applied in a straightforward way. For the less well-ordered sample of SO₃-SBA it was not possible to meet the criterion of Equation 6.31 with a constant baseline, as this always leads to a ratio $V^{\text{sec}}/V^{\text{cyl}}$ greater than the experimental value. In order to meet the criterion of Equation 6.31 for this system it had to be assumed that the baseline increases toward the lower limit of the mesopore range. This leads to a low level of pore sizes near the lower limit of the mesopore range, which is in line with the low micropore volume of this sample (see Fig. 6.4b). Since for lysozyme only pores of diameter >3 nm are accessible, the pore size distribution of smaller pores is of no relevance. Nevertheless, a reliable determination of the normalized PSD remains a challenge for future work.

6.6.5 Protein Adsorption Measurements

Lysozyme from chicken egg white (lyophilized powder, protein ≥90%, ≥40.000 units/mg protein) was received from Sigma-Aldrich (lot 061M1329 V) and stored at −30 °C. Adsorption isotherms of lysozyme onto the OMS materials were determined in unbuffered solutions at controlled pH in the absence and presence of salt (100 mM NaCl). For each set of experiments, stock solutions of lysozyme (10 mg/mL), NaCl (300 mM), and OMS (20 mg/mL) were freshly prepared in water at the desired pH by addition of known aliquots of HCl or NaOH. Samples with 1.5–15 mg protein were prepared from the protein and salt stocks, and 0.5 mL of the stirred OMS stock was added to reach the sample volume of 3 mL. The samples were equilibrated at 20 °C for 20 h in a closed vial, using a Thermomixer. After readjustment of the pH the silica was separated from the supernatant by centrifugation at 15.000 rpm for 45 min, and the residual concentration of protein in the supernatant was determined by UV-vis spectrometry. The spectra of the samples were compared with a concentration standard at several wavelengths in the 265–300 nm range, and the concentration was obtained by minimizing the variance of the deviations from this concentration standard. The amount of adsorbed protein was calculated by a mass balance. A correction for adsorbed water was applied to the weight m_0 of all samples equilibrated in the laboratory atmosphere, on the basis of the water weight loss of the three materials found by TGA. In preliminary experiments it was found that the adsorption equilibrium of lysozyme in the OMS materials was established on a time scale of a few hours, even at a pH near the IEP. Hence, the lysozyme uptake after 20 h was taken as the equilibrium adsorbed amount.

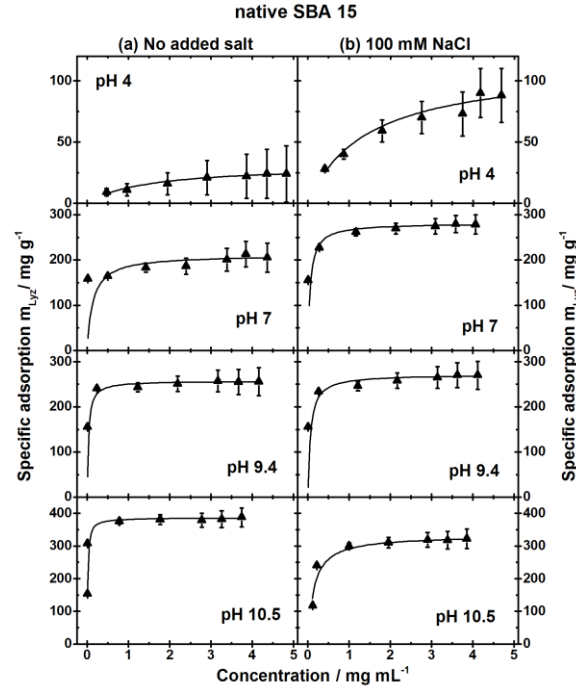


Figure 6.11: Adsorption isotherms of lysozyme in native SBA-15 at four different pH values in the absence of salt (left panels) and with 100 mM NaCl (right panels).

6.6.6 Adsorption Data and Langmuir Fits for Lysozyme in the OMS Materials

Adsorption isotherms for lysozyme in native SBA-15 and Zwi-SBA-15 at pH from 4 to 10.5 in the absence and presence of salt are shown in Figure 6.11 and 6.12.

The adsorption data can be represented within experimental error limits by the Langmuir equation,

$$m_{\text{Lyz}} = m_{\text{max}} \frac{Kc}{1 + Kc} \quad (6.32)$$

where m_{Lyz} is the mass of adsorbed lysozyme per unit mass of the sample, and c is the equilibrium concentration of protein in the supernatant solution. The parameters m_{max} (limiting adsorption per unit mass) and K (Langmuir adsorption constant) were determined from the Langmuir equation in the form

$$\frac{c}{m_{\text{Lyz}}} = \frac{1}{m_{\text{max}}K} + \frac{c}{m_{\text{max}}} \quad (6.33)$$

The resulting values of the parameters m_{max} and K are given in Table 6.5. The adsorption affinity (Henry's law adsorption constant K_H) represents the initial slope of the adsorption isotherm and is related to these parameters as $K_H = Km_{\text{max}}$.

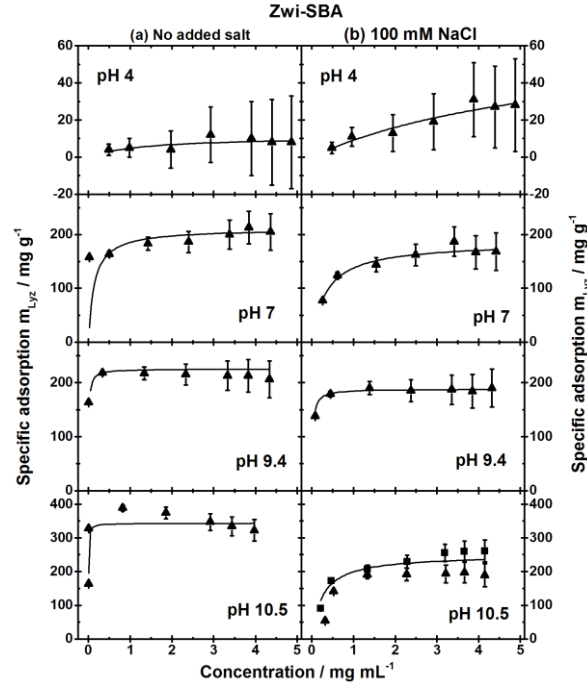


Figure 6.12: Adsorption isotherms of lysozyme in Zwi-SBA-15 at four different pH values in the absence of salt (left panels) and with 100 mM NaCl (right panels).

6.6.7 Protein pore filling model

To relate the protein uptake into OMS to the specific pore volume of the sample we generalize the geometric model of Sang, Vinu and Coppens (SVC)¹⁴⁹ to the situation of materials having a distribution of pore sizes. In the SVC model the maximum amount of protein that can be accommodated in pores of cross-sectional area $A_p = (\pi/4)D^2$ is given by

$$n_{\max} = \frac{N}{N_A A_p \delta_{\text{prot}}} v_p \quad (6.34)$$

where N is the number of molecules that can be accommodated side-by-side in a cross-section of the pore, N_A is the Avogadro constant, δ_{prot} is the longest dimension of a protein molecule, and v_p is the specific pore volume of the sample. In Equation 6.34 the factor $N/A_p \delta$ represents the number of protein molecules in a volume element of length δ_{prot} of the pore. The volume fraction of protein in this element is then

$$\varphi_m = \frac{N v_{\text{prot}}}{(\pi/4) D^2 \delta_{\text{prot}}} \quad (6.35)$$

where v_{prot} is the volume of a protein molecule. Equation 6.35 is strictly a 2D model of protein packing without consideration of packing effects in the direction of the pore axis. Elongated protein molecules are treated as cylinders of diameter σ and length δ_{prot} , so that $v_{\text{prot}} = (\pi/4)\sigma^2\delta$. Inserting this into Equation 6.35 and combining with 6.34 gives

$$n_{\text{max}} = \frac{4}{N_A \pi \sigma^2 \delta_{\text{prot}}} \varphi_m v_p \quad (6.36)$$

with

$$\varphi_m = \frac{N}{(D/\sigma)^2} \quad (6.37)$$

For a sample containing cylindrical pores of different diameters \bar{D} , Equation 6.36 can be generalized by introducing the pore size distribution function $f(D) = (dv_p/dD)_D$

$$n_{\text{max}} = \frac{4}{N_A \pi \sigma^2 \delta_{\text{prot}}} \int \varphi_m(D) f(D) dD \quad (6.38)$$

where the integral extends over the relevant pore sizes.

Table 6.5: Langmuir parameters for lysozyme adsorbed in the OMS materials at four different pH values without added salt and in 100 mM NaCl.

System	pH	without salt		100 mM NaCl	
		$\frac{m_{\text{max}}}{\text{mg/g}}$	$\frac{K}{\text{mL/mg}}$	$\frac{m_{\text{max}}}{\text{mg/g}}$	$\frac{K}{\text{mL/mg}}$
SBA-15	4.0	31	0.70	113	0.70
	7.0	210	7.4	281	18
	9.4	257	35	272	17
	10.5	386	78	333	7.2
SO ₃ -SBA	4.0	61	16	145*	9.0*
	7.0	252	29	303	25
	9.4	345	100	345	45
	10.5	489	43	453	8.7
Zwi-SBA	4.0	11	0.77	66	0.16
	7.0	211	7.4	186	2.9
	9.4	225	93	188	48
	10.5	343	265	249	5.0

* Values for 50 mM NaCl

Pore size dependence of the protein packing factor ϕ_m . In the approximation underlying the SVC model¹⁵⁰ the determination of N as a function of the reduced pore diameter D/σ (Eq. 6.37) becomes equivalent to calculating the number of circular objects (diameter σ) that can be arranged in a series of non-overlapping concentric rings ('layers') of width σ and outer diameter $d_n = D - 2(n - 1)\sigma$. Treating the number of objects N_n in layer n as a continuous variable it becomes

$$N_n = \pi \left(\arcsin \frac{\sigma}{d_n - \sigma} \right)^{-1} \quad (6.39)$$

For the outermost layer ($n = 1$), d_1 represents the pore diameter D . A second layer ($n = 2$) with $d_2 = D - 2\sigma$ can form when $D \geq 4\sigma$. Generally, a maximum of m layers can form when $2m\sigma < D < (2m + 1)\sigma$, and the total number of molecules becomes

$$N_m = \pi \sum_{n=1}^m \left(\arcsin \frac{\sigma}{D - (2n - 1)\sigma} \right)^{-1} \quad (6.40)$$

If the pore diameter is in the range $(2m + 1)\sigma < D < 2(m + 1)\sigma$, a further particle fits in at the center of the pore, so that the total number of particle becomes $N_m + 1$. For $m = 1$ this is the situation when D is between 3σ and 4σ . Here, 6 particles form the outer layer in contact with the pore wall and one further particle is near the center of the pore.

As mentioned above, the approximation for calculating N as a function of D/σ assumes that the protein molecules are arranged in non-overlapping concentric rings. Accordingly, the limiting value of ϕ_m for large D/σ calculated with this relation is lower than the packing fraction of a 2D hexagonal lattice, which is $\phi_{2D} = \pi/2\sqrt{3} \approx 0.907$.

Chapter 7 Secondary Confinement of Water Observed in Eutectic Melting of Aqueous Salt Systems in Nanopores⁵

7.1 Introduction

Phase transitions at the nanoscale, such as the condensation of vapors or the freezing of liquids in narrow pores, are of fundamental interest for the understanding of competing interactions in strongly confined systems.^{174–176} Systems of interest cover a wide variety of host materials of well-defined pore geometry, such as graphene nanocapillaries,¹⁷⁷ metal-organic frameworks,¹⁷⁸ cryo-cooled protein crystals,¹⁷⁹ zeolites,¹⁸⁰ and ordered mesoporous silica.^{181–183} Water confined in the cylindrical pore channels of MCM-41 or SBA-15 silica exhibits a large freezing point depression, increasing with decreasing pore diameter. Water molecules at the pore wall are strongly interacting with surface silanol groups and do not participate in this phase transition. The density of water in the central part of the pore strongly decreases below the normal freezing temperature. Accordingly, the density increment of the solid/liquid transition becomes quite small in pores of diameter less than 3.5 nm,¹⁸⁴ and freezing/melting as a first-order phase transition disappears below a pore diameter of ca. 2.5 nm.^{185,186}

In contrast with the extensive work devoted to pure water, little attention has been paid to phase transitions of aqueous solutions in pores. Aqueous salt systems are of particular interest, since the nature and range of the dominating interactions are strongly dependent on the salt concentration, and because the two components undergo different processes at the solid/liquid transition: while water is melting, the salt dissolves in ionic form and thus requires the presence of liquid water. In addition, novel volumetric effects may come into play with salts crystallizing in form of hydrates, which may take up significantly more space in the pores than anhydrous salts. Generally, a shift of the solid/liquid phase transition of salt solutions in pores occurs as a combination of confinement and colligative¹⁸⁷ effects (see Fig. 7.1): The melting temperature of pure water in the pores is shifted by an increment $\Delta T_p^0 = T^0 - T_p^0$ that depends on the pore diameter D (Fig. 7.1a). When salt is added, the freezing point of water is lowered proportional to the salt concentration (liquidus line L in Fig. 7.1b). The liquidus line of ice and the solubility line of the salt intersect at the eutectic point (temperature T_E , salt molality m_E). The eutectic temperature in the pore, $T_{E,p}$, is shifted against the bulk eutectic temperature by an increment $\Delta T_p = T_E - T_{E,p}$.

In this work we determined ΔT_p for several aqueous alkali halide systems in the pore channels of SBA-15 and MCM-41 materials. At the eutectic point some of these salts crystallize

⁵ Reproduced with permission from J. Meissner, A. Prause, G. H. Findenegg, *J. Phys. Chem. Lett.* **2016**, 7 (10), 1816. Copyright 2016 American Chemical Society.
<http://dx.doi.org/10.1021/acs.jpcllett.6b00756>

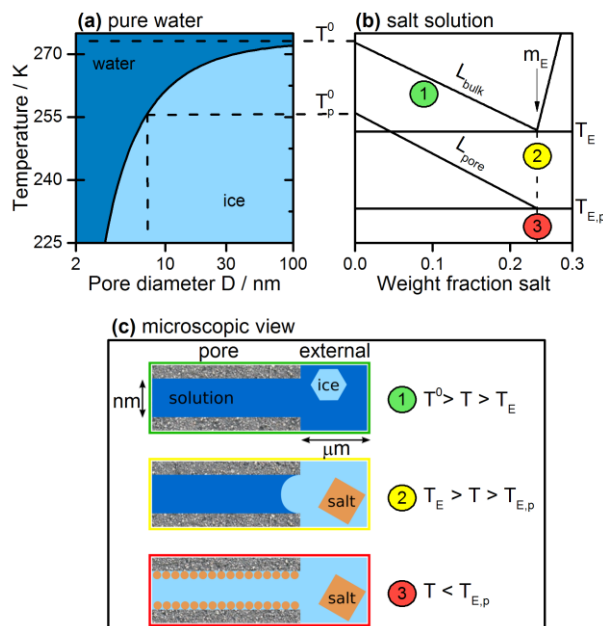


Figure 7.1: (a) Sketch of melting temperature vs. pore diameter D for pure water; (b) melting lines and eutectic temperature of salt solution in bulk and in a pore of diameter D ; (c) aqueous eutectic mixture in pores and external reservoir for three temperature ranges of a cooling scan: (1) between the freezing temperature of pure water (T^0) and the bulk eutectic temperature (T_E); (2) between T_E and the pore eutectic temperature ($T_{E,p}$); (3) below $T_{E,p}$. Note that the external reservoir has a thickness in the μm range while the pore width is in the nm size range.

as oligohydrates, others in anhydrous form. We find a remarkable increase of ΔT_p with the fraction of volume occupied by salt in the solid eutectic mixture. We attribute this effect to a stronger confinement of water/ice in the pores due to the precipitated salt. To the best of our knowledge such an effect, which we call *secondary confinement* (as distinct from confinement in pristine pores), has not been reported previously.

7.2 Results and Discussion

Well-characterized SBA-15 and MCM-41 silica materials, designated as SBA-A ($D = 7.1$ nm), SBA-B (8.5 nm) and MCM (4.4 nm) were used in this study (see Appendix). For the DSC measurements the materials were overfilled with salt solution, such that about 25 percent of the solution was confined in the pores and a threefold excess remained unconfined (external reservoir; Fig. 7.1c). No salt exclusion from the pores is expected at the present high salt concentrations, at which the Debye length λ_D is typically 0.1 nm and the condition $D/\lambda_D \gg 1$ applies for all samples studied.¹⁸⁸ Figure 7.1a shows the DSC cooling/heating scan of a 10 wt% NaCl solution in SBA-A. The endothermic peaks on the heating scan result from eutectic melting in the pores (P) and from eutectic melting (E) and melting of ice along the liquidus line (L) in the external reservoir. The corresponding exothermic peaks on the cooling scan are labeled as P_f , E_f and L_f . Here we focus on the results from the heating scans which yield phase transition temperatures close to thermodynamic equilibrium. A phase diagram

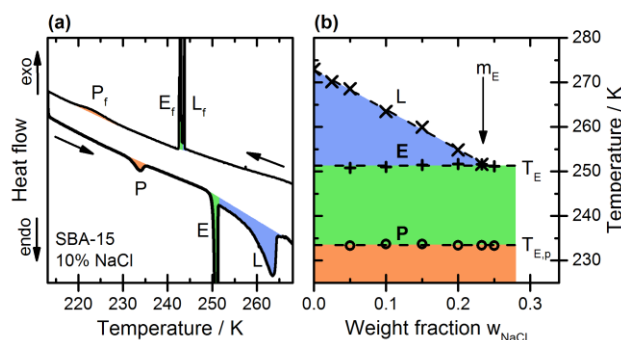


Figure 7.2: (a) DSC cooling/heating scans of a 10 wt% aqueous NaCl solution in SBA-A. Peaks on the heating scan are labeled P (pore), E and L (external sample), peaks on the cooling scan P_f (pore), E_f and L_f (external sample); (b) phase diagram NaCl + water derived from DSC heating scans: Data for the liquidus line (L) and eutectic temperature (E) of external sample and pore eutectic temperature (P).

derived from samples with salt concentrations up to the eutectic composition is shown in Figure 7.2b. Notably, no pore freezing/melting liquidus line (L_{pore} in Fig. 7.1b) is observed in the cooling/heating scans. The absence of this transition in the pores is a signature of overfilled samples and can be rationalized from the sample geometry (Fig. 7.1c): During cooling, precipitation of ice in the reservoir causes a gradual increase of the salt concentration in the external solution and in the pores, since the salt concentration in the pores can equilibrate with the reservoir down to the (undercooled) eutectic freezing temperature of the reservoir. At this temperature the pore liquid of all samples has attained the eutectic composition, irrespective of their initial composition, and only eutectic freezing/melting occurs in the pores. DSC cooling/heating scans reveal that the hysteresis of the eutectic phase transition in the pores (P vs. P_f) is weaker than in the external sample, suggesting that the transition in the pores is nucleated by the external solid:¹⁸² As sketched in Figure 7.1c, ice bulges into the pore entrance at $T < T_E$ and propagates into the pore at the temperature at which the thermodynamic Gibbs-Thomson equation is fulfilled for the diameter of the pore entrance.^{186,189} Salt nano-crystals will precipitate from the oversaturated solution in the region next to the ice front and may accumulate near the pore walls as the ice front moves ahead (Fig. 7.1c).

We now turn to a comparison of the confinement-induced shift of the eutectic temperature, $\Delta T_p = T_E - T_{E,p}$, for a series of alkali halides. Eutectic pore melting peaks for NaCl, KCl, RbCl and CsCl in SBA-A are shown in Figure 7.3a, where for each salt the temperature scale is normalized to the onset of the bulk eutectic melting peak. Also shown is the pore melting peak of pure water normalized to the melting peak of bulk water. Note that ΔT_p can be greater or smaller than ΔT_p^0 , the melting point depression of pure water. The highest ΔT_p value in this series of alkali chlorides is found for NaCl, the salt that crystallizes in form of a dihydrate at the eutectic point, while the others crystallize in anhydrous form.¹⁹⁰

For two of the salts studied (NaBr and KF) more than one DSC signal appears below the bulk eutectic transition. Heating scans from repeated cooling-heating cycles performed at different scan rates are presented in Fig. 7.3b and 7.3c. For both these salts two oligohydrates

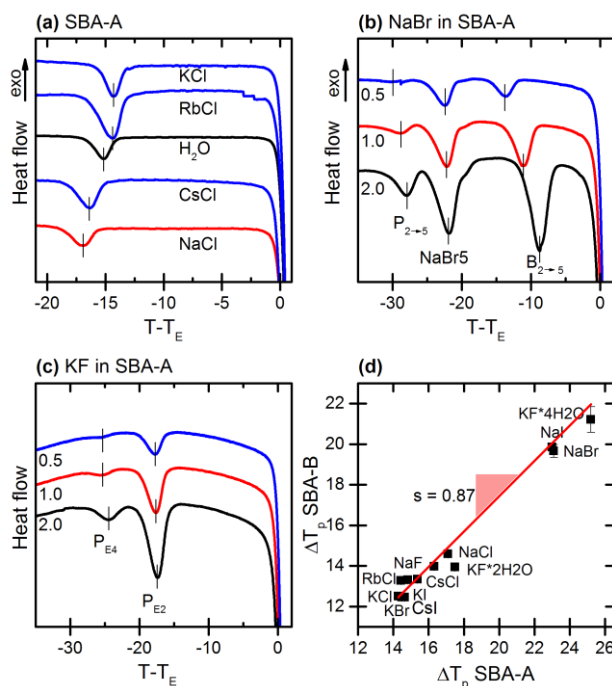


Figure 7.3: (a) DSC heating scans for eutectic salt systems confined in SBA-A, monitoring transitions below the bulk eutectic temperature T_E : (a) pore melting of NaCl, KCl, RbCl, CsCl and pure H₂O (scan rate 0.5 K/min); (b) and (c): multiple peaks detected for NaBr and KF at three different scan rates (2, 1 and 0.5 K/min) (see text for explanation); (d) comparison of eutectic melting point depression ΔT_p of all salts in pores of SBA-A and SBA-B.

appear in the phase diagram: a dihydrate and a tetrahydrate for KF (abbreviated as KF2 and KF4), a dihydrate and a pentahydrate for NaBr (abbreviated as NaBr2 and NaBr5). In both cases the higher hydrate represents the stable form at the eutectic temperature (see Appendix). DSC scans for NaBr + H₂O without the silica matrix indicate that metastable NaBr2 is formed in eutectic freezing, which transforms to NaBr5 on heating in a separate transition below eutectic melting (Appendix, Fig. 7.7). This transition (marked $B_{2 \rightarrow 5}$ in Fig. 7.3b) was confirmed by temperature-scanning XRD measurements (Appendix, Fig. 7.10). On the assumption that the same sequence of transitions as in bulk samples also occurs in the pores, we attribute the three peaks below bulk eutectic melting of the NaBr + H₂O system (Fig. 7.3b) to the transition from NaBr2 to NaBr5 ($P_{2 \rightarrow 5}$) and eutectic melting of NaBr5 (P_E) in the pores, and to the transition from NaBr2 to NaBr5 in the excess sample ($B_{2 \rightarrow 5}$). For the KF + H₂O system (Fig. 7.3c) DSC cooling scans indicate that both metastable KF2 and stable KF4 are formed in eutectic freezing (Appendix, Fig. 7.8), but in this case no transition from KF2 to KF4 can be detected in the heating scans. Hence the two transitions observed in the pores are attributed tentatively to eutectic melting of the tetrahydrate (P_{E4}) and dihydrate (P_{E2}).

For the set of alkali halides studied we find that the values of ΔT_p increase in a similar sequence in the three silica materials. For the two SBA materials this is shown in Figure 7.2d, where the ΔT_p values for SBA-B are plotted against the values for SBA-A. The data can be represented by a line through the origin having a slope $s = 0.87$, consistent with the ratio of the melting point depression values ΔT_p^0 of pure water in the two materials ($13.1/15.1 = 0.87$).

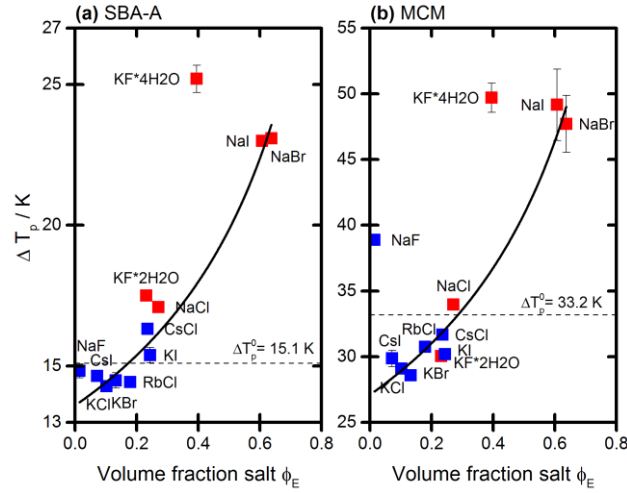


Figure 7.4: Depression of the eutectic temperature ΔT_p of aqueous alkali halide systems plotted as a function of the volume fraction ϕ_E of salt in the solid eutectic mixture. Experimental data (symbols; red for salts crystallizing as oligohydrates, blue for anhydrites), and fit of the data by Equation 7.2 (full line). (a) Confinement in SBA-A; (b) in MCM.

Higher values of ΔT_p are found for all salts in MCM, as expected from its smaller pore size. A diagram of ΔT_p values in MCM vs. SBA-A similar to Figure 7.3d is shown in the Appendix (Fig. 7.12). The similar sequence of the ΔT_p values in the three materials suggests a genuine salt-specific behavior for the eutectic melting in pores. Notably, for all three matrices the largest ΔT_p values are found for those salts for which the stable form at the eutectic temperature is a higher oligohydrate, viz., KF (tetrahydrate), NaBr (pentahydrate) and NaI (pentahydrate) (see Appendix). It is revealing to correlate ΔT_p with the volume fraction of the salt phase in the solid eutectic mixture, $\phi_E = x_E V_S / [V_I + x_E (V_S - V_I)]$, where V_S and V_I represent the molar volumes of the salt phase and ice, and x_E is the mole fraction of salt (hydrate) given by $x_E = n_S / (n_W + n_S - h_E n_S)$, where h_E is the number of water molecules in the hydrate. Values of ϕ_E for the present alkali halide systems range from 0.015 (NaF) to 0.64 (NaBr · 5H₂O) (Appendix, Table 7.3). Figure 7.4 shows the ΔT_p values in SBA-A and MCM plotted against ϕ_E . For both pore sizes we observe a pronounced increase of ΔT_p with increasing ϕ_E . The deviating behavior of NaF and KF will be discussed later.

The observed increase of ΔT_p with the fraction of pore volume occupied by solid salt (Fig. 7.4) suggests that precipitated salt causes a *secondary confinement* (SC) for water/ice in the pores. A simple expression for the salt-induced melting-point depression is obtained for the case when the precipitated salt forms a layer of crystallites near the pore wall, as sketched in Figure 7.1c. In this case the effective core radius within which crystallization of water occurs is reduced from R_c to a smaller value R_{SC} . From the concomitant decrease of the cross-sectional core area one finds¹⁹¹ $R_{SC}/R_c = \sqrt{1 - \phi_E}$. We infer that the melting point depression of water in the core of the salt-containing pores conforms to a Gibbs-Thomson relation $\Delta T_{SC} = C_{GT}/R_{SC}$, as in the absence of salt, when $\Delta T_p^0 = C_{GT}/R_c$.^{174,182} Hence, the salt-induced melting point

depression will be related to the melting point depression of water/ice in the absence of salt, ΔT_p^0 , by

$$\frac{\Delta T_{sc}}{\Delta T_p^0} = \frac{1}{\sqrt{1 - \phi_E}} \quad (7.1)$$

According to this relation we expect $\Delta T_{sc} = \Delta T_p^0$ for $\phi_E = 0$ and an increase of ΔT_{sc} proportional to $(1 - \phi_E)^{-1/2}$ with increasing ϕ_E . Figure 7.4 shows, however, that for salts with low ϕ_E the melting point depression ΔT_p is somewhat smaller than ΔT_p^0 . Hence, salt-induced confinement alone does not account for the depression of the eutectic temperature in the pores, but a further effect must exist that causes this negative contribution to ΔT_p . We surmise that this contribution arises from salt-specific or ion-specific influences on the non-freezing layer (nfl) at the pore wall. Denoting this by a (positive) term ΔT_{nfl} we obtain

$$\Delta T_p = \Delta T_{sc}(\phi_E) - \Delta T_{nfl} = \Delta T_p^0(1 - \phi_E)^{-1/2} - \Delta T_{nfl} \quad (7.2)$$

For a test of Equation 7.2 we adopt the experimental melting point depression of pure water in the silica matrix (ΔT_p^0 values in Fig. 7.4) and take ΔT_{nfl} as an adjustable parameter. The curves in Figure 7.4 represent Equation 7.2 with $\Delta T_{nfl} = 1.5$ K for SBA-A and $\Delta T_{nfl} = 6.1$ K for MCM. The corresponding graph for SBA-B is shown in the Appendix (Fig. 7.13). It is remarkable that a relation based on a simple model with a single adjustable parameter reproduces the main trend of the eutectic point depression data of the alkali halide systems in the nanopores.

For NaF in MCM and for KF4 in all matrices we find higher values of ΔT_p than expected on the basis of Equation 7.2 (Fig. 7.4). One possible cause for this is the strong hydrogen bond interaction of fluoride ions with water and surface silanol groups, which may lead to a larger thickness of the nonfreezing layer at the pore wall and a concomitant greater ΔT_p .¹⁸² For salts composed of large, weakly hydrated (chaotropic) ions we generally find low ΔT_p values but no hint at size dependent adsorption effects of cations at the negatively charged silica surface, as reported in the literature.¹⁹² Changing from pH 5 (at which the present results were obtained) to pH 9 had no noticeable effect on ΔT_p for the NaCl system, where we expected stronger adsorption of the cations at higher pH. These findings show that ion-specific surface charge effects⁴⁵ are screened to a length scale of the ionic diameter at the high ionic strength of the present systems. On the other hand, the trends emerging from Figure 7.4 are in line with the concept of matching water affinities of the ions forming a salt,¹⁹³ in the sense that salts formed by ions of similar size (NaF, CsI) are weakly soluble (low ϕ_E and ΔT_p) while salts formed by ions of strongly different size (NaBr, NaI) are highly soluble (high ϕ_E and ΔT_p).

We have estimated the size of salt crystallites in the pores by X-ray diffraction from the width of Bragg reflexes, using the Scherrer equation.¹⁹⁴ For dried samples at room temperature this yields a typical crystallite size of about 1 nm (Appendix, Fig. 7.9). Although the Scherrer

equation is not applicable to such small crystals we adopt this value in the following geometric consideration. If in pores of diameter D the salt crystallites form a layer of thickness d at the pore wall, the mean volume fraction ϕ_E can be expressed by the reduced density ρ_{salt} of salt particles in this layer and the fraction of the pore volume φ making up the layer, i.e., $\phi_E = \rho_{\text{salt}}\varphi$, where $\varphi = 1 - (1 - 2d/D)^2$. Hence for a monolayer of 1 nm sized crystallites ($d = 1$ nm) and an assumed maximum packing density $\eta_{\text{max}} = 0.5$ in the layer we find that salt up to a maximum ϕ_E of 0.24 (for SBA-A, $D = 7.1$ nm) and 0.35 (for MCM, $D = 4.4$ nm) can be accommodated. For higher values of ϕ_E , as they are found for the oligohydrate salts (Fig. 7.4), the thickness of the salt layer will exceed a monolayer. In the case of MCM this implies that the free core of the pores available for ice will have a thickness of less than 2.5 nm. In this context it is of interest that exceptionally broad DSC pore melting peaks were found for the salts with the highest ϕ_E and ΔT_p (NaBr, NaI and KF) in MCM (Appendix, Fig. 7.11). We suspect that in these cases, in which the pore eutectic temperature is below 210 K, no first-order freezing/melting of water occurs in the pores of MCM, similar to the situation of pure water in pores of diameter below 2.5 nm.^{185,186} An experimental test of the geometrical model discussed above by temperature-scanning small-angle X-ray scattering is currently in progress.

7.3 Conclusion

In conclusion, we have found that the shift of the eutectic melting temperature of aqueous salt systems in nanosized pores depends on the fraction of volume occupied by the solid salt. Salts crystallizing as voluminous hydrates at the eutectic temperature cause a stronger depression of the eutectic temperature than salts crystallizing in anhydrous form. We model this effect by assuming that solid salt represents a secondary confinement for water/ice in the pores. The different role played by the two solid phases in the eutectic phase transition can be rationalized by recalling that melting of ice is pre-requisite for the dissolution of salt. Secondary confinement may play a role in many technologically relevant fields, whenever nanoporous materials are impregnated with salts or related substances, e.g., for supported metal oxide catalysts,^{195,196} trapping of radioactive waste,¹⁹⁷ advanced adsorbents,¹⁹⁸ or adsorption heat transformation devices.¹⁹⁹ In addition, salt crystallization in the pores of stone and brick is believed to be a major reason for the destruction of building materials by salt weathering. The existence of different hydration states of the crystals appears to play an important role in these processes.^{200,201}

7.4 Appendix

7.4.1 Characterization of silica materials

The MCM-41 and SBA-15 silica materials used in this study were prepared by the methods described previously.^{186,202} The specific surface area, the pore volume, and the pore size distribution (PSD) of the materials was characterized by nitrogen adsorption at 77 K and argon adsorption at 87 K. Figure 7.5 shows the adsorption-desorption isotherms for the samples MCM and SBA-A and their PSD as derived from the desorption branch of the isotherms on the basis of the nonlocal density functional theory (NLDFT) with the kernel for cylindrical silica pores.¹⁵¹

Values of the specific surface area (BET), the total pore volume and the mean diameter of the cylindrical pore channels of the materials are summarized in Table 7.1. Also included are values of the pore lattice parameter determined from the 10 reflection of the 2D pore lattice. A further sample, denoted as SBA-B, was characterized only by nitrogen adsorption.

Table 7.1: Specific surface area a_s , total specific pore volume v_p , mean pore diameter D and pore lattice parameter a_0 of the MCM-41 and SBA-15 silica samples.

sample	gas	$\frac{a_s}{\text{m}^2 \text{ g}^{-1}}$	$\frac{v_p}{\text{cm}^3 \text{ g}^{-1}}$	$\frac{D}{\text{nm}}$	$\frac{a_0}{\text{nm}}$
MCM	N ₂	811	0.79	4.45 ± 0.03	5.13 ± 0.01
	Ar	686	0.75	4.38 ± 0.03	
SBA-A	N ₂	786	0.85	7.12 ± 0.05	10.89 ± 0.03
	Ar	655	0.82	6.86 ± 0.05	
SBA-B	N ₂	582	0.87	8.5 ± 0.2	

7.4.2 Eutectic point of bulk systems

Literature data for the eutectic point of the alkali halide + water systems studied in this work are given in Table 7.2. Here, T_E represents the eutectic temperature and w_E the eutectic composition expressed as weight fraction of salt. The salt concentration expressed as molality m_E (mol per kg water) is obtained from w_E by the relation $m_E = w_E / M_S (1 - w_E)$, where M_S is the molar mass of salt (kg/mol). In four of the eleven systems a salt hydrate coexists with ice and solution at the eutectic point. The respective hydration number h_E (number of water molecules per unit salt) is also given in Table 7.2.

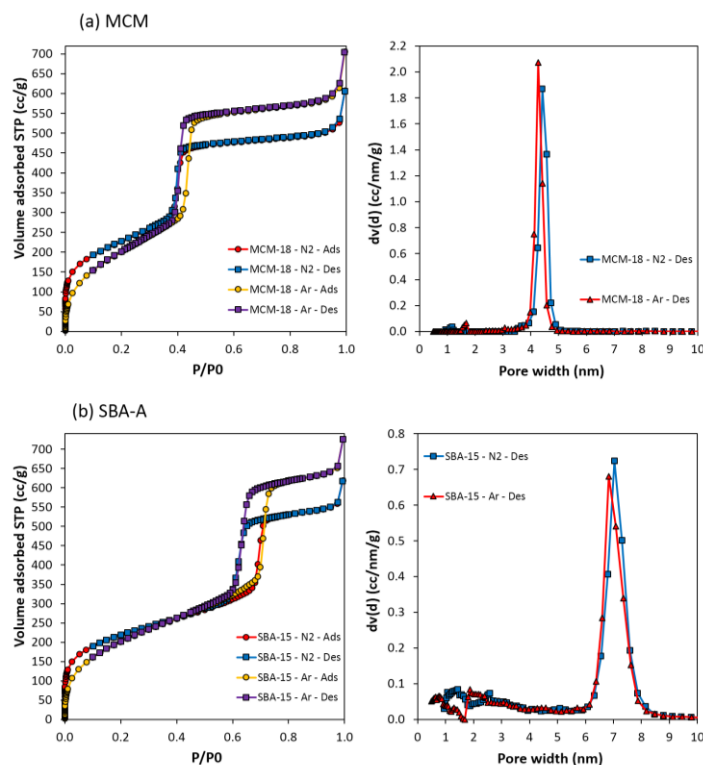


Figure 7.5: Adsorption/desorption isotherms of nitrogen and argon (left) and pore size distribution derived from the desorption branch (right) for the samples (a) MCM; (b) SBA-A.

In the present DSC study the eutectic temperature of the bulk system is defined as the onset temperature of the eutectic melting peak of the excess sample. A comparison of these values, $T_E(\text{exp})$, with literature data of $T_E(\text{Lit})$ (Table 7.2) is shown in Figure 7.6.

Table 7.2: Eutectic point data of alkali halide + water systems.

Salt	$\frac{T_E}{K}$	w_E	$\frac{m_E}{\text{mol kg}^{-1}}$	h_E	reference
NaF	269.9	0.039	0.97	0	167
NaCl	251.90	0.232	5.17	2	168
NaBr	245.15	0.403	6.47	5	169
NaI	241.65	0.471	5.94	5	170
KF	251.5	0.219	4.83	4	167
KCl	262.50	0.196	3.27	0	168
KBr	260.55	0.313	3.83	0	169
KI	250.10	0.522	6.58	0	169
RbCl	256.75	0.398	5.46	0	168
CsCl	249.45	0.569	7.84	0	171
CsI	269.15	0.274	1.45	0	172

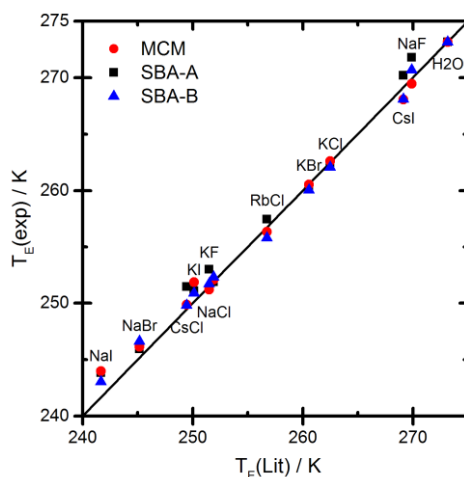


Figure 7.6: Experimental values of the bulk eutectic temperature $T_E(exp)$ of the alkali halide + water systems correlated with literature values of $T_E(Lit)$ (Table 7.2). The $T_E(exp)$ values represent values for the excess phase with the three silica materials.

7.4.3 Systems Forming Salt Hydrates

NaCl: The dihydrate $NaCl \cdot 2H_2O$ is the only hydrate formed in the $NaCl$ + water system at normal pressure. It represents the stable phase in equilibrium with the aqueous solution from the eutectic temperature (251.9 K) to 271.9 K. Anhydrous $NaCl$ is the stable form at higher temperatures.²⁰³

NaBr: Two hydrates are formed in the $NaBr$ + water system. The pentahydrate $NaBr \cdot 5H_2O$ is the stable form in equilibrium with aqueous solution from the eutectic temperature (245.2 K) to 248.8 K. The dihydrate $NaBr \cdot 2H_2O$ is the stable form from 248.8 K to 324.4 K, and anhydrous $NaBr$ is the stable form at higher temperatures. Note that the pentahydrate represents the stable form only in a rather narrow range.²⁰⁴

NaI: Two hydrates are formed in the NaI + water system. The pentahydrate $NaI \cdot 5H_2O$ is the stable form in equilibrium with aqueous solution from the eutectic temperature (241.7 K) to 260.9 K, followed by the dihydrate $NaI \cdot 2H_2O$, which is the stable form up to at least 313 K.²⁰⁵

KF: Two hydrates are also formed in the KF + water system. The tetrahydrate $KF \cdot 4H_2O$ is the stable form in equilibrium with aqueous solution from the eutectic temperature (251.5 K) to 290.9 K. The dihydrate $KF \cdot 2H_2O$ is the stable form from 290.9 K to approximately 318 K, and anhydrous KF is the stable form at higher temperatures.²⁰⁶

7.4.4 Volume fraction of Salt in Solid Eutectic Mixtures

The volume fraction of the salt phase in the solid eutectic mixture is given by

$$\phi_E = \frac{x_E V_S}{V_I + x_E(V_S - V_I)} \quad (7.3)$$

where V_S and V_I denote the molar volumes of the salt phase and ice, respectively, and x_E is the mole fraction of salt in the mixture. In the case of salt hydrates we have to take into account that the amount of free (unbound) water is reduced and given by $n_W - h_E n_S$, where n_W and n_S represent the overall amounts of water and salt, and h_E is the number of water molecules per unit salt in the hydrate. Accordingly, a general expression for the mole fraction x_E is¹⁸⁷

$$x_E = \frac{n_S}{n_W + n_S - h_E n_S} \quad (7.4)$$

which can be expressed in terms of the molality m_E as

$$x_E = \frac{m_E}{55.51 + (1 - h_E)m_E} \quad (7.5)$$

Values of the volume fraction ϕ_E estimated on the basis of Equation 7.3 and 7.5 for the present systems are summarized in Table 7.3. A value $V_I = 19.5 \text{ cm}^3/\text{mol}$ was adopted for the molar volume of ice from its density at 233.15 K.²⁰⁷ The molar volume of the anhydrous salts was taken from their density.²⁰⁸ For salts crystallizing as hydrates, V_S was obtained either from crystal structure data (sodium chloride dihydrate,²⁰⁹ potassium fluoride dihydrate²¹⁰ and tetrahydrate,²¹¹ sodium bromide dihydrate²¹²), or estimated by assuming volume additivity of anhydrous salt and water (pentahydrates of NaBr and NaI). This assumption causes an overestimate of the composite volume of typically 5-7%, which for the given salt hydrates translates into an error in ϕ_E of 2-3%. The overall error in ϕ_E resulting from the uncertainty of the molar volumes of salt and ice and the composition of the mixture in the pores is estimated to be less than 5%.

Table 7.3: Molar volume V_S of alkali halides and volume fraction ϕ_E in solid eutectic mixture based on Equation 7.3 and 7.5. The salts are listed in ascending order of ϕ_E . For salts for which two hydrates exist, ϕ_E values for both phases are given.

Salt	$\frac{m_E}{\text{mol kg}^{-1}}$	h_E	$\frac{V_S}{\text{cm}^3 \text{mol}^{-1}}$	ϕ_E
NaF	0.97	0	16.4	0.015
CsI	1.45	0	57.6	0.072
KCl	3.27	0	37.6	0.102
KBr	3.83	0	43.3	0.133
RbCl	5.46	0	43.2	0.179
CsCl	7.84	0	42.4	0.235
KI	6.58	0	53.0	0.244
NaCl · 2H ₂ O	5.17	2	63.0	0.271
KF · 2H ₂ O	4.83	2	55.8	0.232
KF · 4H ₂ O	4.83	4	90.3	0.395
NaI · 2H ₂ O	5.94	2	75.9	0.346
NaI · 5H ₂ O	5.94	5	130.9	0.607
NaBr · 2H ₂ O	6.47	2	64.4	0.335
NaBr · 5H ₂ O	6.47	5	122.2	0.637

7.4.5 Information from DSC Cooling Scans

Much information about phase transitions in the pores was obtained from successive DSC cooling-heating cycles performed at different scan rates. High rates provide high sensitivity, subsequent scans at lower rate probe rate-dependent shifts of the peak position. Heating scans resulting from such cycles are shown in Figure 7.2b and 7.2c. Here we present complementary information gained from the cooling scans of successive cooling-heating cycles.

NaBr + water. Figure 7.7a shows the cooling scans from repeated cooling-heating cycles for an eutectic NaBr + H₂O mixture imbibed in SBA-A. The large exothermic feature between 240 and 230 K results from supercooled eutectic freezing of the excess sample. At the higher scan rates (2 K/min, 1 K/min) it consists of two sharp signals which we attribute to the formation of NaBr dihydrate (NaBr₂) and pentahydrate (NaBr₅), in view of the fact that NaBr₂ represents the stable form down to nearly the eutectic temperature (see Section 7.4.3). The broad features below the bulk eutectic transition result from transitions in the pores. The two overlapping peaks marked as P1 and P2 may be caused, by analogy with the bulk system, from eutectic freezing involving the formation of NaBr₂ and NaBr₅. More likely, P1 results from eutectic

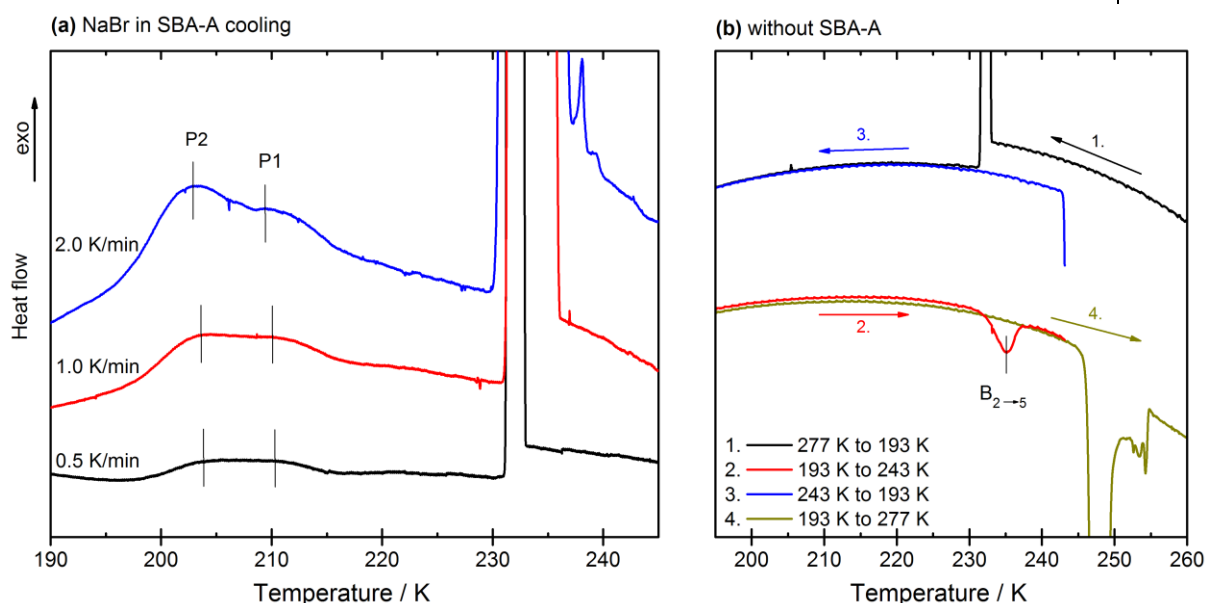


Figure 7.7: DSC of eutectic aqueous NaBr: (a) cooling scans for the solution imbibed in SBA-A at cooling rates 2.0, 1.0 and 0.5 K/min; the broad overlapping signals shown in the inset are attributed to the transitions in the pores; (b) cooling-heating cycle of the bulk sample without silica matrix (see text for explanation).

freezing with formation of NaBr₂, and P2 from the transition from metastable NaBr₂ to stable NaBr₅ in the pores.

Indirect evidence for this solid-state transition in the pores comes from DSC of the NaBr + H₂O bulk system (without the silica matrix). A cooling-heating cycle of the eutectic bulk mixture (scan rate 0.5 K/min) is shown in Figure 7.7b. Supercooled eutectic freezing occurs near 233 K and no further transition takes place down to 200 K. In the subsequent heating scan a smaller endothermic peak, marked as B₂→₅, appears at 233 K. Importantly, this peak does not re-appear, neither on cooling nor heating, as long as the temperature is cycled below eutectic melting. This finding indicates that eutectic freezing of the sample leads – at least in part – to the metastable form NaBr₂, which then transforms to the stable form NaBr₅ on heating in the transition B₂→₅. This assignment is in accordance with the Ostwald rule of stages, according to which crystallization from solution often starts in such a way that the thermodynamically unstable form appears first, followed by re-crystallization to the thermodynamically stable phase.^{200,213} The presence of two hydrate forms in the NaBr + H₂O system was also confirmed by low-temperature XRD (see Section 7.4.5).

Based on these complementary findings we attribute the three signals observed in the heating scans of the NaBr + H₂O system below the bulk eutectic temperature (Fig. 7.2b of the main text) to the conversion of dihydrate to pentahydrate (P₂→₅) and eutectic melting in the pore (P_E), and to the conversion of dihydrate to pentahydrate in the excess (bulk) sample (B₂→₅).

KF + H₂O. In the KF + H₂O system, the tetrahydrate (KF₄) represents the stable form in a broader temperature range above the eutectic point (see Section 7.4.3). DSC measurements of the bulk system (without silica) indicate that no phase transitions take place below the eutectic

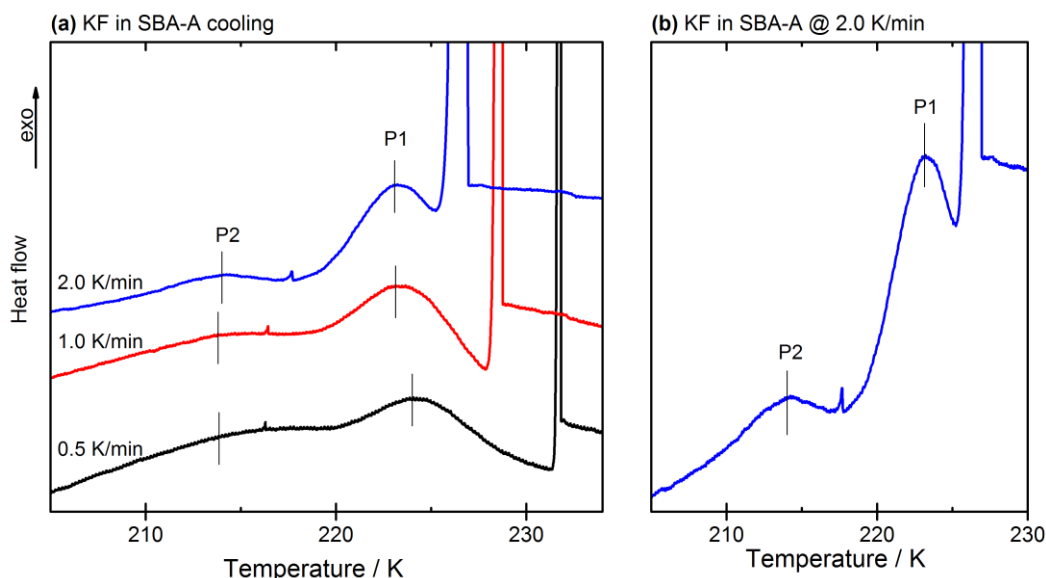


Figure 7.8: DSC of eutectic aqueous KF imbibed in SBA-A: (a) cooling scans at different cooling rate (2 K/min, 1 K/min, 0.5 K/min); (b) enlarged view of the scan at 2 K/min. The rounded peaks P1 and P2 below the bulk eutectic freezing transition are attributed to transitions in the pores, namely eutectic freezing with formation of metastable KF2 (P1) and partial conversion of KF2 to PF4 (P4).

temperature. Yet DSC heating scans in the presence of SBA-A show that two transitions are occurring in the pores below bulk eutectic melting (Fig. 7.2c).

Figure 7.8a presents cooling scans from a sequence of cooling-heating cycles taken at different scan rates for KF + H₂O imbibed in SBA-A. In each of the scans the sharp signal at the highest temperature represents supercooled eutectic freezing of the excess sample. Supercooling of this transition is most pronounced in the first scan (taken at 2 K/min) and smallest in the last scan (0.5 K/min).

The two smaller and rounded peaks at temperatures below supercooled freezing of the bulk sample, shown at enlarged scale in Figure 7.8b, correspond to phase transitions in the pores. By analogy with the NaBr + H₂O system and again based on Ostwald's rule of stages we infer that the larger peak at higher temperature (marked as P1 represents (nucleated) eutectic freezing in the pores with formation of the metastable KF dihydrate (KF2), and the small peak at lower temperature (marked as P2) to a partial conversion of KF2 to the stable form KF4. Unlike the case of NaBr, we have to infer that at temperatures below P2 part of the salt in the pores still exists in form of metastable KF2, and the rest as the stable form KF4.

Based on this assignment we attribute the two signals observed in the heating scans of the KF + H₂O system below the bulk eutectic temperature (see Fig. 7.2c) to pore eutectic melting with KF4 as the salt phase (P_{E4}) and pore eutectic melting with KF2 as the salt phase (P_{E2}). Eutectic melting with KF4 as the salt phase is believed to occur at a lower temperature than pore eutectic melting with KF2, in line with our model of secondary confinement, since KF4 occupies a larger fraction of the pore volume than KF2. However, this assignment of the two phase transitions in the pores is only tentative, as an independent proof is still missing.

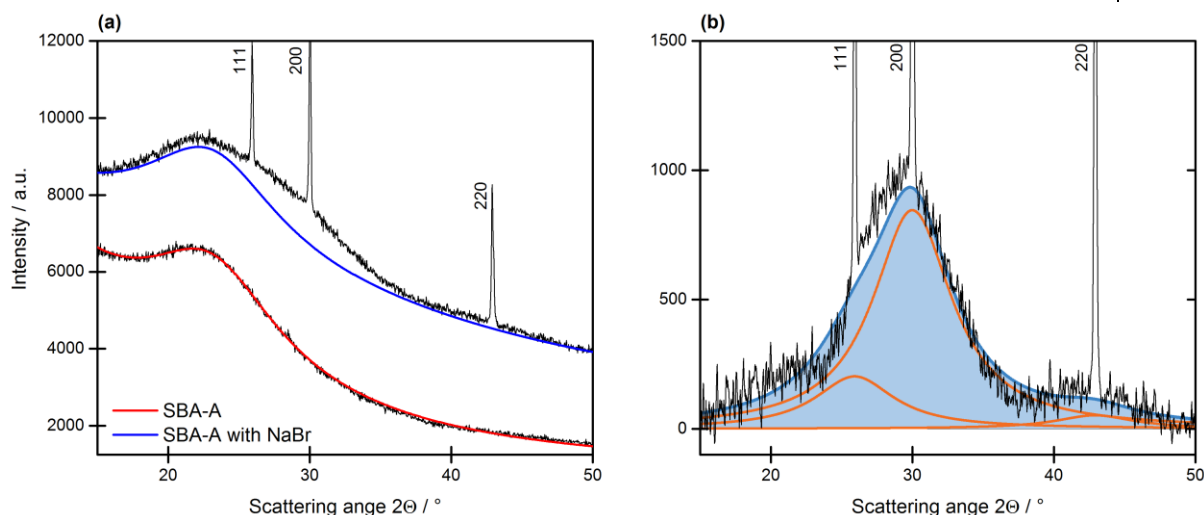


Figure 7.9: Scherrer analysis of a dried sample of NaBr in SBA-A: (a) subtraction of the background of pure SBA-A from the sample containing salt; (b) the signal after background subtraction is simulated by a superposition of three narrow and three broad Lorentzians.

7.4.6 Information from in situ XRD

Estimation of salt crystallite size. The size of salt crystallites in the pores was estimated by XRD from the width of the Bragg reflections, based on the Scherrer equation. Samples were prepared by imbibition of eutectic solution of NaBr into SBA-A and subsequent drying at room temperature. During the drying process of the slurry the concentration of salt in the pores increased due to diffusion from the external excess, but part of the excess salt crystallizes outside the pore space. Nitrogen adsorption measurements showed that about 30% of the pore volume was occupied by the dry salt.

Powder XRD profiles of the dry samples were recorded in a 2θ range of $15 - 50^\circ$ ($\text{Cu } K\alpha, \lambda = 1.54 \text{ \AA}$) (Fig. 7.9). After subtraction of the silica background (Fig. 7.9a) the remaining signal was modeled by a sum of six Lorentzians, each two centered at the position of the first three leading Bragg reflections (Fig. 7.9b).

Table 7.4: Peak height and peak width parameters I and $\Delta\theta$ of the Lorentzian functions used to represent the three leading Bragg reflections for NaBr outside and inside the pores of SBA-A.

hkl	2θ	I_b	I_p	$\Delta\theta_b$	$\Delta\theta_p$
	$^\circ$	a.u.	a.u.	$^\circ$	$^\circ$
111	25.92	3244	202	0.1215	6.801
220	30.00	5921	846	0.1215	6.801
200	42.91	3947	52	0.1215	6.801

$$I_{\text{total}} = I_{\text{bg}} + \sum_{i=1}^3 [\mathcal{L}_{\text{bulk}}(\theta_i, \Delta\theta_b, I_{i,b}) + \mathcal{L}_{\text{pore}}(\theta_i, \Delta\theta_p, I_{i,p})] \quad (7.6)$$

By allowing for two width parameters, $\Delta\theta_b$ and $\Delta\theta_p$, we obtain a narrow and a broad peak for each reflection, assigned to the external salt and the small salt crystallites inside the pores, respectively. Values of the parameters $I_{i,b}$, $I_{i,p}$, $\Delta\theta_b$, and $\Delta\theta_p$ are given in Table 7.4.

On the basis of the Scherrer equation¹⁹⁴ the volume averaged crystallite size is given by

$$L_{\text{hkl}} = \frac{k\lambda}{\beta \cos\theta_{\text{hkl}}} \quad (7.7)$$

with k : Scherrer constant, λ : wavelength, β : integral peak width, and θ : angular peak position. From the integral width of the broad peaks, $\beta = (\pi/2)\Delta\theta_p = 10.7$, and with $k = 0.94$ we find $\bar{L} = 0.9(4) \pm 0.1$ nm. This value represents only a rough estimate, since the Scherrer equation breaks down for very small crystals. We conclude that the salt crystallites in the pores have a size not greater than approximately 1 nm.

Evidence for different salt hydrates. Combined in situ X-ray diffraction and small-angle scattering measurements on the present samples were carried out at the Elettra synchrotron facility (Trieste, Italy). XRD data were recorded in a q -range of 16–27 nm^{−1} ($\lambda = 1.54$ Å) with a 2D PILATUS 100k detector in the temperature range 130–290 K. Due to experimental limitations only samples having a high excess of external salt solution could be studied. Accordingly, the observed XRD profiles result mainly from salt and ice crystals in the excess phase outside the pores. In addition, the resulting XRD profiles were affected by spurious ice formation at the outside of the sample capillary. Figure 7.10 shows the XRD profile for a eutectic sample of NaBr + H₂O (in contact with MCM) during a cooling/heating cycle (290–130–290 K). Bragg reflections assigned to hexagonal ice are marked with arrows. One observes a sharp change in the Bragg pattern at a temperature 231 K on the heating scan, indicating a phase transition of the salt in the excess sample. Within experimental accuracy this solid-state transition occurs at the same temperature as the small endothermic peak in the DSC heating scan marked as B₂→₅ in Figure 7.7b, which was attributed to a transition from NaBr dihydrate to pentahydrate. Hence, the XRD scan provides independent support for this conjecture, which also implies that in the cooling scan, part of the salt crystallizes as NaBr₂ instead of the stable form NaBr₅, in agreement with Ostwald’s rule of stages.

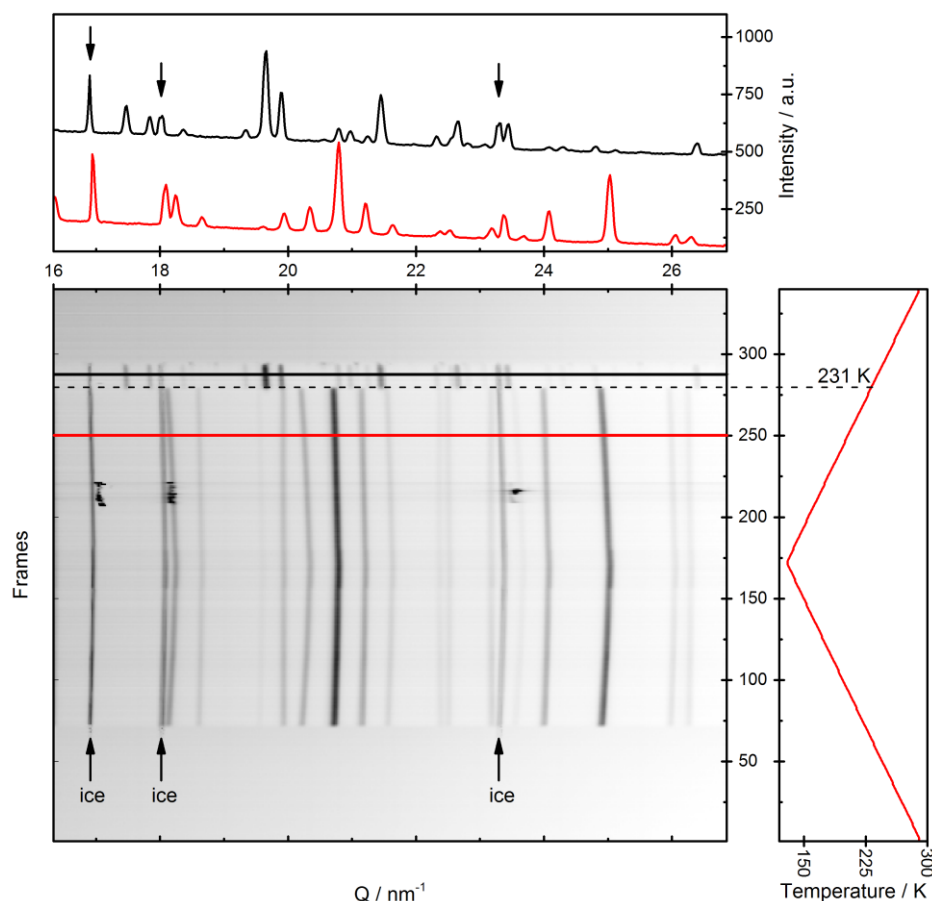


Figure 7.10: XRD profile of the eutectic NaBr + water system in contact with MCM during a cooling/heating cycle (290-130-290 K). Bragg reflections assigned to hexagonal ice are marked with arrows. A sharp change in the Bragg pattern appearing at 231 K in the heating scan is marked by a dashed line. The top panel shows the spectra for two selected temperatures, one below and one above the transition, as marked with lines in the lower panel.

7.4.7 Summarized DSC Pore Melting Results

Peak width of pore melting peaks. The width of eutectic melting peaks in the pores was defined as the difference between the peak maximum and onset temperatures, $\delta T = T_{\text{max}} - T_{\text{ons}}$. Mean values for the individual salts in each of the three matrices are given in Figure 7.11. To differentiate between the individual salts, Figure 7.11a shows δT plotted as a function of the eutectic temperature T_E of the systems (T_E values from Table 7.2). We find $\delta T = 2 \pm 1$ K for most salts in the pores of SBA-A and SBA-B, but higher values of δT , ranging from 3 to 10 K, in the more narrow pores of MCM. Figure 7.11b shows that as a general trend the peak width δT increases as the pore eutectic temperature $T_{E,p}$ decreases. A related trend has been reported in the literature for the freezing/melting of water in MCM-41 materials, where it was found that the width of the pore melting peak increases with decreasing pore diameter, i.e., lower pore melting temperature.¹⁸⁶ Hence, the trends of δT shown in Figure 7.11b are consistent with the concept of secondary confinement, since low values of $T_{E,p}$ (i.e., high values of ΔT_p) are

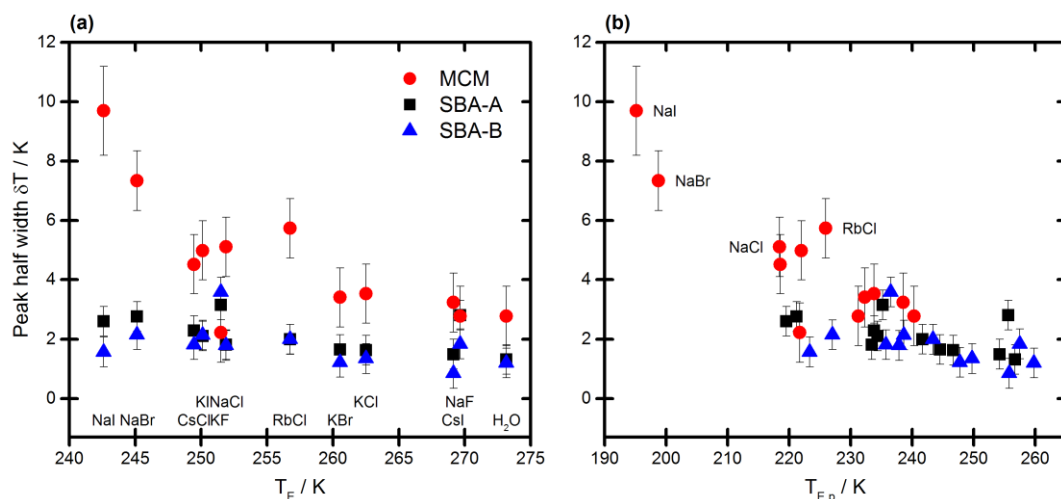


Figure 7.11: Half width δT of DSC pore melting peaks for the alkali halide salts in the pores of the three silica materials as indicated in the graph: (a) δT data plotted as a function of the eutectic temperature T_E ; (b) the same data plotted as a function of the pore eutectic temperature $T_{E,p}$. For KF4 in MCM the half width is greater than 12 K and cannot be determined accurately.

expected for a small effective pore width as it results from secondary confinement of water/ice by the precipitated salt.

Tabulated ΔT_p results and complementary figures. Experimental data of the eutectic melting point depression $\Delta T_p = T_E - T_{E,p}$ of the aqueous alkali halide systems confined in the pore channels of the three silica matrices are given in Table 7.5. These data represent mean values from a series of independent DSC measurements.

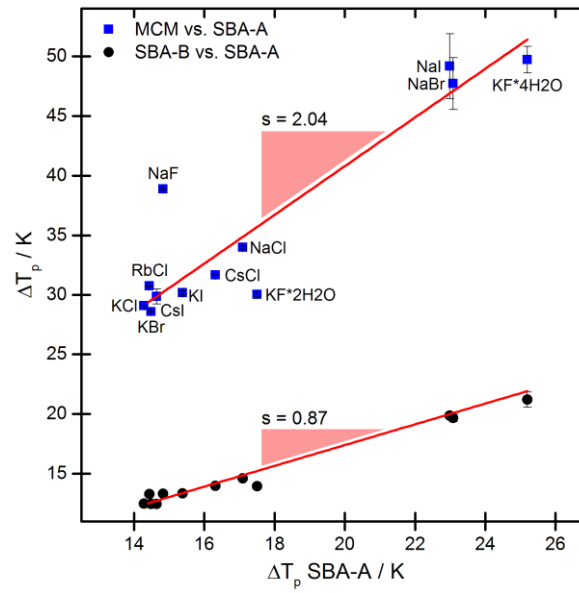


Figure 7.12: Eutectic melting point depression ΔT_p of the salt systems in MCM and in SBA-B plotted as a function of the corresponding ΔT_p values in SBA-A. The lines show linear regression of the data by regression lines through the origin.

Table 7.5: Eutectic temperature increment $\Delta T_E = T^0 - T_E$ of the external (bulk) samples and shift of the eutectic temperature in the pores, $\Delta T_p = T_E - T_{E,p}$ for the alkali halide systems in MCM, SBA-A and SBA-B. Values of the melting point depression of water in the three materials are also included.

Salt	ϕ_E	$\frac{\Delta T_p}{K}$	$\frac{\Delta T_p}{K}$	$\frac{\Delta T_p}{K}$	$\frac{\Delta T_p}{K}$
		external	MCM	SBA-A	SBA-B
H ₂ O	0	0.28	33.2	15.1	13.1
NaF	0.015	2.78	38.9	14.8	14.6
NaCl	0.271	21.33	34.0	17.1	14.6
NaBr	0.637	27.18	47.7	23.1	19.7
NaI	0.601	29.81	49.2	23.0	19.9
KF ₂	0.232	21.46	30.1	17.5	13.9
KF ₄	0.395	21.46	49.7	25.2	21.2
KCl	0.101	11.12	29.1	14.3	12.5
KBr	0.133	13.12	28.6	14.5	12.5
KI	0.243	22.15	30.2	15.4	13.3
RbCl	0.177	16.89	30.8	14.4	13.3
CsCl	0.235	23.05	31.7	16.3	14.0
CsI	0.072	4.65	29.9	14.7	12.5

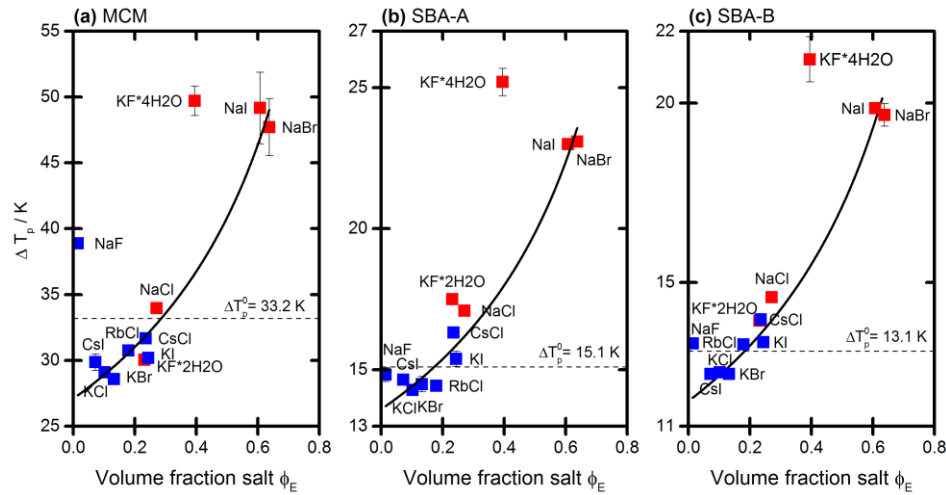


Figure 7.13: Depression of eutectic melting point in pores ΔT_p of the aqueous alkali halide systems plotted as a function of the volume fraction ϕ_E of salt in the solid eutectic mixture for (a) MCM; (b) SBA-A; (c) SBA-B. Experimental data (symbol) and fit of the data by Equation 7.2 (full line). The dashed line gives the melting point of water in the respective material. Red data points refer to salts crystallizing as oligohydrate, symbols to salts crystallizing in anhydrous form.

A correlation graph for the ΔT_p values of all salt systems in SBA-B and in SBA-A is shown in Figure 7.2d. Figure 7.12 presents a related correlation graph for the ΔT_p data of the salts in MCM and SBA-A. The correlation graph for SBA-B is also shown for comparison. Linear regression of the ΔT_p values in MCM vs. the ΔT_p values in SBA-A by a line through the origin yields a slope $s = 2.04$. This value is somewhat lower than the value expected from the melting point depression of ice/water in the two materials, $33.2/15.1 = 2.20$. The deviation of S from this value can be attributed mostly to the exceptionally high value of ΔT_p for NaF in MCM.

Graphs for the eutectic melting point depression ΔT_p as a function of the volume fraction ϕ_E of salt in the solid eutectic mixture for the salts in SBA-A and MCM are presented in Figure 7.3. A graph with the corresponding results for the salts in SBA-B is shown in Figure 7.13c. The graphs for SBA-A and MCM are also shown for comparison. The curves in Figure 7.13 represent Equation 7.2 with $\Delta T_{nfl} = 6.1$ K (MCM), 1.5 K (SBA-A) and 1.4 K (SBA-B).

Chapter 8 Conclusions and Outlook

In this concluding Chapter the main achievements of this Ph.D. thesis are summarized and discussed in the context of the existing research and its impact to recent literature. Additionally, new developments in the presented projects are outlined and an outlook to future work is given.

8.1 Protein Adsorption on Silica Nanoparticles on Above and Below the Isoelectric Point

In Chapter 3 experimental data for the adsorption of lysozyme (Lyz) and β -lactoglobulin (β -Lg) on silica nanoparticles were presented for a wide pH range. An important difference between these two proteins is their different IEP. While Lyz has its IEP at pH 11, the IEP of β -Lg is close to pH 5. The Lyz/SiNP system was chosen as it was used extensively in earlier experiments to investigate the structural characteristics of the hetero-aggregates formed in a wide pH range. This system represents an ideal model system for protein nanoparticle interaction studies, but the high IEP of Lyz limits the accessible pH range to a regime where the net charge of Lyz is opposite to that of the silica surface. β -Lg was chosen in order to extend this study to systems where the net charge of the protein is the same as that of the SiNP.

Qualitatively the two proteins show a similar adsorption behavior below their IEP (net charge of protein is opposite to that of the silica surface). The adsorbed amount increases with increasing pH and reaches a maximum close to the IEP. This is explained with the fact that close to the IEP the net charge of the proteins is neutral and thus the repulsive interactions between adsorbed protein molecules are small which allows a more dense packing on the silica surface. On the other hand, positively charged groups still exist by which the protein is anchored to the negatively charged surface. Because attractive electrostatic interactions are screened by electrolytes, it is expected that the adsorption of the protein is weakened by the addition of salt, which was confirmed by measurements. The observed salt effect gives strong evidence that the adsorption behavior is dominated by electrostatic forces while non-electrostatic and protein-specific interactions play a minor role in this regime.

In the case of β -Lg the regime of equal net charge of the protein and the silica particles was also accessible. Without added salt the adsorption capacity of β -Lg on the SiNPs drops sharply beyond the IEP, but in the presence of salt this drop becomes less pronounced and adsorption is still observed at a pH 9, i.e., well above the IEP. This salt-induced enhancement of adsorption may be partly due to the screening of the (negative) net charge on the adsorbed protein, but the origin of adsorption must be of a non-electrostatic nature. This was tentatively attributed to a different interplay of the single contributions to the overall adsorption energy.

Van-der-Waals forces and hydrophobic interactions may contribute more to the adsorption energy in this regime, and the addition of salt promotes the close approach of the equally charged proteins and particles.

Whereas in the literature, adsorption of proteins is commonly analyzed on the basis of the Langmuir or the Hill equation, in this work the liquid-phase variant of the Guggenheim – Anderson – de Boer (GAB) model¹⁰ was used for the quantitative analysis of the collected adsorption data. This isotherm model assumes two independent adsorption states: a more strongly bound state is attributed to adsorption in the first layer, and an additional weaker state to adsorption in any further layers. This model is similar to the well-known BET model for gas-phase adsorption. Like the BET model the GAB model reduces to the Langmuir isotherm in case the second (weaker) adsorption-constant reaches zero. For both proteins the Langmuir model underestimates the adsorbed amount of adsorbed protein at higher c_{eq} in large regions of bulk pH. The contribution of non-monolayer adsorption could be efficiently modeled by the use of the the GAB model. The total adsorbed amount Γ_{max} could be precisely predicted and the adsorption constants were estimated.

8.2 Hetero-Aggregation of Silica Nanoparticles with a Protein: Observing the Aggregate Structure with Fluorescence Methods

The hetero-aggregation of SiNPs with protein was previously investigated by small-angle scattering and analytical ultracentrifugation. In Chapter 4 of this thesis a study is presented in which fluorescence microscopy techniques are used to directly visualize the structures over a wide range of protein-to-particles number ratios (over 3 orders of magnitude). In order to achieve a high resolution and to enhance the contrast between aggregates and the surrounding medium a fluorescence confocal laser scanning microscope (CLSM) was used. Stacks of 2-dimensional micrographs were combined to achieve a 3-dimensional depiction of the aggregates. In order to compare the results of different protein-to-particle number ratios on a quantitative basis the surface-area-to-volume ratio (A/V) was calculated for every 3D stack. A low A/V is characteristic for a large compact aggregate while a high A/V is typical for a loose network structure and finely dispersed particles. It was found that A/V shows a minimum when the protein loading reaches a monolayer. For even higher protein loadings a gradual increase in A/V was detected. These results indicate that initially (at low protein-to-particle ratios, below a complete monolayer) a network-like structure is formed but only a limited number of adsorbed protein molecules is available as connecting nodes. Also, the high negative charge of the silica surface is not fully compensated by the adsorbed positively charged protein which leads to a strong repulsion between the single network components. With more adsorbed proteins more connecting points are generated and the complete network becomes electrostatically neutral.

Ultimately, the fine network collapses to a dense structure. This behavior is similar to findings of our earlier study³² where the limitation of connection points was achieved by limiting the protein adsorption by pH variation.

To extend this study to even lower protein-to-particle number ratios, this system was also studied by fluorescence correlation spectroscopy (FCS). This technique is superior to CLSM in detecting small aggregates and particles and therefore lower protein/particles ratios became measurable. The most remarkable result of the FCS experiment is the appearance of very small structures over the entire experimental protein-to-particle number ratio range. These small aggregates have a diameter of approximately one particle radius plus one protein radius. It stands to reason that single building blocks of aggregates are present, even when larger aggregates dominate the dispersion.

In future studies, the results of the CLSM experiments could be analyzed even further in order to calculate the fractal dimension of the aggregates. Fractal dimensions are frequently used to test structures for self-similarities and its structural complexity. In the context of this work this would allow us to compare the aggregate structure across the vastly different length scales probed in this CLSM experiment. The fractal dimension of the 3D CLSM data can be derived from the fractal dimension of the single 2D slices of each z-stack by $D_{\text{frac, 3D}} = D_{\text{frac, 2D}} + 1$.^{114–116} This method is valid until the size of the primary particle is smaller than the resolution of the microscope which is not the case for the studied system. More experiments are needed in order to verify whether fractal dimensions offer a way to compare the results extracted from the microscopy data with future light scattering studies and thus ensure its reliability.

Fractal dimensions derived from CLSM measurements can be compared with non-classical DLS methods which provide the opportunity to measure the opaque and non-transparent samples. In Chapter 4 (Fig. 4.7) the feasibility of modern DLS techniques was tested for aggregated Lyz/SiNP samples. This exemplary measurement yielded an intensity curve typical for mass fractal structures as was expected for this sample. It was concluded that non-classical DLS is a valuable technique for future studies and synergizes well with the 3D-analysis of CLSM micrographs.

Furthermore, it would be interesting to replace the labeled protein by intrinsically fluorescent proteins like GFP. This would avoid the problems of altering the native protein with an attached fluorescent dye. Unfortunately the fluorescent properties of those proteins are sensitive to its structure and therefore susceptible to deformations during the adsorption. Nevertheless, this is difficult to predict, and an experimental test is necessary to explore the feasibility of such studies.

A study on the kinetics of the protein mediated aggregation process was attempted in collaboration with H. Amenitsch at the Austrian SAXS beam line at the Elettra synchrotron in Trieste. In a first experiment standard stopped flow methods with SAXS detection showed that

the aggregation process is completed within the dead time of the system. In a second experiment, a free jet micromixer was used to access sub millisecond time scales.²¹⁴ It was found, that the process of particle aggregation is faster than a few milliseconds.²¹⁵ Although the data did not allow the determination of a precise rate constant for the flocculation process, it is clear that the aggregation is comparably fast. This is a hint that the kinetics of the system Lyz/SiNP obey the predictions of a diffusion limited aggregation process^{216,217} in which diffusion is the rate-limiting factor for the aggregate growth. This process typically generates mass fractal structures as they found them in the CLSM micrographs.

8.3 Orientation of Adsorbed Protein on bulk pH Conditions as a Consequence of the Dipole Orientation

In Chapter 5 an experimental method is presented which allows to test the predictions of protein binding sites to surfaces as obtained by simulations.⁴³ This method could help to find better surface supports for proteins planned for an industrial application.

The apparent diameter of cytochrome *c* adsorbed on the surface of differently sized silica particles has been followed over a wide pH range with small angle neutron scattering (SANS). Attempts to analyze the scattering intensity curves with a spherical shell model or individual non-interacting protein molecules and particles failed, as these simplistic models were unable to reproduce the individual high-*q* pattern caused by the shape of the scattering object. Ultimately, the scattering data was analyzed with an analytical form factor model accounting for the special shape of scatters in the sample. This model was originally developed for Pickering emulsions where smaller particles are situated at the surface of a bigger droplet resembling a ‘raspberry-like’ shape.⁴⁴ Most of the model parameter were known (e.g. concentrations) or determined independently (e.g. SiNP size) so that the complexity of the analysis was reduced to two free parameters.

A significant change in the apparent protein diameter was found between pH 4 and 5. This apparent reduction in diameter was observed for all studied particles sizes but shifted slightly towards higher pH for larger particles. This change in the apparent diameter was attributed to the change of the orientation of the ellipsoidal cytochrome *c* relative to the surface. Rationally, this means that cytochrome *c* is adsorbed in a ‘head-on’ configuration when exposed to low pH conditions and turns into a ‘side-on’ arrangement beyond pH 5. In order to rule out that the observed change is an intrinsic pH effect on the structure of the protein, a separate series of SANS measurements was performed in the absence of SiNPs. It was found that cytochrome *c* is pH-stable in the entire experimental range. This finding is in agreement with studies of the literature.³⁹

The experimentally found shift in the protein orientation was attributed tentatively to a major change in the dipole moment vector of cytochrome *c* happening in the same pH-region. To verify this conjecture, the distribution of charges in the structure of cytochrome *c* was modeled based on the PDB structure 2GIW. A combination of programs were used to assign the protonation state of each side chain and compute the dipole moment vector. It was shown that for the low pH-region the dipole moment vector is almost aligned parallel to the longer polar axis of the ellipsoidal structure of cytochrome *c*. When the pH is increased over pH 4 the dipole moment vector points perpendicular to the equatorial plane of the protein. This result supports our conclusion that the change in orientation of the adsorbed protein is closely linked with a change in the orientation of its dipole moment.

It is remarkable that even for the smallest tested particles (7 nm) whose size was comparable to the size of the protein (≈ 3 nm) the dipole moment seems to dictate the adsorption orientation. Smaller particles carry fewer charges and due to the curvature the neighboring charges would be further apart from the attached protein. Therefore it was not strictly expected to see such a clear behavior for the smallest particles.

Combining the experimental SANS data and the electrostatic modeling of the protein structure provides a strong tool to understand the adsorption on a microscopic scale. It might even be possible to predict the adsorption site of pH-stable proteins from its solution structure. Nevertheless, this method fails when adsorption is not electrostatically dominated or the net dipole moment is very small.

Although the results for the specific case of cytochrome *c* are convincing further testing is needed. One limitation is, that the protein solution structure was kept constant for all pH and only the protonation state was altered according to the pK_a of every side chain. Even when the overall shape of the protein remains the same it is still possible that the internal structure changes slightly. When ionic side chains are affected this would affect the dipole moment, too. Therefore a more sophisticated way of modeling the protein structure, its protonation state and even containing ions and cofactors is desirable.

8.4 Prediction of protein adsorption in native and chemically modified mesoporous silica materials

A model to estimate the protein loading capacity of a mesoporous solid with cylindrical pores of uniform size was published in literature (SVC model).¹⁴⁹ In Chapter 6 an extension of this model is presented which accounts for a distribution of pore sizes and which is also applicable to materials with chemically modified pore walls.

In order to test the validity of the new model a set of mesoporous materials (SBA-15) with chemically modified surfaces were synthesized. The materials were characterized with

nitrogen sorption, x-ray diffraction and thermogravimetric analysis. Based on this information, the pore size distribution and the degree of chemical modification of the pore walls were estimated. The materials differed significantly in the relative proportions of cylindrical pores, secondary pores and of the functional layer. It was possible to estimate the contributions of the cylindrical pores, secondary pores, silica matrix and functional layer to the total volume of the material. Protein adsorption experiments were carried out with lysozyme at two salinities and over a wide range of pH. Similar to the adsorption on spherical nanoparticles (cf. Chapter 3) the adsorbed amount increases towards the IEP of the protein independent from the chemical functionality presented on the surface of the solid material. Analogous to the situation for lysozyme adsorption at SiNPs, added salt was again found to cause a reduction of adsorption in the pores.

Comparing the proposed model with the existing model for protein adsorption showed an improvement especially for materials with a high content of secondary porosity. Often a significant fraction of such secondary porosity is not assessable to the protein as the pore size is smaller than the protein diameter. It was shown that it is important to account for such excluded pore space to correctly calculate the protein loading on porous solids. The formalism presented here can help to efficiently identify suitable support materials for industrially used proteins. It synergizes well with the results explained in Chapter 5 about protein orientation on particle surfaces. Considering the non-spherical shape of most proteins it is vital to know the apparent protein diameter. Combining the presented formalisms the protein loading capacity could be predicted on a micro- and mesoscopic scale, just by knowing the individual properties of each material.

One of the tested SBA-15 was modified with a zwitterionic surface. Generally such surfaces are considered as protein repellent. Remarkably, a significant adsorption of lysozyme was found for this material. It is not clear why the protein repelling effect is lacking in the confined space and further work is needed to understand this finding.

Another interesting future option is to expand the fluorescent experiments presented in Chapter 4 to porous materials. With the use of FCS it could be possible to quantify the kinetics of the protein diffusion inside the porous matrix. This is particularly interesting when the pore diameter becomes smaller than two times the protein diameter. Under these circumstances the diffusion processes should be described by single file diffusion (diffusion limited to one spatial dimension).^{218,219} In this case proteins in the pore matrix cannot pass each other making such systems interesting for controlled and sequential drug release.

8.5 Freezing/Melting of Aqueous Salt Systems in Silica Mesopores

In Chapter 7 the eutectic melting and freezing of aqueous salt solutions within the confinement of nanometer sized pores was studied. Differential scanning calorimetry (DSC) was used to determine the melting temperature for a number of aqueous salt solutions in three different pore sizes. Such results might have an impact in industrial applications to avoid weathering of buildings and monuments^{48–51} but also for the production of supported metal oxide catalysts.²²⁰

It was found that the confinement-induced shift of the eutectic temperature in the pores can be significantly greater than the shift of the melting temperature of pure water. This effect was explained by the additional confinement introduced by the precipitated salt crystals in the pores. More or less bulky salt crystals within the pore reduce the available pore volume for water and thus lead to an additional (secondary) confinement of ice/water in the pores. This effect is most dramatic for bulky oligohydrates which occupy a significant part of the pore volume, in some cases more than half of the available pore volume. The existence of such oligohydrate crystals in the external bulk solution could be proven with synchrotron SAXS/WAXS experiments performed at the Austrian SAXS beamline at the Elettra synchrotron in Trieste. From these assumptions a one-parameter model based on a modified version of the Kelvin equation was developed.¹⁸² This model is in good agreement with the general trend found in the experimental data for the depression of the eutectic temperature for all tested pore sizes and salt solutions. For a few samples more than one pore melting signal was detected. This was explained with a delayed transition of the one hydrate form to another one.

The water-rich region of the eutectic phase diagram for NaCl in the pores of SBA-15 and MCM-41 was measured in the presence of excess liquid phase. The fact that inside the pores only the eutectic phase transition could be observed was attributed to a diffusive exchange of salt from the excess liquid into the pore during cooling. Meanwhile we succeeded to prepare samples without excess phase by a two-solvent technique.²²¹ It was found that under these circumstances the complete phase diagram including the liquidus line in the pore could be detected by DSC.

It was also attempted to determine the size of salt crystals precipitated in the pore. Laboratory scale XRD experiments provided evidence that the crystals are much smaller than the pore diameter (4–7 nm) but the application of the Scherrer equation to such small crystals is problematic. Typically, the broadened Bragg peaks become indistinguishable from the background and a reliable analysis of the peak width fails. In this point more experiments including different techniques are needed to determine the size of precipitated salt in the pores.

During the synchrotron SAXS/WAXS measurements at Elettra it was also possible to collect precise data of the pore lattice deformation of SBA-15 during the freezing/melting temperature scans. Currently, the analysis is still ongoing and they might lead a way towards a

better understanding of the processes during the phase transition within the pores and the crystal size.

References

- 1 K. Bourzac, Quantum dots go on display, *Nature*, 2013, **493**, 283. DOI: 10.1038/493283a.
- 2 I. Sondi and B. Salopek-Sondi, Silver nanoparticles as antimicrobial agent, *Journal of Colloid and Interface Science*, 2004, **275**, 177–182. DOI: 10.1016/j.jcis.2004.02.012.
- 3 G. A. Martínez-Castañón, N. Niño-Martínez, F. Martínez-Gutierrez, J. R. Martínez-Mendoza and F. Ruiz, Synthesis and antibacterial activity of silver nanoparticles with different sizes, *J Nanopart Res*, 2008, **10**, 1343–1348. DOI: 10.1007/s11051-008-9428-6.
- 4 R. Singh and J. W. Lillard, Nanoparticle-based targeted drug delivery, *Experimental and molecular pathology*, 2009, **86**, 215–223. DOI: 10.1016/j.yexmp.2008.12.004.
- 5 T. C. Johnstone, K. Suntharalingam and S. J. Lippard, The Next Generation of Platinum Drugs, *Chemical reviews*, 2016, **116**, 3436–3486. DOI: 10.1021/acs.chemrev.5b00597.
- 6 W. Norde, in *Biopolymers at Interfaces, Second Edition*, ed. M. Malmsten, CRC Press, New York, 2003.
- 7 W. Norde, My voyage of discovery to proteins in flatland ...and beyond, *Colloids and surfaces. B, Biointerfaces*, 2008, **61**, 1–9. DOI: 10.1016/j.colsurfb.2007.09.029.
- 8 I. Langmuir, The Adsorption of Gases on Plane Surfaces of Glass, Mica and Platinum, *J. Am. Chem. Soc.*, 1918, **40**, 1361–1403. DOI: 10.1021/ja02242a004.
- 9 P. d. Pino, B. Pelaz, Q. Zhang, P. Maffre, G. U. Nienhaus and W. J. Parak, Protein corona formation around nanoparticles – from the past to the future, *Mater. Horiz.*, 2014, **1**, 301–313. DOI: 10.1039/C3MH00106G.
- 10 E. O. Timmermann, A B.E.T.-like three sorption stage isotherm, *J. Chem. Soc., Faraday Trans. 1*, 1989, **85**, 1631. DOI: 10.1039/f19898501631.
- 11 A. Ebadi, J. S. Soltan Mohammadzadeh and A. Khudiev, What is the correct form of BET isotherm for modeling liquid phase adsorption?, *Adsorption*, 2009, **15**, 65–73. DOI: 10.1007/s10450-009-9151-3.
- 12 Z. Zhou and M. Hartmann, Progress in enzyme immobilization in ordered mesoporous materials and related applications, *Chem. Soc. Rev.*, 2013, **42**, 3894. DOI: 10.1039/c3cs60059a.

- 13 D. I. Fried, F. J. Brieler and M. Fröba, Designing Inorganic Porous Materials for Enzyme Adsorption and Applications in Biocatalysis, *ChemCatChem*, 2013, **5**, 862–884. DOI: 10.1002/cctc.201200640.
- 14 A. Popat, S. B. Hartono, F. Stahr, J. Liu, S. Z. Qiao and G. Qing Lu, Mesoporous silica nanoparticles for bioadsorption, enzyme immobilisation, and delivery carriers, *Nanoscale*, 2011, **3**, 2801. DOI: 10.1039/c1nr10224a.
- 15 M. Malmsten, Inorganic nanomaterials as delivery systems for proteins, peptides, DNA, and siRNA, *Curr. Opin. Colloid Interface Sci.*, 2013, **18**, 468–480. DOI: 10.1016/j.cocis.2013.06.002.
- 16 C. Argyo, V. Weiss, C. Bräuchle and T. Bein, Multifunctional Mesoporous Silica Nanoparticles as a Universal Platform for Drug Delivery, *Chem. Mater.*, 2014, **26**, 435–451. DOI: 10.1021/cm402592t.
- 17 M. Xue and G. H. Findenegg, Lysozyme as a pH-Responsive Valve for the Controlled Release of Guest Molecules from Mesoporous Silica, *Langmuir*, 2012, **28**, 17578–17584. DOI: 10.1021/la304152j.
- 18 D. Zhao, Q. Huo, J. Feng, B. F. Chmelka and G. D. Stucky, Nonionic Triblock and Star Diblock Copolymer and Oligomeric Surfactant Syntheses of Highly Ordered, Hydrothermally Stable, Mesoporous Silica Structures, *J. Am. Chem. Soc.*, 1998, **120**, 6024–6036. DOI: 10.1021/ja974025i.
- 19 D. Margolese, J. A. Melero, S. C. Christiansen, B. F. Chmelka and G. D. Stucky, Direct Syntheses of Ordered SBA-15 Mesoporous Silica Containing Sulfonic Acid Groups, *Chem. Mater.*, 2000, **12**, 2448–2459. DOI: 10.1021/cm0010304.
- 20 K. Gawlitza, C. Wu, R. Georgieva, D. Wang, M. B. Ansorge-Schumacher and R. von Klitzing, Immobilization of lipase B within micron-sized poly-N-isopropylacrylamide hydrogel particles by solvent exchange, *Physical chemistry chemical physics : PCCP*, 2012, **14**, 9594–9600. DOI: 10.1039/c2cp40624a.
- 21 L.-C. Sang and M.-O. Coppens, Effects of surface curvature and surface chemistry on the structure and activity of proteins adsorbed in nanopores, *Phys. Chem. Chem. Phys.*, 2011, **13**, 6689. DOI: 10.1039/c0cp02273j.
- 22 J. Liu, S. Bai, Q. Jin, H. Zhong, C. Li and Q. Yang, Improved Catalytic Performance of Lipase Accommodated in the Mesoporous Silicas with Polymer-Modified Microenvironment, *Langmuir*, 2012, **28**, 9788–9796. DOI: 10.1021/la301330s.
- 23 K.-C. Kao, T.-S. Lin and C.-Y. Mou, Enhanced Activity and Stability of Lysozyme by Immobilization in the Matching Nanochannels of Mesoporous Silica Nanoparticles, *J. Phys. Chem. C*, 2014, **118**, 6734–6743. DOI: 10.1021/jp4112684.

- 24 M. Kahse, M. Werner, S. Zhao, M. Hartmann, G. Buntkowsky and R. Winter, Stability, Hydration, and Thermodynamic Properties of RNase A Confined in Surface-Functionalized SBA-15 Mesoporous Molecular Sieves, *J. Phys. Chem. C*, 2014, **118**, 21523–21531. DOI: 10.1021/jp506544n.
- 25 Z. G. Estephan, P. S. Schlenoff and J. B. Schlenoff, Zwitteration As an Alternative to PEGylation, *Langmuir*, 2011, **27**, 6794–6800. DOI: 10.1021/la200227b.
- 26 B. Derjaguin and L. Landau, Theory of the stability of strongly charged lyophobic sols and of the adhesion of strongly charged particles in solutions of electrolytes, *Progress in Surface Science*, 1993, **43**, 30–59. DOI: 10.1016/0079-6816(93)90013-L.
- 27 E. Verwey and T. Overbeek, *Theory of the stability of lyophobic colloids; the interaction of sol particles having an electric double layer*, Elsevier Publishing Company, New York, 1948.
- 28 D. Grasso, K. Subramaniam, M. Butkus, K. Strevett and J. Bergendahl, A review of non-DLVO interactions in environmental colloidal systems, *Rev Environ Sci Biotechnol*, 2002, **1**, 17–38. DOI: 10.1023/A:1015146710500.
- 29 I. Yadav, S. Kumar, V. K. Aswal and J. Kohlbrecher, Structure and Interaction in the pH-Dependent Phase Behavior of Nanoparticle-Protein Systems, *Langmuir : the ACS journal of surfaces and colloids*, 2017, **33**, 1227–1238. DOI: 10.1021/acs.langmuir.6b04127.
- 30 N. Mine Eren, G. Narsimhan and O. H. Campanella, Protein adsorption induced bridging flocculation: the dominant entropic pathway for nano-bio complexation, *Nanoscale*, 2016, **8**, 3326–3336. DOI: 10.1039/c5nr06179b.
- 31 B. Bharti, J. Meissner and G. H. Findenegg, Aggregation of Silica Nanoparticles Directed by Adsorption of Lysozyme, *Langmuir*, 2011, **27**, 9823–9833. DOI: 10.1021/la201898v.
- 32 B. Bharti, J. Meissner, S. H. L. Klapp and G. H. Findenegg, Bridging interactions of proteins with silica nanoparticles, *Soft Matter*, 2014, **10**, 718–728. DOI: 10.1039/C3SM52401A.
- 33 S. R. Saptarshi, A. Duschl and A. L. Lopata, Interaction of nanoparticles with proteins, *Journal of nanobiotechnology*, 2013, **11**, 26. DOI: 10.1186/1477-3155-11-26.
- 34 L. Shang, Y. Wang, J. Jiang and S. Dong, pH-dependent protein conformational changes in albumin, *Langmuir*, 2007, **23**, 2714–2721. DOI: 10.1021/la062064e.
- 35 N. Wangoo, C. R. Suri and G. Shekhawat, Interaction of gold nanoparticles with protein, *Appl. Phys. Lett.*, 2008, **92**, 133104. DOI: 10.1063/1.2902302.

- 36 T. Chatterjee, S. Chakraborti, P. Joshi, S. P. Singh, V. Gupta and P. Chakrabarti, The effect of zinc oxide nanoparticles on the structure of the periplasmic domain of the *Vibrio cholerae* ToxR protein, *The FEBS journal*, 2010, **277**, 4184–4194. DOI: 10.1111/j.1742-4658.2010.07807.x.
- 37 P. Asuri, S. S. Bale, R. C. Pangule, D. A. Shah, R. S. Kane and J. S. Dordick, Structure, function, and stability of enzymes covalently attached to single-walled carbon nanotubes, *Langmuir*, 2007, **23**, 12318–12321. DOI: 10.1021/la702091c.
- 38 S. Laera, G. Ceccone, F. Rossi, D. Gilliland, R. Hussain, G. Siligardi and L. Calzolari, Measuring protein structure and stability of protein-nanoparticle systems with synchrotron radiation circular dichroism, *Nano letters*, 2011, **11**, 4480–4484. DOI: 10.1021/nl202909s.
- 39 A. Kondo, S. Oku and K. Higashitani, Structural changes in protein molecules adsorbed on ultrafine silica particles, *Journal of Colloid and Interface Science*, 1991, **143**, 214–221. DOI: 10.1016/0021-9797(91)90454-G.
- 40 A. A. Vertegel, R. W. Siegel and J. S. Dordick, Silica Nanoparticle Size Influences the Structure and Enzymatic Activity of Adsorbed Lysozyme, *Langmuir*, 2004, **20**, 6800–6807. DOI: 10.1021/la0497200.
- 41 M. Lundqvist, I. Sethson and B.-H. Jonsson, Protein Adsorption onto Silica Nanoparticles, *Langmuir*, 2004, **20**, 10639–10647. DOI: 10.1021/la0484725.
- 42 M. Karlsson and U. Carlsson, Protein adsorption orientation in the light of fluorescent probes: mapping of the interaction between site-directly labeled human carbonic anhydrase II and silica nanoparticles, *Biophysical Journal*, 2005, **88**, 3536–3544. DOI: 10.1529/biophysj.104.054809.
- 43 N. Hildebrand, S. Köppen, L. Derr, K. Li, M. Koleini, K. Rezwani and L. Colombi Ciacchi, Adsorption Orientation and Binding Motifs of Lysozyme and Chymotrypsin on Amorphous Silica, *J. Phys. Chem. C*, 2015, **119**, 7295–7307. DOI: 10.1021/acs.jpcc.5b00560.
- 44 K. Larson-Smith, A. Jackson and D. C. Pozzo, Small angle scattering model for Pickering emulsions and raspberry particles, *Journal of Colloid and Interface Science*, 2010, **343**, 36–41. DOI: 10.1016/j.jcis.2009.11.033.
- 45 A. Salis, D. F. Parsons, M. Boström, L. Medda, B. Barse, B. W. Ninham and M. Monduzzi, Ion Specific Surface Charge Density of SBA-15 Mesoporous Silica, *Langmuir*, 2010, **26**, 2484–2490. DOI: 10.1021/la902721a.
- 46 N. Schwierz, D. Horinek and R. R. Netz, Reversed anionic Hofmeister series, *Langmuir : the ACS journal of surfaces and colloids*, 2010, **26**, 7370–7379. DOI: 10.1021/la904397v.

- 47 L. D. Gelb, K. E. Gubbins, R. Radhakrishnan and M. Śliwińska-Bartkowiak, Phase separation in confined systems, *Rep. Prog. Phys.*, 2000, **63**, 727. DOI: 10.1088/0034-4885/63/4/501.
- 48 D. Camuffo, Physical weathering of stones, *Science of The Total Environment*, 1995, **167**, 1–14. DOI: 10.1016/0048-9697(95)04565-I.
- 49 V. Cnudde and P. J. S. Jacobs, Monitoring of weathering and conservation of building materials through non-destructive X-ray computed microtomography, *Env Geol*, 2004, **46**. DOI: 10.1007/s00254-004-1049-5.
- 50 R. B. G. Williams and D. A. Robinson, Weathering of sandstone by the combined action of frost and salt, *Earth Surf. Process. Landforms*, 1981, **6**, 1–9. DOI: 10.1002/esp.3290060102.
- 51 E. Ruiz-Agudo, F. Mees, P. J. S. Jacobs and C. Rodriguez-Navarro, The role of saline solution properties on porous limestone salt weathering by magnesium and sodium sulfates, *Environ Geol*, 2007, **52**, 269–281. DOI: 10.1007/s00254-006-0476-x.
- 52 S. Papida, W. Murphy and E. May, Enhancement of physical weathering of building stones by microbial populations, *International Biodeterioration & Biodegradation*, 2000, **46**, 305–317. DOI: 10.1016/S0964-8305(00)00102-5.
- 53 M. Minsky, Microscopy Apparatus, US patent 3013467, 1957.
- 54 S. Inoué, in *Handbook Of Biological Confocal Microscopy*, ed. J. B. Pawley, Springer US, Boston, MA, 2006, pp. 1–19.
- 55 P. Davidovits and M. D. Egger, Scanning laser microscope for biological investigations, *Applied optics*, 1971, **10**, 1615–1619. DOI: 10.1364/AO.10.001615.
- 56 N. Åslund, A. Liljeborg, P.-O. Forsgren and S. Wahlsten, Three-dimensional digital microscopy using the PHOIBOSI Scanner, *Scanning*, 1987, **9**, 227–235. DOI: 10.1002/sca.4950090603.
- 57 S. W. Hell and J. Wichmann, Breaking the diffraction resolution limit by stimulated emission, *Opt. Lett.*, 1994, **19**, 780. DOI: 10.1364/OL.19.000780.
- 58 S. W. Hell, Far-field optical nanoscopy, *Science (New York, N.Y.)*, 2007, **316**, 1153–1158. DOI: 10.1126/science.1137395.
- 59 M. J. Rust, M. Bates and X. Zhuang, Sub-diffraction-limit imaging by stochastic optical reconstruction microscopy (STORM), *Nature methods*, 2006, **3**, 793–795. DOI: 10.1038/nmeth929.
- 60 Nathan S. Claxton, Thomas J. Fellers and Michael W. Davidson, Laser Scanning Confocal Microscopy.

- 61 D. Magde, E. L. Elson and W. W. Webb, Fluorescence correlation spectroscopy. II. An experimental realization, *Biopolymers*, 1974, **13**, 29–61. DOI: 10.1002/bip.1974.360130103.
- 62 J. Ries and P. Schwille, Fluorescence correlation spectroscopy, *BioEssays : news and reviews in molecular, cellular and developmental biology*, 2012, **34**, 361–368. DOI: 10.1002/bies.201100111.
- 63 O. Krichevsky and G. Bonnet, Fluorescence correlation spectroscopy, *Rep. Prog. Phys.*, 2002, **65**, 251–297. DOI: 10.1088/0034-4885/65/2/203.
- 64 B. Bharti and G. H. Findenegg, Protein-specific Effects of Binding to Silica Nanoparticles, *Chem. Lett.*, 2012, **41**, 1122–1124. DOI: 10.1246/cl.2012.1122.
- 65 J. S. Pedersen, Structure factors effects in small-angle scattering from block copolymer micelles and star polymers, *The Journal of Chemical Physics*, 2001, **114**, 2839–2846. DOI: 10.1063/1.1339221.
- 66 L. Banci, I. Bertini, J. G. Huber, G. A. Spyroulias and P. Turano, Solution structure of reduced horse heart cytochrome c, *Journal of Biological Inorganic Chemistry*, 1999, **4**, 21–31. DOI: 10.1007/s007750050285.
- 67 T. J. Dolinsky, J. E. Nielsen, J. A. McCammon and N. A. Baker, PDB2PQR: An automated pipeline for the setup of Poisson-Boltzmann electrostatics calculations, *Nucleic Acids Research*, 2004, **32**, W665–W667. DOI: 10.1093/nar/gkh381.
- 68 T. J. Dolinsky, P. Czodrowski, H. Li, J. E. Nielsen, J. H. Jensen, G. Klebe and N. A. Baker, PDB2PQR: Expanding and upgrading automated preparation of biomolecular structures for molecular simulations, *Nucleic Acids Research*, 2007, **35**, W522–W525. DOI: 10.1093/nar/gkm276.
- 69 M. H. M. Olsson, C. R. Søndergaard, M. Rostkowski and J. H. Jensen, PROPKA3, *Journal of chemical theory and computation*, 2011, **7**, 525–537. DOI: 10.1021/ct100578z.
- 70 C. R. Søndergaard, M. H. M. Olsson, M. Rostkowski and J. H. Jensen, Improved Treatment of Ligands and Coupling Effects in Empirical Calculation and Rationalization of pKa Values, *Journal of chemical theory and computation*, 2011, **7**, 2284–2295. DOI: 10.1021/ct200133y.
- 71 B. L. Mellor, S. Khadka, D. D. Busath and B. A. Mazzeo, Influence of pK a Shifts on the Calculated Dipole Moments of Proteins, *Protein J*, 2011, **30**, 490–498. DOI: 10.1007/s10930-011-9355-8.
- 72 J. E. Nielsen, T. J. Dolinsky, N. A. Baker and K. Monson, *PDB2PQR Server*, available at: http://nbc-222.ucsd.edu/pdb2pqr_2.0.0/, accessed 9 October 2017.

- 73 Miguel Ortiz-Lombardia, *calculating dipole moment*, available at: <https://sourceforge.net/p/apbs/mailman/attachment/d5dc3ecc0706020322r761ca22i55fb0b7724516e36@mail.gmail.com/2/>.
- 74 E. F. Pettersen, T. D. Goddard, C. C. Huang, G. S. Couch, D. M. Greenblatt, E. C. Meng and T. E. Ferrin, UCSF Chimera--a visualization system for exploratory research and analysis, *Journal of computational chemistry*, 2004, **25**, 1605–1612. DOI: 10.1002/jcc.20084.
- 75 N. A. Baker, D. Sept, S. Joseph, M. J. Holst and J. A. McCammon, Electrostatics of nanosystems: Application to microtubules and the ribosome, *Proceedings of the National Academy of Sciences*, 2001, **98**, 10037–10041. DOI: 10.1073/pnas.181342398.
- 76 N. A. Baker, *APBS-PDB2PQR*, available at: <http://apbs-pdb2pqr.readthedocs.io/en/latest/>, accessed 31 August 2017.
- 77 S. Tanaka, Theory of power-compensated DSC, *Thermochimica Acta*, 1992, **210**, 67–76. DOI: 10.1016/0040-6031(92)80277-4.
- 78 A. Schreiber, *Phasenverhalten reiner Stoffe in mesoporösen Silika-Materialien*, Technische Universität Berlin.
- 79 H. Hoffmann and M. Reger, Emulsions with unique properties from proteins as emulsifiers, *Adv. Colloid Interface Sci.*, 2014, **205**, 94–104. DOI: 10.1016/j.cis.2013.08.007.
- 80 S. T. Moerz, A. Kraegeloh, M. Chanana and T. Kraus, Formation Mechanism for Stable Hybrid Clusters of Proteins and Nanoparticles, *ACS Nano*, 2015, **9**, 6696–6705. DOI: 10.1021/acsnano.5b01043.
- 81 A. E. Nel, L. Mädler, D. Velegol, T. Xia, E. M. V. Hoek, P. Somasundaran, F. Klaessig, V. Castranova and M. Thompson, Understanding biophysicochemical interactions at the nano–bio interface, *Nat. Mater.*, 2009, **8**, 543–557. DOI: 10.1038/nmat2442.
- 82 A. A. Shemetov, I. Nabiev and A. Sukhanova, Molecular Interaction of Proteins and Peptides with Nanoparticles, *ACS Nano*, 2012, **6**, 4585–4602. DOI: 10.1021/nn300415x.
- 83 M. Kurylowicz, M. Giuliani and J. R. Dutcher, Using Nanoscale Substrate Curvature to Control the Dimerization of a Surface-Bound Protein, *ACS Nano*, 2012, 10571–10580. DOI: 10.1021/nn302948d.
- 84 W. Shang, J. H. Nuffer, V. A. Muñoz-Papandrea, W. Colón, R. W. Siegel and J. S. Dordick, Cytochrome c on Silica Nanoparticles, *Small*, 2009, **5**, 470–476. DOI: 10.1002/smll.200800995.

- 85 X. Wu and G. Narsimhan, Effect of surface concentration on secondary and tertiary conformational changes of lysozyme adsorbed on silica nanoparticles, *Biochim. Biophys. Acta*, 2008, **1784**, 1694–1701. DOI: 10.1016/j.bbapap.2008.06.008.
- 86 X. Wu and G. Narsimhan, Characterization of Secondary and Tertiary Conformational Changes of β -Lactoglobulin Adsorbed on Silica Nanoparticle Surfaces, *Langmuir*, 2008, **24**, 4989–4998. DOI: 10.1021/la703349c.
- 87 G. Anand, S. Sharma, A. K. Dutta, S. K. Kumar and G. Belfort, Conformational Transitions of Adsorbed Proteins on Surfaces of Varying Polarity, *Langmuir*, 2010, **26**, 10803–10811. DOI: 10.1021/la1006132.
- 88 A. Wittemann and M. Ballauff, Interaction of proteins with linear polyelectrolytes and spherical polyelectrolyte brushes in aqueous solution.
- 89 O. Hollmann, R. Steitz and C. Czeslik, Structure and dynamics of α -lactalbumin adsorbed at a charged brush interface, *Phys. Chem. Chem. Phys.*, 2008, **10**, 1448. DOI: 10.1039/b716264b.
- 90 W. M. de Vos, P. M. Biesheuvel, A. de Keizer, J. M. Kleijn and M. A. Cohen Stuart, Adsorption of the Protein Bovine Serum Albumin in a Planar Poly(acrylic acid) Brush Layer As Measured by Optical Reflectometry, *Langmuir*, 2008, **24**, 6575–6584. DOI: 10.1021/la8006469.
- 91 K. Henzler, B. Haupt, K. Lauterbach, A. Wittemann, O. Borisov and M. Ballauff, Adsorption of β -Lactoglobulin on Spherical Polyelectrolyte Brushes, *J. Am. Chem. Soc.*, 2010, **132**, 3159–3163. DOI: 10.1021/ja909938c.
- 92 F. E. Regnier, The role of protein structure in chromatographic behavior, *Science*, 1987, **238**, 319–323. DOI: 10.1126/science.3310233.
- 93 R. A. Hartvig, M. van de Weert, J. Østergaard, L. Jorgensen and H. Jensen, Protein Adsorption at Charged Surfaces, *Langmuir*, 2011, **27**, 2634–2643. DOI: 10.1021/la104720n.
- 94 P. M. Biesheuvel, M. van der Veen and W. Norde, A Modified Poisson–Boltzmann Model Including Charge Regulation for the Adsorption of Ionizable Polyelectrolytes to Charged Interfaces, Applied to Lysozyme Adsorption on Silica, *J. Phys. Chem. B*, 2005, **109**, 4172–4180. DOI: 10.1021/jp0463823.
- 95 C. A. Haynes and W. Norde, Globular proteins at solid/liquid interfaces, *Colloids Surf., B*, 1994, **2**, 517–566. DOI: 10.1016/0927-7765(94)80066-9.
- 96 H. Larsericsdotter, S. Oscarsson and J. Buijs, Thermodynamic Analysis of Proteins Adsorbed on Silica Particles, *J. Colloid Interface Sci.*, 2001, **237**, 98–103. DOI: 10.1006/jcis.2001.7485.

- 97 M. van der Veen, W. Norde and M. C. Stuart, Electrostatic interactions in protein adsorption probed by comparing lysozyme and succinylated lysozyme, *Colloids Surf., B*, 2004, **35**, 33–40. DOI: 10.1016/j.colsurfb.2004.02.005.
- 98 T. Nezu, T. Masuyama, K. Saskai, S. Saitoh, M. Taira and Y. ARAKI, Effect of pH and Addition of Salt on the Adsorption Behavior of Lysozyme on Gold, Silica, and Titania Surfaces Observed by Quartz Crystal Microbalance with Dissipation Monitoring, *Dent. Mater. J.*, 2008, **27**, 573–580. DOI: 10.4012/dmj.27.573.
- 99 A. V. Hill, The possible effects of the aggregation of the molecules of haemoglobin on its dissociation curves, *J. Physiology*, 1910, **40**, iv–vii.
- 100 C. Röcker, M. Pötzl, F. Zhang, W. J. Parak and G. U. Nienhaus, A quantitative fluorescence study of protein monolayer formation on colloidal nanoparticles, *Nat. Nanotech.*, 2009, **4**, 577–580. DOI: 10.1038/nnano.2009.195.
- 101 A. P. Minton, Effects of excluded surface area and adsorbate clustering on surface adsorption of proteins, *Biophys. Chem.*, 2000, **86**, 239–247. DOI: 10.1016/S0301-4622(00)00151-4.
- 102 U. M. Elofsson, M. A. Paulsson and T. Arnebrant, Adsorption of β -Lactoglobulin A and B in Relation to Self-Association, *Langmuir*, 1997, **13**, 1695–1700. DOI: 10.1021/la9601061.
- 103 M. Verheul, J. S. Pedersen, Roefs, Sebastianus P. F. M. and K. G. de Kruif, Association behavior of native beta-lactoglobulin, *Biopolymers*, 1999, **49**, 11–20. DOI: 10.1002/(SICI)1097-0282(199901)49:1<11::AID-BIP2>3.0.CO;2-1.
- 104 D. M. Lugo, J. Oberdisse, A. Lapp and G. H. Findenegg, Effect of Nanoparticle Size on the Morphology of Adsorbed Surfactant Layers, *J. Phys. Chem. B*, 2010, **114**, 4183–4191. DOI: 10.1021/jp911400j.
- 105 J. Meissner, A. Prause, C. Di Tommaso, B. Bharti and G. H. Findenegg, Protein Immobilization in Surface-Functionalized SBA-15, *J. Phys. Chem. C*, 2015, **119**, 2438–2446. DOI: 10.1021/jp5096745.
- 106 P. Żeliszewska, A. Bratek-Skicki, Z. Adamczyk and M. Cieřła, Human Fibrinogen Adsorption on Positively Charged Latex Particles, *Langmuir*, 2014, **30**, 11165–11174. DOI: 10.1021/la5025668.
- 107 R. Anandakrishnan, B. Aguilar and A. V. Onufriev, H⁺⁺ 3.0, *Nucleic Acids Res.*, 2012, **40**, W537–W541. DOI: 10.1093/nar/gks375.
- 108 K. Kubiak-Ossowska and P. A. Mulheran, Mechanism of Hen Egg White Lysozyme Adsorption on a Charged Solid Surface, *Langmuir*, 2010, **26**, 15954–15965. DOI: 10.1021/la102960m.
- 109 N. Welsch, J. Dzubiella, A. Graebert and M. Ballauff, Protein binding to soft polymeric layers, *Soft matter*, 2012, **8**, 12043. DOI: 10.1039/c2sm26798e.

- 110 M. Hiramatsu, N. Okabe and K. Tomita, Preparation and properties of lysozyme modified by fluorescein-isothiocyanate, *Journal of biochemistry*, 1973, **73**, 971–978.
- 111 J. Schindelin, I. Arganda-Carreras, E. Frise, V. Kaynig, M. Longair, T. Pietzsch, S. Preibisch, C. Rueden, S. Saalfeld, B. Schmid, J.-Y. Tinevez, D. J. White, V. Hartenstein, K. Eliceiri, P. Tomancak and A. Cardona, Fiji, *Nature methods*, 2012, **9**, 676–682. DOI: 10.1038/nmeth.2019.
- 112 S. Bolte and F. P. Cordelières, A guided tour into subcellular colocalization analysis in light microscopy, *Journal of microscopy*, 2006, **224**, 213–232. DOI: 10.1111/j.1365-2818.2006.01706.x.
- 113 D. W. Schaefer, Polymers, fractals, and ceramic materials, *Science*, 1989, **243**, 1023–1027. DOI: 10.1126/science.243.4894.1023.
- 114 B. B. Mandelbrot, *The fractal geometry of nature*, Freeman, New York, NY, 1983.
- 115 Thill, Veerapaneni, Simon, Wiesner, Bottero and Snidaro, Determination of Structure of Aggregates by Confocal Scanning Laser Microscopy, *Journal of Colloid and Interface Science*, 1998, **204**, 357–362. DOI: 10.1006/jcis.1998.5570.
- 116 Thill, Wagner and Bottero, Confocal Scanning Laser Microscopy as a Tool for the Determination of 3D Floc Structure, *Journal of Colloid and Interface Science*, 1999, **220**, 465–467. DOI: 10.1006/jcis.1999.6478.
- 117 H.-S. Han, E. Niemeyer, Y. Huang, W. S. Kamoun, J. D. Martin, J. Bhaumik, Y. Chen, S. Roberge, J. Cui, M. R. Martin, D. Fukumura, R. K. Jain, M. G. Bawendi and D. G. Duda, Quantum dot/antibody conjugates for in vivo cytometric imaging in mice, *Proceedings of the National Academy of Sciences of the United States of America*, 2015, **112**, 1350–1355. DOI: 10.1073/pnas.1421632111.
- 118 A. Tan, J. Rajadas and A. M. Seifalian, Exosomes as nano-theranostic delivery platforms for gene therapy, *Advanced drug delivery reviews*, 2013, **65**, 357–367. DOI: 10.1016/j.addr.2012.06.014.
- 119 J. N. Anker, W. P. Hall, O. Lyandres, N. C. Shah, J. Zhao and R. P. van Duyne, Biosensing with plasmonic nanosensors, *Nature materials*, 2008, **7**, 442–453. DOI: 10.1038/nmat2162.
- 120 C. D. Walkey and W. C. W. Chan, Understanding and controlling the interaction of nanomaterials with proteins in a physiological environment, *Chemical Society reviews*, 2012, **41**, 2780–2799. DOI: 10.1039/c1cs15233e.
- 121 S. A. Bhakta, E. Evans, T. E. Benavidez and C. D. Garcia, Protein adsorption onto nanomaterials for the development of biosensors and analytical devices: a review, *Analytica chimica acta*, 2015, **872**, 7–25. DOI: 10.1016/j.aca.2014.10.031.

- 122 S. T. Moerz and P. Huber, Protein adsorption into mesopores: a combination of electrostatic interaction, counterion release, and van der Waals forces, *Langmuir*, 2014, **30**, 2729–2737. DOI: 10.1021/la404947j.
- 123 S. Gon and M. M. Santore, Single component and selective competitive protein adsorption in a patchy polymer brush: opposition between steric repulsions and electrostatic attractions, *Langmuir*, 2011, **27**, 1487–1493. DOI: 10.1021/la104592f.
- 124 A. Hung, S. Mwenifumbo, M. Mager, J. J. Kuna, F. Stellacci, I. Yarovsky and M. M. Stevens, Ordering surfaces on the nanoscale: implications for protein adsorption, *Journal of the American Chemical Society*, 2011, **133**, 1438–1450. DOI: 10.1021/ja108285u.
- 125 F. Secundo, Conformational changes of enzymes upon immobilisation, *Chemical Society reviews*, 2013, **42**, 6250–6261. DOI: 10.1039/c3cs35495d.
- 126 M. Wang, C. Fu, X. Liu, Z. Lin, N. Yang and S. Yu, Probing the mechanism of plasma protein adsorption on Au and Ag nanoparticles with FT-IR spectroscopy, *Nanoscale*, 2015, **7**, 15191–15196. DOI: 10.1039/c5nr04498g.
- 127 P. L. Edmiston, J. E. Lee, S.-S. Cheng and S. S. Saavedra, Molecular Orientation Distributions in Protein Films. 1. Cytochrome c Adsorbed to Substrates of Variable Surface Chemistry, *J. Am. Chem. Soc.*, 1997, **119**, 560–570. DOI: 10.1021/ja962366a.
- 128 T. Cha, A. Guo and X.-Y. Zhu, Enzymatic activity on a chip: the critical role of protein orientation, *Proteomics*, 2005, **5**, 416–419. DOI: 10.1002/pmhc.200400948.
- 129 N. S. Wigginton, A. de Titta, F. Piccapietra, J. Dobias, V. J. Nesatyy, M. J. F. Suter and R. Bernier-Latmani, Binding of silver nanoparticles to bacterial proteins depends on surface modifications and inhibits enzymatic activity, *Environmental science & technology*, 2010, **44**, 2163–2168. DOI: 10.1021/es903187s.
- 130 J. Romanowska, D. B. Kokh and R. C. Wade, When the Label Matters: Adsorption of Labeled and Unlabeled Proteins on Charged Surfaces, *Nano letters*, 2015, **15**, 7508–7513. DOI: 10.1021/acs.nanolett.5b03168.
- 131 W. Shang, J. H. Nuffer, V. A. Muniz-Papandrea, W. Colon, R. W. Siegel and J. S. Dordick, Cytochrome C on silica nanoparticles: influence of nanoparticle size on protein structure, stability, and activity, *Small*, 2009, **5**, 470–476. DOI: 10.1002/smll.200800995.
- 132 L. C. J. Thomassen, A. Aerts, V. Rabolli, D. Lison, L. Gonzalez, M. Kirsch-Volders, D. Napierska, P. H. Hoet, C. E. A. Kirschhock and J. A. Martens, Synthesis and Characterization of Stable Monodisperse Silica Nanoparticle Sols for in Vitro Cytotoxicity Testing, *Langmuir*, 2010, **26**, 328–335. DOI: 10.1021/la902050k.

- 133 T. M. Davis, M. A. Snyder, J. E. Krohn and M. Tsapatsis, Nanoparticles in Lysine–Silica Sols, *Chem. Mater.*, 2006, **18**, 5814–5816. DOI: 10.1021/cm061982v.
- 134 L. A. Feigin and D. I. Svergun, eds., *Structure analysis by small-angle X-ray and neutron scattering*, Plenum Press, New York, 1987.
- 135 G. R. Moore and G. W. Pettigrew, eds., *Cytochromes c. Evolutionary, structural and physicochemical aspects*, Springer, Berlin, 1990.
- 136 R. E. Dickerson, T. Takano, D. Eisenberg, O. B. Kallai, L. Samson, A. Cooper and E. Margoliash, Ferricytochrome c. I. General features of the horse and bonito proteins at 2.8 Å resolution, *The Journal of biological chemistry*, 1971, **246**, 1511–1535.
- 137 T. Takano and R. E. Dickerson, Conformation Change of Cytochrome c, *Journal of Molecular Biology*, 1981, **153**, 95–115. DOI: 10.1016/0022-2836(81)90529-5.
- 138 *SasView*, available at: <http://www.sasview.org/>, accessed 28 April 2016.
- 139 O. Glatter and Kratky Otto, eds., *Small angle X-ray scattering*, Acad. Pr, London, 2nd edn., 1983.
- 140 I. Yadav, V. K. Aswal and J. Kohlbrecher, Size-dependent interaction of silica nanoparticles with lysozyme and bovine serum albumin proteins, *Phys. Rev. E*, 2016, **93**. DOI: 10.1103/PhysRevE.93.052601.
- 141 A. Guinier and G. Fournet, eds., *Small-Angle Scattering of X-Rays*, John Wiley & Sons, Inc, New York, 1955.
- 142 D. Lugo, J. Oberdisse, M. Karg, R. Schweins and G. H. Findenegg, Surface aggregate structure of nonionic surfactants on silica nanoparticles, *Soft matter*, 2009, **5**, 2928. DOI: 10.1039/b903024g.
- 143 B. Bharti, J. Meissner, U. Gasser and G. H. Findenegg, Surfactant adsorption and aggregate structure at silica nanoparticles, *Soft matter*, 2012, **8**, 6573. DOI: 10.1039/c2sm25648g.
- 144 P. Debye, Zerstreung von Röntgenstrahlen, *Ann. Phys.*, 1915, **351**, 809–823. DOI: 10.1002/andp.19153510606.
- 145 W. H. Koppenol, J. D. Rush, J. D. Mills and E. Margoliash, The dipole moment of cytochrome c, *Molecular biology and evolution*, 1991, **8**, 545–558.
- 146 J. G. Fraaije, J. M. Kleijn, M. van der Graaf and J. C. Dijt, Orientation of adsorbed cytochrome c as a function of the electrical potential of the interface studied by total internal reflection fluorescence, *Biophysical Journal*, 1990, **57**, 965–975. DOI: 10.1016/S0006-3495(90)82616-3.
- 147 J. Prass, D. Mütter, P. Fratzl and O. Paris, Capillarity-driven deformation of ordered nanoporous silica, *Appl. Phys. Lett.*, 2009, **95**, 83121. DOI: 10.1063/1.3213564.

- 148 H. H. P. Yiu and P. A. Wright, Enzymes supported on ordered mesoporous solids, *J. Mater. Chem.*, 2005, **15**, 3690. DOI: 10.1039/b506090g.
- 149 L.-C. Sang, A. Vinu and M.-O. Coppens, General Description of the Adsorption of Proteins at Their Iso-electric Point in Nanoporous Materials, *Langmuir*, 2011, **27**, 13828–13837. DOI: 10.1021/la202907f.
- 150 P. I. Ravikovitch and A. V. Neimark, Characterization of Micro- and Mesoporosity in SBA-15 Materials from Adsorption Data by the NLDTFT Method, *J. Phys. Chem. B*, 2001, **105**, 6817–6823. DOI: 10.1021/jp010621u.
- 151 J. Landers, G. Y. Gor and A. V. Neimark, Density functional theory methods for characterization of porous materials, *Colloids Surf., A*, 2013, **437**, 3–32. DOI: 10.1016/j.colsurfa.2013.01.007.
- 152 M. Imperor-Clerc, P. Davidson and A. Davidson, Existence of a Microporous Corona around the Mesopores of Silica-Based SBA-15 Materials Templated by Triblock Copolymers, *J. Am. Chem. Soc.*, 2000, **122**, 11925–11933. DOI: 10.1021/ja002245h.
- 153 G. A. Zickler, S. Jähnert, W. Wagermaier, S. S. Funari, G. H. Findenegg and O. Paris, Physisorbed films in periodic mesoporous silica studied by in situ synchrotron small-angle diffraction, *Phys. Rev. B*, 2006, **73**. DOI: 10.1103/PhysRevB.73.184109.
- 154 G. H. Findenegg, S. Jähnert, D. Mütter, J. Prass and O. Paris, Fluid adsorption in ordered mesoporous solids determined by in situ small-angle X-ray scattering, *Phys. Chem. Chem. Phys.*, 2010, **12**, 7211. DOI: 10.1039/c001541p.
- 155 R. A. Pollock, B. R. Walsh, J. Fry, I. T. Ghampson, Y. B. Melnichenko, H. Kaiser, R. Pynn, W. J. DeSisto, M. C. Wheeler and B. G. Frederick, Size and Spatial Distribution of Micropores in SBA-15 using CM-SANS, *Chem. Mater.*, 2011, **23**, 3828–3840. DOI: 10.1021/cm200707y.
- 156 C. J. Gommers, H. Friedrich, M. Wolters, P. E. d. Jongh and K. P. d. Jong, Quantitative Characterization of Pore Corrugation in Ordered Mesoporous Materials Using Image Analysis of Electron Tomograms, *Chem. Mater.*, 2009, **21**, 1311–1317. DOI: 10.1021/cm803092c.
- 157 M. van der Veen, W. Norde and M. C. Stuart, Electrostatic interactions in protein adsorption probed by comparing lysozyme and succinylated lysozyme, *Colloids Surf., B*, 2004, **35**, 33–40. DOI: 10.1016/j.colsurfb.2004.02.005.
- 158 J. Deere, E. Magner, J. G. Wall and B. K. Hodnett, Mechanistic and Structural Features of Protein Adsorption onto Mesoporous Silicates, *J. Phys. Chem. B*, 2002, **106**, 7340–7347. DOI: 10.1021/jp0139484.

- 159 M. S. Bhattacharyya, P. Hiwale, M. Piras, L. Medda, D. Steri, M. Piludu, A. Salis and M. Monduzzi, Lysozyme Adsorption and Release from Ordered Mesoporous Materials, *J. Phys. Chem. C*, 2010, **114**, 19928–19934. DOI: 10.1021/jp1078218.
- 160 D. Steri, M. Monduzzi and A. Salis, Ionic strength affects lysozyme adsorption and release from SBA-15 mesoporous silica, *Microporous Mesoporous Mater.*, 2013, **170**, 164–172. DOI: 10.1016/j.micromeso.2012.12.002.
- 161 A. Vinu, V. Murugesan and M. Hartmann, Adsorption of Lysozyme over Mesoporous Molecular Sieves MCM-41 and SBA-15, *J. Phys. Chem. B*, 2004, **108**, 7323–7330. DOI: 10.1021/jp037303a.
- 162 C. Lei, Y. Shin, J. K. Magnuson, G. Fryxell, L. L. Lasure, D. C. Elliott, J. Liu and E. J. Ackerman, Characterization of functionalized nanoporous supports for protein confinement, *Nanotechnology*, 2006, **17**, 5531–5538. DOI: 10.1088/0957-4484/17/22/001.
- 163 T. P. B. Nguyen, J.-W. Lee, W. G. Shim and H. Moon, Synthesis of functionalized SBA-15 with ordered large pore size and its adsorption properties of BSA, *Microporous Mesoporous Mater.*, 2008, **110**, 560–569. DOI: 10.1016/j.micromeso.2007.06.054.
- 164 F. Hoffmann, M. Cornelius, J. Morell and M. Fröba, Silica-Based Mesoporous Organic–Inorganic Hybrid Materials, *Angew. Chem. Int. Ed.*, 2006, **45**, 3216–3251. DOI: 10.1002/anie.200503075.
- 165 D. Mauder, D. Akcakayiran, S. B. Lesnichin, G. H. Findenegg and I. G. Shenderovich, Acidity of Sulfonic and Phosphonic Acid-Functionalized SBA-15 under Almost Water-Free Conditions, *J. Phys. Chem. C*, 2009, **113**, 19185–19192. DOI: 10.1021/jp907058y.
- 166 J. B. Schlenoff, Zwitteration, *Langmuir*, 2014, **30**, 9625–9636. DOI: 10.1021/la500057j.
- 167 B.-H. Min, E.-Y. Jeong, M. Thommes and S.-E. Park, Direct synthesis of plugged SBA-15 type mesoporous silica using alcoholamines, *Chem. Commun.*, 2011, **47**, 4673. DOI: 10.1039/c1cc10420a.
- 168 D. Akcakayiran, *Pure and acid-functionalized ordered mesoporous silicas: Hosts for metallo-supramolecular coordination polymers*, Berlin, 2008.
- 169 A. Galarneau, H. Cambon, F. Di Renzo, R. Ryoo, M. Choi and F. Fajula, Microporosity and connections between pores in SBA-15 mesostructured silicas as a function of the temperature of synthesis, *New J. Chem.*, 2003, **27**, 73–79. DOI: 10.1039/b207378c.
- 170 Z. G. Estephan, J. A. Jaber and J. B. Schlenoff, Zwitterion-Stabilized Silica Nanoparticles, *Langmuir*, 2010, **26**, 16884–16889. DOI: 10.1021/la103095d.

- 171 M. Litt and T. Matsuda, Siloxane zwitterions, *J. Appl. Polym. Sci.*, 1975, **19**, 1221–1225. DOI: 10.1002/app.1975.070190502.
- 172 C. A. Schneider, W. S. Rasband and K. W. Eliceiri, NIH Image to ImageJ, *Nat Meth*, 2012, **9**, 671–675. DOI: 10.1038/nmeth.2089.
- 173 M. Jaroniec and L. A. Solovyov, Improvement of the Kruk–Jaroniec–Sayari Method for Pore Size Analysis of Ordered Silicas with Cylindrical Mesopores, *Langmuir*, 2006, **22**, 6757–6760. DOI: 10.1021/la0609571.
- 174 H. K. Christenson, Confinement effects on freezing and melting, *J. Phys.: Condens. Matter*, 2001, **13**, R95–R133. DOI: 10.1088/0953-8984/13/11/201.
- 175 C. Alba-Simionesco, B. Coasne, G. Dosseh, G. Dudziak, K. E. Gubbins, R. Radhakrishnan and M. Śliwińska-Bartkowiak, Effects of confinement on freezing and melting, *J. Phys.: Condens. Matter*, 2006, **18**, R15–R68. DOI: 10.1088/0953-8984/18/6/R01.
- 176 P. Huber, Soft matter in hard confinement, *J. Phys.: Condens. Matter*, 2015, **27**, 103102. DOI: 10.1088/0953-8984/27/10/103102.
- 177 G. Algara-Siller, O. Lehtinen, F.-C. Wang, R. R. Nair, U. Kaiser, H. Wu, A. K. Geim and I. V. Grigorieva, Square ice in graphene nanocapillaries, *Nature*, 2015, **519**, 443–445. DOI: 10.1038/nature14295.
- 178 K. Watanabe, M. Tadokoto and M. Oguni, Thermal Characteristics of Channel Water Confined in Nanopores with Crystalline Pore-Wall Structure in [M(H₂bim)₃](TMA)⁺nH₂O, *J. Phys. Chem. C*, 2012, **116**, 11768–11775. DOI: 10.1021/jp302222r.
- 179 C. U. Kim, B. Barstow, M. W. Tate and S. M. Gruner, Evidence for liquid water during the high-density to low-density amorphous ice transition, *Proc. Natl. Acad. Sci. USA*, 2009, **106**, 4596–4600. DOI: 10.1073/pnas.0812481106.
- 180 F. G. Alabarse, J. Haines, O. Cambon, C. Levelut, D. Bourgogne, A. Haidoux, D. Granier and B. Coasne, Freezing of Water Confined at the Nanoscale, *Phys. Rev. Lett.*, 2012, **109**. DOI: 10.1103/PhysRevLett.109.035701.
- 181 K. Morishige and K. Kawano, Freezing and melting of water in a single cylindrical pore, *J. Chem. Phys.*, 1999, **110**, 4867. DOI: 10.1063/1.478372.
- 182 G. H. Findenegg, S. Jähnert, D. Akcakayiran and A. Schreiber, Freezing and Melting of Water Confined in Silica Nanopores, *ChemPhysChem*, 2008, **9**, 2651–2659. DOI: 10.1002/cphc.200800616.
- 183 M. Erko, G. H. Findenegg, N. Cade, A. G. Michette and O. Paris, Confinement-induced structural changes of water studied by Raman scattering, *Phys. Rev. B*, 2011, **84**. DOI: 10.1103/PhysRevB.84.104205.

- 184 M. Erko, D. Wallacher, A. Hoell, T. Hauß, I. Zizak and O. Paris, Density minimum of confined water at low temperatures, *Phys. Chem. Chem. Phys.*, 2012, **14**, 3852. DOI: 10.1039/c2cp24075k.
- 185 D. Liu, Y. Zhang, C.-C. Chen, C.-Y. Mou, P. H. Poole and S.-H. Chen, Observation of the density minimum in deeply supercooled confined water, *Proc. Natl. Acad. Sci. USA*, 2007, **104**, 9570–9574. DOI: 10.1073/pnas.0701352104.
- 186 S. Jähnert, F. Vaca Chávez, G. E. Schaumann, A. Schreiber, M. Schönhoff and G. H. Findenegg, Melting and freezing of water in cylindrical silica nanopores, *Phys. Chem. Chem. Phys.*, 2008, **10**, 6039. DOI: 10.1039/b809438c.
- 187 A. A. Zavitsas, Properties of Water Solutions of Electrolytes and Nonelectrolytes, *J. Phys. Chem. B*, 2001, **105**, 7805–7817. DOI: 10.1021/jp011053l.
- 188 M. Dubois, T. Zemb, L. Belloni, A. Delville, P. Levitz and R. Setton, Osmotic pressure and salt exclusion in electrostatically swollen lamellar phases, *J. Chem. Phys.*, 1992, **96**, 2278. DOI: 10.1063/1.462078.
- 189 M. Steiger, Crystal growth in porous materials—II, *J. Crys. Growth*, 2005, **282**, 470–481. DOI: 10.1016/j.jcrysgr.2005.05.008.
- 190 R. Cohen-Adad and J. W. Lorimer, *Alkali metal and ammonium chlorides in water and heavy water (binary systems)*, Pergamon Press, Oxford, New York, 1st edn., 1991.
- 191 R. Farasat, B. Yancey and S. Vyazovkin, Loading salts from solutions into nanopores, *Chem. Phys. Lett.*, 2013, **558**, 72–76. DOI: 10.1016/j.cplett.2013.01.009.
- 192 M. Dishon, O. Zohar and U. Sivan, From Repulsion to Attraction and Back to Repulsion, *Langmuir*, 2009, **25**, 2831–2836. DOI: 10.1021/la803022b.
- 193 K. Collins, Ions from the Hofmeister series and osmolytes, *Methods*, 2004, **34**, 300–311. DOI: 10.1016/j.ymeth.2004.03.021.
- 194 C. Weidenthaler, Pitfalls in the characterization of nanoporous and nanosized materials, *Nanoscale*, 2011, **3**, 792. DOI: 10.1039/c0nr00561d.
- 195 M. Imperor-Clerc, D. Bazin, M.-D. Appay, P. Beaunier and A. Davidson, Crystallization of β -MnO₂ Nanowires in the Pores of SBA-15 Silicas, *Chem. Mater.*, 2004, **16**, 1813–1821. DOI: 10.1021/cm035353m.
- 196 G. Satishkumar, L. Titelman and M. V. Landau, Mechanism for the formation of tin oxide nanoparticles and nanowires inside the mesopores of SBA-15, *Journal of Solid State Chemistry*, 2009, **182**, 2822–2828. DOI: 10.1016/j.jssc.2009.07.039.
- 197 J. van der Meer, I. Bardez-Giboire, C. Mercier, B. Revel, A. Davidson and R. Denoyel, Mechanism of Metal Oxide Nanoparticle Loading in SBA-15 by the

- Double Solvent Technique, *J. Phys. Chem. C*, 2010, **114**, 3507–3515. DOI: 10.1021/jp907002y.
- 198 C. Petit, C. Karwacki, G. Peterson and T. J. Bandosz, Interactions of Ammonia with the Surface of Microporous Carbon Impregnated with Transition Metal Chlorides, *J. Phys. Chem. C*, 2007, **111**, 12705–12714. DOI: 10.1021/jp072066n.
- 199 Y. I. Aristov, Challenging offers of material science for adsorption heat transformation, *Applied Thermal Engineering*, 2013, **50**, 1610–1618. DOI: 10.1016/j.applthermaleng.2011.09.003.
- 200 R. M. Espinosa Marzal and G. W. Scherer, Crystallization of sodium sulfate salts in limestone, *Environ Geol*, 2008, **56**, 605–621. DOI: 10.1007/s00254-008-1441-7.
- 201 N. Shahidzadeh-Bonn, J. Desarnaud, F. Bertrand, X. Chateau and D. Bonn, Damage in porous media due to salt crystallization, *Phys. Rev. E*, 2010, **81**. DOI: 10.1103/PhysRevE.81.066110.
- 202 A. Schreiber, I. Ketelsen and G. H. Findenegg, Melting and freezing of water in ordered mesoporous silica materials, *Phys. Chem. Chem. Phys.*, 2001, **3**, 1185–1195. DOI: 10.1039/b010086m.
- 203 J. W. Lorimer and R. Cohen-Adad, eds., *Solubility Data Serie Vol. 47. Alkali Metal and Ammonium Chlorides in Water and Heavy Water (Binary Systems)*, Pergamon Press, Oxford, New York, Beijing, Frankfurt, Seoul, Sydney, Tokio, 47th edn., 1991.
- 204 E. W. Washburn, ed., *International critical tables of numerical data, physics, chemistry and technology*, Published for the National Research Council by McGraw-Hill, New York, 4th edn., 1928.
- 205 T. R. Briggs and W. F. Geigle, Note on the System Sodium Iodide–Water, *J. Phys. Chem.*, 1940, **44**, 373–377. DOI: 10.1021/j150399a009.
- 206 K. Thomsen, *Modeling systems containing fluoride in addition to H₂O. (K⁺, Na⁺, H⁺, Ca²⁺) - (Cl⁻, HSO₄⁻, SO₄²⁻, OH⁻, CO₂, HCO₃⁻, CO₃²⁻, H₃PO₄, H₂PO₄⁻, HPO₄²⁻, PO₄³⁻)*.
- 207 D. S. Eisenberg and W. Kauzmann, *The structure and properties of water [by] D. Eisenberg and W. Kauzmann*, Oxford University Press, Oxford, 1969.
- 208 R. C. Weast, ed., *CRC Handbook of chemistry and physics*, CRC Press, Cleveland, Ohio, 52nd edn., 1971.
- 209 B. Klewe and B. Pedersen, The crystal structure of sodium chloride dihydrate, *Acta Crystallogr B Struct Crystallogr Cryst Chem*, 1974, **30**, 2363–2371. DOI: 10.1107/S0567740874007138.
- 210 T. H. Anderson and E. C. Lingafelter, The structure of potassium fluoride dihydrate, *Acta Cryst*, 1951, **4**, 181–182. DOI: 10.1107/S0365110X51000520.

- 211 G. Beurskens and G. A. Jeffrey, Crystal Structure of Potassium Fluoride Tetrahydrate, *The Journal of Chemical Physics*, 1964, **41**, 917–923. DOI: 10.1063/1.1726033.
- 212 J. Tegenfeldt, R. Tellgren, B. Pedersen and I. Olovsson, Neutron diffraction study of sodium bromide dihydrate, *Acta Crystallogr B Struct Sci*, 1979, **35**, 1679–1682. DOI: 10.1107/S0567740879007391.
- 213 J. Nývlt, The Ostwald Rule of Stages, *Cryst. Res. Technol.*, 1995, **30**, 443–449. DOI: 10.1002/crat.2170300402.
- 214 B. Marmiroli, G. Greci, F. Cacho-Nerin, B. Sartori, E. Ferrari, P. Laggner, L. Businaro and H. Amenitsch, Free jet micromixer to study fast chemical reactions by small angle X-ray scattering, *Lab on a chip*, 2009, **9**, 2063–2069. DOI: 10.1039/b904296b.
- 215 B. Marmiroli, B. Sartori, J. Meissner, G. Greci, M. Girod, G. H. Findenegg and H. Amenitsch, SAXS and free jet micromixer to study the sub-millisecond/millisecond interaction of silica nanoparticles with proteins, 16th Conference on Small Angle Scattering, Berlin, 2015.
- 216 T. A. Witten and L. M. Sander, Diffusion-Limited Aggregation, a Kinetic Critical Phenomenon, *Phys. Rev. Lett.*, 1981, **47**, 1400–1403. DOI: 10.1103/PhysRevLett.47.1400.
- 217 P. Meakin, S. Tolman and A. Blumen, Diffusion-Limited Aggregation, *Proceedings of the Royal Society A: Mathematical, Physical and Engineering Sciences*, 1989, **423**, 133–148. DOI: 10.1098/rspa.1989.0046.
- 218 S. Y. Yang, J.-A. Yang, E.-S. Kim, G. Jeon, E. J. Oh, K. Y. Choi, S. K. Hahn and J. K. Kim, Single-file diffusion of protein drugs through cylindrical nanochannels, *ACS nano*, 2010, **4**, 3817–3822. DOI: 10.1021/nn100464u.
- 219 Q. Wei, C. Bechinger and P. Leiderer, Single-File Diffusion of Colloids in One-Dimensional Channels, *Science*, 2000, **287**, 625–627. DOI: 10.1126/science.287.5453.625.
- 220 E. Baktash, P. Littlewood, J. Pfrommer, R. Schomäcker, M. Driess and A. Thomas, Controlled Formation of Nickel Oxide Nanoparticles on Mesoporous Silica using Molecular Ni₄O₄ Clusters as Precursors, *ChemCatChem*, 2015, **7**, 1280–1284. DOI: 10.1002/cctc.201402983.
- 221 A. Prause, J. Meissner, C. Koczwar, H. Amenitsch, O. Paris and G. H. Findenegg, Freezing and Melting of Aqueous Salt Systems in Nanopores, 9th International Conference on Porous Media, Rotterdam, 2017.

Abbreviations and Symbols

2D	: Two-dimensional
3D	: Three-dimensional
A/V	: Surface-area-to-volume ratio
A_0	: Footprint area of Lyz in side-on orientation
a_0	: Lattice parameter
AcOH	: Acetic acid
a_{geom}	: Geometric surface area
APBS	: Adaptive Poisson Boltzmann solver
a_s	: Specific surface area
BET	: Brunauer – Emmett – Teller
b_i	: Scattering length of the nucleus i
BICINE	: 2-(bis(2-hydroxyethyl)-amino)-acetic acid
C	: K_S/K_L
c^*	: Reference concentration of lysozyme (2 mg/mL)
CAPS	: 3-(cyclohexyl-amino)-1-propane sulfonic acid
CD	: Circular dichroism
c_{eq}	: Equilibrium concentration
C_{GT}	: Gibbs-Thomson constant
CLSM	: Confocal laser scanning microscopy
D	: pore diameter
D_{SiNP}	: Diameter of silica nanoparticle
D/σ	: Reduced pore diameter
D_f	: Diffusion coefficient
DLVO	: Derjaguin, Landau, Verwey and Overbeek
D_p^{ax}	: Axial diameter of an ellipsoid
D_p^{eq}	: Equatorial diameter of an ellipsoid
D_{part}	: Diameter of an OMS particle
DSC	: Differential scanning calorimetry
E	: Peak from eutectic melting
E_f	: Peak from eutectic freezing
$f(D)$: Normalized pore size distribution
FCS	: Fluorescence correlation spectroscopy
FITC	: Fluorescein-5-isothiocyanat
FTC	: Fluorescein dye
$G(\tau)$: Autocorrelation function
GAB	: Guggenheim - Anderson - de Boer
h_E	: Hydration number
$I(q)$: Scattered intensity as a function of q
IEP	: Isoelectric point
IS	: Ionic strength
K	: Langmuir adsorption constant
k	: Scherrer constant

k_B	: Boltzmann constant
K_H	: Henry's law adsorption constant
KJS	: Kruk – Jaroniec – Sayari
K_L	: Adsorption constant for weakly bound protein
K_S	: Adsorption constant for strongly bound protein
L	: Melting along the liquidus line (bulk)
L_f	: Freezing along the liquidus line (bulk)
L_{pore}	: Freezing/melting along the liquidus line in pores
Lyz	: Lysozyme
Lyz_{FTC}	: FTC labeled lysozyme
$\text{Lyz}_{\text{native}}$: Native lysozyme
M	: Prefactor accounting for total SLD of 'raspberry-like' particles
m_E	: Molality at eutectic point
m_F/m_S	: Mass ratio of functional organic group to silica
m_{max}	: Limiting adsorbed amount of Lyz in pores
m_S	: Mass of silica
m_{total}	: Maximum uptake of Lyz as expected from porefilling model
MW	: Molecular weight
N	: Number of proteins per SiNP
n	: Refractive index
NA	: Numerical aperture
N_A	: Avogadro constant
N_{ext}	: Number of protein molecules adsorbed at the external surface of OMS
nfl	: Non-freezing layer
NLDFT	: Nonlocal density functional theory
N_m	: number of adsorption sites per unit area
N_p	: Average number of small particles
NP	: Nanoparticle
n_S	: Amount of salt
n_W	: Amount of water
OMS	: Ordered mesoporous silica
P	: Peak from eutectic melting in pores
$P(q)$: Form factor
PDB	: Protein data base
P_f	: peak from eutectic freezing in pores
pK_a	: Logarithmic acid dissociation constant
PSD	: Pore size distribution function
\vec{q}	: Scattering vector
Q_i	: Quantum yield
RB	: Raspberry-like
R_C	: Effective core radius of a pore for freezing
R_h	: Hydrodynamic radius
R_{SC}	: Effective core radius considering secondary confinement
s	: Polydispersity
$S(q)$: Structure factor

SANS	: Small-angle neutron scattering
SAXS	: Small-angle x-ray scattering
SC	: Secondary confinement
SiNP	: Silica nanoparticle
SLD	: Scattering length density
SLS	: Static light scattering
STED	: Stimulated emission depletion
SVC	: Sang, Vinu, Coppens
T_0	: Melting temperature of bulk water
T_E	: Eutectic temperature
TEM	: Transmission electron microscopy
TEOS	: Tetraethoxysilane
$T_{E,p}$: Eutectic temperature in pores
TGA	: Thermogravimetry
T_{max}	: Temperature at DSC peak maximum
T_{ons}	: Temperature at DSC peak onset
T_p^0	: Melting temperature of confined water
V_G	: Volume of Gaussian profile
w_E	: Eutectic composition as weight fraction of salt
x_E	: Mole fraction of salt at eutectic point
XRD	: X-ray diffraction
β -Lg	: β -lactoglobulin
Γ	: Surface concentration of adsorbed protein
δ	: Penetration factor for the 'raspberry-like' model
ΔT_{nfl}	: Increment from ion specific influences on the non-freezing layer
ΔT_p	: Increment between TE and TE _p
ΔT_0	: Increment between T ₀ and T _{p0}
ε	: Secondary porosity
$\Delta\rho$: Scattering length density difference
ζ	: Zeta potential
η	: Viscosity
θ	: Scattering angle
λ	: Wavelength
λ_D	: Debye length
$\vec{\mu}$: Dipole moment vector
μ_e	: Electrophoretic mobility
ξ	: Aspect ratio of the Gaussian profile
ρ_F	: Density of organic functionalization
ρ_i	: Weighing parameter
ρ_S	: Density of silica
σ	: Protein diameter
σ_0	: Electrokinetic surface charge density
$\tau_{D,i}$: Characteristic lag time of the component i
ϕ_E	: Volume fraction of salt in the solid eutectic mixture
$\phi_m(D)$: Protein packing fraction as function of pore diameter

